Nondestructive Relative Permittivity and Loss Tangent Measurements Using a Split-Cylinder Resonator

by

Michael Daniel Janezic

B.S., University of Colorado, 1990

M.S., University of Colorado, 1996

A thesis submitted to the

Faculty of the Graduate School of the

University of Colorado in partial fulfillment

of the requirements for the degree of

Doctor of Philosophy

Department of Electrical and Computer Engineering

2003

This thesis entitled:
Nondestructive Relative Permittivity and Loss Tangent Measurements Using a Split-Cylinder Resonator
written by Michael Daniel Janezic
has been approved for the Department of Electrical and Computer Engineering

Edward F. Kuester

James Baker-Jarvis

Date _____

The final copy of this thesis has been examined by the signatories, and we find that both the content and the form meet acceptable presentation standards of scholarly work in the above mentioned discipline.

Janezic, Michael Daniel (Ph.D., Electrical Engineering)

Nondestructive Relative Permittivity and Loss Tangent Measurements Using a Split-Cylinder Resonator

Thesis directed by Professor. Edward F. Kuester

To keep pace with the expanding wireless and electronics industries, manufacturers are developing innovative materials for improving system performance, and there is a critical need to accurately characterize the electrical properties of these new materials at microwave frequencies. To address this need, this thesis develops a nondestructive method for measuring the relative permittivity and loss tangent of dielectric substrates using a split-cylinder resonator.

Three theoretical models for the split-cylinder resonator are derived using mode-matching, least-squares boundary residual, and Hankel-transform methods, from which one can calculate the relative permittivity and loss tangent of a dielectric substrate from measurements of the split-cylinder resonator's TE_{0np} resonant frequency and quality factor.

Each of these models has several advantages over previously published models. First, the accuracy of the relative permittivity measurement is increased because each model accurately models the fringing fields that extend beyond the cylindrical-cavity sections. Second, to increase the accuracy of the loss tangent measurement, each model accurately separates the conductive metal losses of the split-cylinder resonator from the dielectric losses of the substrate. Finally, in contrast to previous models for the split-cylinder resonator that use only the TE_{011} resonant mode, each of the new models include the higher-order TE_{0np} resonant modes, thereby broadening the frequency range over which one can make relative permittivity and loss tangent measurements. In a comparison of the three models, the mode-matching method was found to be superior on the basis of measurement accuracy and computational speed.

Relative permittivity and loss tangent measurements for several dielectric materials are performed using a split-cylinder resonator and are in good agreement with measurements made using a circular-cylindrical cavity, split-post resonator, and dielectric post resonator. This thesis also identifies sources of uncertainty and presents a comprehensive uncertainty budget for both the relative permittivity and loss tangent.

Dedication

This work is dedicated to my wife Jennifer whose constant love, encouragement and patience made everything possible.

Acknowledgements

I wish to express my deep gratitude to Professor Edward Kuester, my thesis advisor, for his insight, guidance, and patience throughout my education.

I am also indebted to Dr. James Baker-Jarvis, my project leader, who has been a wonderful mentor since my first days at NIST.

With his continued friendship and sense of humor, Jeffrey Jargon kept me sane by adding many moments of levity to the daily chaos.

The staff of the Radio-Frequency Technology Division at NIST has been a great source of encouragement since I was a sophomore at the University of Colorado. In particular, Robert Judish, William Kissick, and Dennis Friday always made my education a priority and provided the necessary funding.

I owe a great deal to the many wonderful teachers I've had a privilege know. In particular, Helen Wilson, Peg Smith, Steve Iona, and Marilyn Johnstone taught me lessons not found in any textbook.

Special thanks to Micheal and JoAnne Osborn for their interest in my education and the many memorable vacations over the years.

I am grateful to Dr. Donald DeGroot, Dr. K.C. Gupta, and Dr. Allen Herman for taking the time out of their busy schedules to be on my thesis committee. Their feedback and suggestions were appreciated.

For his continual instruction on matters of true import, I am indebted to Father Joseph Meznar.

I owe a great deal to my friend Eleanor Livingston for her willingness to be an editor. Her suggestions and comments were invaluable in improving this thesis.

Most importantly, I am continually grateful for my family who, from the beginning, demonstrated the importance of perseverance and hard work. Those early lessons and their continued love and support have helped me weather many storms.

Contents

Chapter

Tables

Table

Figures

Figure

Chapter 1

Introduction

The most precise methods for determining the relative permittivity $\epsilon_r^{'}$ and loss tangent $\tan\delta$ of low-loss dielectrics are resonator methods. Commonly-used resonator techniques include the dielectric-post resonator, circular-cylindrical cavity, and the whispering-gallery mode method [1]. Although usually limited to a single frequency, these resonant methods provide the needed accuracy that broadband methods lack. A disadvantage of these techniques is that samples must be accurately machined into a symmetrical geometry such as a cylinder. Since sample machining is destructive and sometimes expensive, conventional resonator methods are rarely used for large-scale quality-control purposes.

Kent developed a resonator technique for performing nondestructive measurements of the relative permittivity and loss tangent [2, 3]. This method, the *split-cylinder resonator* technique, uses a cylindrical cavity which is separated into two halves as shown in Figure 1.1. A sample is placed in the gap between the two shorted cylindrical waveguide sections. A TE_{0np} resonance is excited, and from measurements of the resonant frequency and the quality factor, one determines the relative permittivity and loss tangent of the sample. In terms of sample geometry, the only requirements are that the sample must extend beyond the diameter of the two cavity sections and the sample must be flat. This arrangement provides the accuracy of a resonator technique without having to machine the sample.

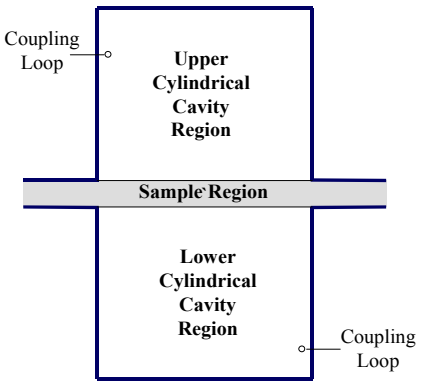

Figure 1.1: Split-cylinder resonator.

Unfortunately, having little or no sample preparation comes at the cost of needing a more comprehensive model for the split-cylinder resonator. In conventional resonator methods, the boundary-value problem is relatively straightforward since the electric and magnetic fields are confined to the sample or within a metallic cavity. However, for the split-cylinder resonator, a gap exists between the two cylindrical waveguide sections, and the electric and magnetic fields extend into the sample outside of the cylindrical waveguide regions.

Kent, in his original model [2], correctly recognized that neglecting the fields in the region of the sample outside of the waveguide sections would lead to a systematic error in the measured permittivity. He initially proposed a correction to the measured permittivity based on a perturbation calculation. Later, Kent and Bell developed an improved approximation to correct the initial model [4].

In contrast, this thesis develops three new theoretical models for the split-cylinder resonator. In each of the three models, we derive expressions for the electric and magnetic fields in each of the split-cylinder resonator regions, making

sure that we accurately represent the fringing fields in the sample region. By enforcing the appropriate boundary conditions on these fields we derive a resonance condition for the split-cylinder resonator that one can use to accurately calculate the relative permittivity of the dielectric substrate. Once expressions for the fields and the relative permittivity are determined, we develop for each model an explicit expression for the loss tangent. By properly separating the conductive losses in the split-cylinder resonator from the dielectric losses of the substrate, high-accuracy loss tangent measurements are possible. Chapter 2 presents the mode-matching model, while Chapter 3 and Chapter 4 outline the models derived with the least-squares boundary residual and Hankel-transform methods.

In Chapter 5 we compare the three models, derived in the previous three chapters, using a variety of criteria, including the satisfaction of the boundary conditions, agreement in computed relative permittivity and loss tangent, and computational speed. Based on this comparison, we conclude that the mode-matching model is superior and implement this model into our measurement software.

Finally, in Chapter 6, we develop the metrology required for accurate relative permittivity and loss tangent measurement made with the split-cylinder resonator. Beginning with the mechanical specifications of the split-cylinder resonator, we then discuss the characterization of the intermediate variables necessary to calculate the relative permittivity and loss tangent. Next, we provide a detailed step-by-step procedure for making measurements using a split-cylinder resonator and develop an uncertainty budget for both the relative permittivity and loss tangent. Then we present relative permittivity and loss tangent measurements of several dielectric substrates and show good agreement with measurements made using other techniques. Although we do present some single-frequency results using only the TE_{011} resonant mode, we also demonstrate how one can extend the measurement frequency range of the split-cylinder resonator by making use

of the higher-order TE_{0np} resonant modes. Finally, we summarize the results of a repeatability study that confirms the measurement stability of the split-cylinder resonator.

Chapter 2

Mode Matching Model

2.1 Introduction

The first method we selected to model the split-cylinder resonator was the mode-matching method. Developed in the 1940's [5, 6] and later generalized in the 1960's [7, 8], the mode-matching method remains a popular technique for solving electromagnetic boundary problems, especially those involving discontinuities in waveguides and transmission lines where explicit solutions are often not possible. Before using the mode-matching method to develop a theoretical model for the split-cylinder resonator, we describe the implementation of the mode-matching method for a simple discontinuity problem.

The mode-matching method is most often applied to problems where the geometry is composed of distinct regions that can be represented by a separable coordinate system. One such geometry is the discontinuity problem shown in Figure 2.1. In this example, the two regions, with different cross-sections, share a common z-axis and intersect at $z = 0$. The two regions could represent either an intersection of two waveguides or the two sections of a cavity resonator. In the former, one calculates the amplitudes of the reflected and transmitted waves at the discontinuity, while in the latter, one calculates the resonant frequencies of the resonator.

We represent the transverse electric and magnetic fields in each region by

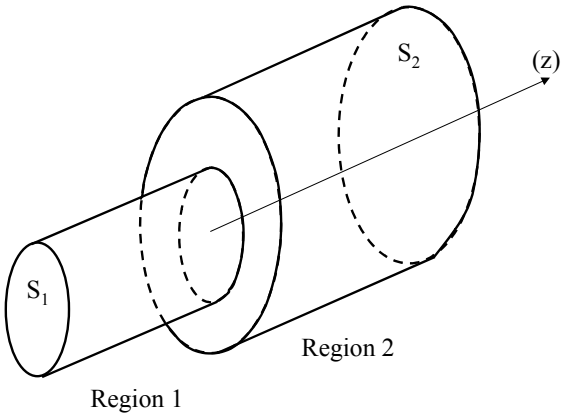

Figure 2.1: Example of a waveguide discontinuity.

an infinite series of normal modes. In region one,

$$\vec{E}_{T_1} = \sum_{n=1}^{\infty} A_n \vec{e}_{n_1}, \tag{2.1}$$

$$\vec{H}_{T_1} = \sum_{n=1}^{\infty} A_n \vec{h}_{n_1}, \tag{2.2}$$

while in region two,

$$\vec{E}_{T_2} = \sum_{n=1}^{\infty} B_n \vec{e}_{n_2}, \tag{2.3}$$

$$\vec{H}_{T_2} = \sum_{n=1}^{\infty} B_n \vec{h}_{n_2}. \tag{2.4}$$

where $\vec{e}_{n_i}$ and $\vec{h}_{n_i}$ are the transverse components of the nth mode in region i, and the constants A_n and B_n are unknown mode coefficients to be determined. If the cross-sections of regions one and two can be represented by a separable coordinate system, then $\vec{e}_{n_i}$ and $\vec{h}_{n_i}$ are merely the normal modes in each region. Each of these normal modes satisfies Maxwell's equations and the boundary conditions everywhere except the discontinuity at $z = 0$.

To satisfy the boundary conditions at the discontinuity, we find the solutions for the mode coefficients A_n and B_n. In our example, the transverse electric

and magnetic fields are continuous across the aperture denoted by S_1 and the transverse electric field is zero on the perfectly conducting surface not containing the aperture $(S_2 - S_1)$. Therefore, the resulting boundary conditions for the electric and magnetic field are

$$\vec{E}_{T_1} = \begin{cases} \vec{E}_{T_2} \text{ on } S_1 \\ 0 \text{ on } (S_2 - S_1) \end{cases} \tag{2.5}$$

and

$$\vec{H}_{T_1} = \vec{H}_{T_2} \text{ on } S_1. \tag{2.6}$$

Substituting equations (2.1-2.4) into (2.5) and (2.6), we obtain

$$\sum_{n=1}^{\infty} A_n \vec{e}_{n_1} = \begin{cases} \sum_{n=1}^{\infty} B_n \vec{e}_{n_2} \text{ on } S_1 \\ 0 \text{ on } (S_2 - S_1) \end{cases} \tag{2.7}$$

and

$$\sum_{n=1}^{\infty} A_n \vec{h}_{n_1} = \sum_{n=1}^{\infty} B_n \vec{h}_{n_2}. \tag{2.8}$$

To reduce the number of infinite series in both equation (2.7) and (2.8), we make use of the orthogonality of the modes in each region. In region 1, the orthogonality relation is

$$\int_{S_1} \vec{e}_{m_1} \times \vec{h}_{n_1} \cdot \vec{a}_z ds = V_{mn} \delta_{mn} \tag{2.9}$$

while the relation in region 2 is

$$\int_{S_2} \vec{e}_{m_2} \times \vec{h}_{n_2} \cdot \vec{a}_z ds = W_{mn} \delta_{mn} \tag{2.10}$$

where V_{mn} and W_{mn} are normalization constants and δ_{mn} is the Kronecker delta function. For these orthogonality relations to be valid, the modes in each waveguide must be nondegenerate, the waveguide boundaries must be perfect conductors, and the material contained within each of the waveguides must be lossless [9].

To simplify the boundary conditions on the electric field, we take the vector product of (2.7) with $\vec{h}_{m_2}$ and integrate over the cross-section S_2. Employing the

orthogonality relation found in (2.10), we eliminate one infinite series in equation (2.7)

$$\sum_{n=1}^{\infty} A_n C_{mn} = B_m W_{mm} \tag{2.11}$$

where

$$C_{mn} = \int_{S_2} (\vec{e}_{n_1} \times \vec{h}_{m_2}) \cdot \vec{a}_z \, ds. \tag{2.12}$$

We use the orthogonality relation for the waveguide modes in the larger waveguide to ensure that the boundary condition is enforced at $z = 0$ in both the aperture region S_1 and the conductive region $(S_2 - S_1)$ [10].

To simplify the boundary condition on the magnetic field, we take the vector product of (2.8) with $\vec{e}_{m_1}$ and integrate over the waveguide cross-section S_1. Using the orthogonality relation found in (2.9), equation (2.8) reduces to

$$A_m V_{mm} = \sum_{n=1}^{\infty} B_n D_{mn} \tag{2.13}$$

where

$$D_{mn} = \int_{S_1} (\vec{e}_{m_1} \times \vec{h}_{n_2}) \cdot \vec{a}_z \, ds. \tag{2.14}$$

We could have employed either of the orthogonality relations in equations (2.9) and (2.10) to simplify the magnetic field boundary condition in (2.8), since both relations enforce the boundary condition for the magnetic field on the aperture region S_1. However, by choosing the orthogonality relation for the waveguide modes in the smaller waveguide, we have employed the orthogonality relations from both regions, and this helps to reduce the errors due to relative convergence [11].

Equations (2.11) and (2.13) represent an infinite system of equations with unknown mode coefficients A_n and B_n. Although the boundary conditions are satisfied when we include an infinite number of modes in each region, we must truncate the number of modes in order to reduce the problem to a finite system

of equations. Assuming N_1 modes in region 1 and N_2 modes in region 2, we have a system of equations

$$\sum_{n=1}^{N_1} A_n C_{mn} = B_m W_{mm} \tag{2.15}$$

and

$$A_m V_{mm} = \sum_{n=1}^{N_2} B_n D_{mn}. \tag{2.16}$$

In matrix form, we can rewrite equations (2.15-2.16) as

$$\begin{bmatrix} \mathbf{C} & -\mathbf{W} \\ \mathbf{V} & -\mathbf{D} \end{bmatrix} \begin{bmatrix} \mathbf{A} \\ \mathbf{B} \end{bmatrix} = [\mathbf{Z}] \begin{bmatrix} \mathbf{A} \\ \mathbf{B} \end{bmatrix} = 0 \tag{2.17}$$

where

$$[\mathbf{Z}] = \begin{bmatrix} \mathbf{C} & -\mathbf{W} \\ \mathbf{V} & -\mathbf{D} \end{bmatrix}. \tag{2.18}$$

If, in our example of Figure 2.1, the problem is the intersection of waveguides, one can calculate the constants A_n and B_n from the system of equations in (2.17) and determine the electric and magnetic fields from equations (2.1-2.4). If, however, the problem is a cavity resonator, one would like to calculate the resonant frequencies of the cavity in addition to the constants A_n and B_n. The linear system of equations in (2.18) has a nontrivial solution only if

$$\det[\mathbf{Z}] = 0. \tag{2.19}$$

Equation (2.19) is the resonance condition for the cavity resonator, and one can calculate the resonant frequencies from this equation.

To implement the mode-matching method, it is always necessary to truncate the number of modes in each region. Unfortunately, this leads to a numerical error known as relative convergence. Wexler [7], in particular, first noted that numerical convergence was dependent on the ratio of the number of modes in each region and suggested that there might be a criterion for the ratio of modes that would minimize the relative convergence error. Further insight into relative convergence was

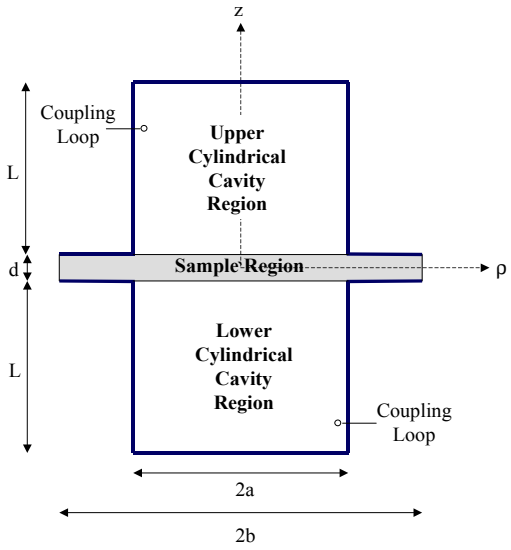

Figure 2.2: Cross-section of split-cylinder resonator with sample.

made by Masterman and Clarricoats [12]. In their paper, they observed that relative convergence was minimized when the spatial frequency of the highest mode in each region was the same. Later, Ilinski [13] found that the relative convergence is minimized when the wavelength of the highest-order mode in each region is the same, thus taking into account the differences in material properties between the regions. Besides specifying a particular ratio of modes in each region, Vassallo [11] found that the relative convergence could also be reduced by employing all available orthogonality relations. We will address relative convergence and other issues related to the mode-matching method in the next section where we use the method to derive a theoretical model for the split-cylinder resonator.

2.2 Split-Cylinder Theoretical Model

In this section, we apply the mode-matching method to the specific case of the split-cylinder resonator, shown in Figure 2.2. The split-cylinder resonator is a circular-cylindrical cavity of radius a and length $2L$, separated into two halves

by a variable-length gap containing a dielectric substrate. At $z = \pm d/2$, both cylindrical-cavity sections are terminated by a conductive flange that extends in the radial direction. A TE_{0np} resonant mode is excited with two coupling loops, one in each cylindrical-cavity section. Each of the loops is connected to a coaxial transmission line and each of the transmission lines is connected to a port of an automatic network analyzer.

A flat dielectric substrate, with a thickness d, is placed in the gap between the two cylindrical-cavity sections, and the gap between the two sections is decreased until the dielectric substrate contacts the conductive flanges. Besides the requirement that the sample be flat, the substrate must cover the entire aperture between the cylindrical-cavity and the sample regions.

In the following sections, we represent the electric and magnetic fields in the different split-cylinder regions as a series of normal modes. Using the mode-matching method, we enforce the boundary conditions and derive the resonance condition for the split-cylinder resonator. Using the resonance condition and the expressions for the electric and magnetic fields, we show how to calculate the dielectric substrate's relative permittivity and loss tangent from a measurement of the TE_{0np} resonant frequency and quality factor.

2.2.1 Fields in the Upper Cylindrical-Cavity Region

From the symmetry of the split-cylinder resonator and the assumption that we excite TE_{0n} modes in the upper cylindrical-cavity region, the electric field has only a ϕ-component of the form

$$E_{\phi_u} = \sum_{n=1}^{\infty} A_n U_n R_{n_u}(\rho) Z_{n_u}(z), \tag{2.20}$$

where A_n are unknown mode coefficients, R_{n_u} are radial eigenfunctions to be determined, and Z_{n_u} are longitudinal functions. We also include the factor U_n, a

constant to be defined later for improving matrix conditioning. Assuming that A_n and U_n are nonzero for all n, we substitute (2.20) into the vector wave equation

$$\nabla^2 \vec{E} + \omega^2 \mu_0 \epsilon_0 \epsilon_a^{'} \vec{E} = 0 \tag{2.21}$$

to obtain

$$\frac{1}{R_{n_u}} \frac{1}{\rho} \frac{\partial}{\partial \rho} \left(\rho \frac{\partial R_{n_u}}{\partial \rho} \right) - \frac{1}{\rho^2} + k_u^2 = -\frac{1}{Z_{n_u}} \frac{\partial^2 Z_{n_u}}{\partial z^2} = k_n^2, \tag{2.22}$$

where $k_u^2 = \omega^2 \mu_0 \epsilon_0 \epsilon_a^{'}$, $\omega = 2\pi f$, k_n^2 is the separation constant, f is the frequency, and $\epsilon_a^{'}$ is the relative permittivity of the air within the upper cylindrical-cavity region. We have assumed that the fields have a time-dependence of $e^{j\omega t}$.

We use the method of separation of variables to solve for $R_{n_u}(\rho)$ and $Z_{n_u}(z)$. Applying this method to (2.22) we find

$$\begin{aligned} E_{\phi_u}(\rho, z) \;\; = \;\; & \sum_{n=1}^{\infty} A_n U_n \left[C_n^{'} J_1(h_{n_u}\rho) + D_n^{'} Y_1(h_{n_u}\rho) \right] \cdot \\ & \left[A_n^{'} \sin[p_{n_u}(L + \frac{d}{2} - z)] + B_n^{'} \cos[p_{n_u}(L + \frac{d}{2} - z)] \right] \end{aligned} \tag{2.23}$$

where $A_n^{'}$, $B_n^{'}$,$C_n^{'}$, and $D_n^{'}$ are constants, J_1 is the Bessel function of the first kind of order one, Y_1 is the Bessel function of the second kind of order two, and $p_{n_u}^2 = k_u^2 - h_{n_u}^2$.

We assume that the metal waveguide wall and endplate of the cylindrical-cavity section are perfect conductors. Therefore, the boundary conditions on the transverse electric field yield

$$E_{\phi_u}(\rho, z = L + \frac{d}{2}) = 0, \qquad 0 \le \rho \le a, \tag{2.24}$$

$$E_{\phi_u}(\rho = 0, z) \text{ is finite}, \qquad 0 \le z \le L + \frac{d}{2}, \tag{2.25}$$

$$E_{\phi_u}(\rho = a, z) = 0, \qquad \frac{d}{2} \le z \le L + \frac{d}{2}. \tag{2.26}$$

It follows that

$$B_n^{'} = 0, \tag{2.27}$$

$$D_n^{'} = 0, \tag{2.28}$$

$$h_{n_u} = \frac{j_{1,n}}{a}, \tag{2.29}$$

where $j_{1,n}$ is the nth zero of J_1 and (2.23) reduces to

$$E_{\phi_u}(\rho, z) = \sum_{n=1}^{\infty} A_n U_n J_1(h_{n_u}\rho) \sin[p_{n_u}(L + \frac{d}{2} - z)]. \tag{2.30}$$

From the differential form of Faraday's law

$$\nabla \times \vec{E} = -j\omega\mu_0 \vec{H} \tag{2.31}$$

and (2.30) we find the components of the magnetic field

$$H_{\rho_u}(\rho, z) = -\frac{1}{j\omega\mu_0} \sum_{n=1}^{\infty} p_{n_u} A_n U_n J_1(h_{n_u}\rho) \cos[p_{n_u}(L + \frac{d}{2} - z)], \tag{2.32}$$

$$H_{z_u}(\rho, z) = -\frac{1}{j\omega\mu_0} \sum_{n=1}^{\infty} h_{n_u} A_n U_n J_0(h_{n_u}\rho) \sin[p_{n_u}(L + \frac{d}{2} - z)]. \tag{2.33}$$

2.2.2 Fields in the Sample Region

Although the split-cylinder resonator is not a closed cavity, we assume a perfectly-conducting boundary at the sample radius $\rho = b$ in order to implement the mode-matching method. The value of b must be large enough to ensure the attenuation of the electric and magnetic fields before they reach this proposed conductive boundary. Later in this section, we examine the value of b and investigate its effect on the calculation of the relative permittivity and loss tangent.

We assume that the electric field in the sample region takes the form

$$E_{\phi_s} = \sum_{n=1}^{\infty} B_n V_n R_{n_s}(\rho) Z_{n_s}(z), \tag{2.34}$$

where B_n are unknown mode coefficients, R_{n_s} are radial eigenfunctions to be determined, and Z_{n_s} are longitudinal functions. We add a factor V_n to improve matrix conditioning.

Assuming that B_n and V_n are nonzero for all n, we substitute (2.34) into the vector wave equation

$$\nabla^2 \vec{E} + \omega^2 \mu_0 \epsilon_0 \epsilon_s^{'} \vec{E} = 0 \tag{2.35}$$

to obtain

$$\frac{1}{R_{n_s}} \frac{1}{\rho} \frac{\partial}{\partial \rho} \left(\rho \frac{\partial R_{n_s}}{\partial \rho} \right) - \frac{1}{\rho^2} + k_s^2 = -\frac{1}{Z_{n_s}} \frac{\partial^2 Z_{n_s}}{\partial z^2} = k_n^2, \tag{2.36}$$

where $k_s^2 = \omega^2 \mu_0 \epsilon_0 \epsilon_s^{'}$, k_n^2 is the separation constant, and $\epsilon_s^{'}$ is the relative permittivity of the sample.

We use the method of separation of variables to solve for $R_{n_s}(\rho)$ and $Z_{n_s}(z)$. Applying this method to (2.36) we find

$$\begin{aligned} E_{\phi_s}(\rho, z) &= \sum_{n=1}^{\infty} B_n V_n \left[C_n^{'} J_1(h_{n_s}\rho) + D_n^{'} Y_1(h_{n_s}\rho) \right] \cdot \\ &\quad \left[A_n^{'} \sin(p_{n_s} z) + B_n^{'} \cos(p_{n_s} z) \right], \end{aligned} \tag{2.37}$$

where $A_n^{'}$, $B_n^{'}$,$C_n^{'}$, and $D_n^{'}$ are constants, J_1 is the Bessel function of the first kind of order one, Y_1 is the Bessel function of the second kind of order two, and $p_{n_s}^2 = k_s^2 - h_{n_s}^2$.

To increase the sensitivity of the split-cylinder resonator, the electric field should be maximum in the sample region. Therefore, we consider only TE_{0np} resonant modes where p, the number of half-wavelengths along the z-axis, is an odd integer. For this mode family, the electric field is symmetric about $z = 0$ and maximum at $z = 0$, the center of the sample.

We also assume that the flanges of the cylindrical-cavity regions are perfect conductors. Given these assumptions, the boundary conditions on the transverse electric field yield

$$E_{\phi_s}(\rho, z = -\frac{d}{2}) = E_{\phi_s}(\rho, z = \frac{d}{2}), \qquad 0 \le \rho \le b, \tag{2.38}$$

$$E_{\phi_s}(\rho = 0, z) \text{ is finite}, \qquad 0 \le z \le \frac{d}{2}, \tag{2.39}$$

$$E_{\phi_s}(\rho = b, z) = 0, \qquad 0 \le z \le \frac{d}{2}. \tag{2.40}$$

It follows that

$$A_n^{'} = 0, \tag{2.41}$$

$$D_n^{'} = 0, \tag{2.42}$$

$$h_{n_s} = \frac{j_{1,n}}{b}, \tag{2.43}$$

where $j_{1,n}$ is the nth zero of J_1 and (2.37) reduces to

$$E_{\phi_s}(\rho, z) = \sum_{n=1}^{\infty} B_n V_n J_1(h_{n_s}\rho)\cos(p_{n_s}z). \tag{2.44}$$

From the differential form of Faraday's law

$$\nabla \times \vec{E} = -j\omega\mu_0\vec{H} \tag{2.45}$$

and (2.44) we find the components of the magnetic field

$$H_{\rho_s}(\rho, z) = -\frac{1}{j\omega\mu_0}\sum_{n=1}^{\infty} p_{n_s} B_n V_n J_1(h_{n_s}\rho)\sin(p_{n_s}z) \tag{2.46}$$

$$H_{z_s}(\rho, z) = -\frac{1}{j\omega\mu_0}\sum_{n=1}^{\infty} h_{n_s} B_n V_n J_0(h_{n_s}\rho)\cos(p_{n_s}z) \tag{2.47}$$

2.2.3 Resonance Condition

In the previous two sections, we derived expressions for the electric and magnetic fields in the upper cylindrical-cavity and sample regions. Because of the symmetry of the split-cylinder resonator at $z = 0$, these are the only two regions that we need to consider. We now derive the resonance condition for the split-cylinder resonator by enforcing the boundary conditions on the transverse fields in the aperture region separating the cylindrical-cavity and sample regions, integrating over the boundary surface, and making use of the orthogonality relations of the normal modes in both regions.

First we enforce the boundary condition that the tangential electric field is continuous at $z = d/2$

$$E_{\phi_u}\left(z = \frac{d}{2}\right) = E_{\phi_s}\left(z = \frac{d}{2}\right), \quad 0 \le \rho \le b. \tag{2.48}$$

Substituting (2.30) and (2.44) into (2.48) we find

$$\sum_{n=1}^{\infty} B_n V_n J_1(h_{n_s}\rho)\cos(p_{n_s}\frac{d}{2}) = \begin{cases} \sum_{n=1}^{\infty} A_n U_n J_1(h_{n_u}\rho)\sin(p_{n_u}L), & 0 \le \rho \le a \\ 0, & a \le \rho \le b. \end{cases} \tag{2.49}$$

To reduce the infinite sum on the left-hand side of (2.49) to a single term, we make use of the orthogonality of the modes. With the assumption that the conductive boundaries are perfectly conducting and all materials within the split-cylinder resonator are lossless [9], the orthogonality relation for the upper cylindrical-cavity region is

$$\int_{\phi=0}^{2\pi}\int_{\rho=0}^{a}\left[E_{\phi_u}^{(n)} \times H_{\rho_u}^{(m)}\right]\cdot \vec{a}_z \rho\, d\rho\, d\phi = F\delta_{mn}, \tag{2.50}$$

and the relation for the sample region is

$$\int_{\phi=0}^{2\pi}\int_{\rho=0}^{b}\left[E_{\phi_s}^{(n)} \times H_{\rho_s}^{(m)}\right]\cdot \vec{a}_z \rho\, d\rho\, d\phi = G\delta_{mn}, \tag{2.51}$$

where F and G are normalization constants and δ_{mn} is the Kronecker delta function.

To reduce (2.49), we can multiply both sides by either $H_{\rho_u}^{(m)}$ and use the orthogonality relation in equation (2.50), or we can multiply by $H_{\rho_s}^{(m)}$ and use the orthogonality relation in equation (2.51). The electric field must not only be continuous at the aperture ($0 \le \rho \le a$) at $z = d/2$, but it also must go to zero on the perfectly conductive flange that extends to $\rho = b$. Only the orthogonality relation for the modes in the sample region will allow us to enforce the electric field boundary condition over the entire boundary from ($0 \le \rho \le b$) [10]. Therefore, multiplying both sides of (2.49) by $H_{\rho_s}^{(m)}$ and integrating over the cross-section of the sample region we find

$$\sum_{n=1}^{\infty} A_n U_n \frac{a h_{nu}}{h_{ms}^2 - h_{nu}^2} J_0(h_{nu}a) J_1(h_{ms}a)\sin(p_{nu}L) = B_m V_m \frac{b^2}{2} J_0^2(h_{ms}b)\cos(p_{ms}\frac{d}{2}). \tag{2.52}$$

The second boundary condition that we enforce is the continuity of the tangential magnetic field

$$H_{\rho_s}\left(z=\frac{d}{2}\right)=H_{\rho_u}\left(z=\frac{d}{2}\right),\ \ 0\le\rho\le a. \tag{2.53}$$

Substituting (2.32) and (2.46) into (2.53) we find

$$\sum_{n=1}^{\infty}p_{n_s}B_nV_nJ_1(h_{n_s}\rho)\sin(p_{n_s}\frac{d}{2})=\sum_{n=1}^{\infty}p_{n_a}A_nU_nJ_1(h_{n_a}\rho)\cos(p_{n_a}L),\quad 0\le\rho\le a. \tag{2.54}$$

We again employ an orthogonality relation to reduce the infinite sum on the right-hand side of (2.54) to a single term. For the case of the magnetic fields, either of the orthogonality relations found in (2.50) or (2.51) will work in principle. However, according to [11], by selecting the remaining orthogonality relation, we reduce the errors due to relative convergence. Therefore, we use

$$\int_{\phi=0}^{2\pi}\int_{\rho=0}^{a}\left[E_{\phi_u}^{(n)}\times H_{\rho_u}^{(m)}\right]\cdot\vec{a}_z\rho\,d\rho\,d\phi=F\delta_{mn}. \tag{2.55}$$

Multiplying each side of (2.54) by $E_{\phi_a}^{(n)}$ and integrating over the cross-section of the upper cavity region we find

$$A_nU_np_{n_u}\frac{a^2}{2}J_0^2(h_{n_u}a)\cos(p_{n_u}L)=\sum_{m=1}^{\infty}B_mV_m\frac{ap_{m_s}h_{n_u}}{h_{m_s}^2-h_{n_u}^2}J_1(h_{m_s}a)J_0(h_{n_u}a)\sin(p_{m_s}\frac{d}{2}). \tag{2.56}$$

To match the boundary conditions exactly, we must include an infinite number of modes in both the upper cylindrical-cavity region and the sample region. The result is an infinite system of equations with unknown constants A_n and B_n. To reduce this to a finite system of linear algebraic equations, we must truncate the number of modes in each region. If we choose the number of modes in the cylindrical-cavity region to be N_u and the number of modes in the sample region to be N_s, then (2.53) and (2.56) form two systems of equations

$$\mathbf{QA}=\mathbf{RB} \tag{2.57}$$

and

$$\mathbf{SA} = \mathbf{PB}, \tag{2.58}$$

where

$$Q_{mn} = U_n \frac{a h_{n_u}}{h_{m_s}^2 - h_{n_u}^2} J_1(h_{m_s} a) J_0(h_{n_u} a) \sin(p_{n_u} L), \tag{2.59}$$

$$R_{mm} = V_m \frac{b^2}{2} J_0^2(h_{m_s} b) \cos(p_{m_s} \frac{d}{2}), \tag{2.60}$$

$$S_{nn} = U_n p_{nu} \frac{a^2}{2} J_0^2(h_{nu} a) \cos(p_{nu} L), \tag{2.61}$$

$$P_{nm} = V_m \frac{a p_{ms} h_{na}}{h_{ms}^2 - h_{nu}^2} J_1(h_{ms} a) J_0(h_{nu} a) \sin(p_{ms} \frac{d}{2}) \tag{2.62}$$

noting that both $\mathbf{R}$ and $\mathbf{S}$ are diagonal matrices.

The system of equations represented by (2.57) and (2.58) is rewritten as

$$[\mathbf{Z}]\,[\mathbf{X}] = \mathbf{0}, \tag{2.63}$$

where

$$[\mathbf{Z}] = \begin{bmatrix} \mathbf{Q} & -\mathbf{R} \\ \mathbf{S} & -\mathbf{P} \end{bmatrix} \tag{2.64}$$

and

$$[\mathbf{X}] = \begin{bmatrix} \mathbf{A} \\ \\ \mathbf{B} \end{bmatrix}. \tag{2.65}$$

The resonance condition follows from the fact that this linear system of equations has a nontrivial solution only if

$$\det[\mathbf{Z}] = \mathbf{0}. \tag{2.66}$$

Equation (2.66) can be used to iteratively calculate either the resonant frequency f of the split-cylinder resonator given a known sample permittivity $\epsilon_s^{'}$ or the sample permittivity given a measured resonant frequency.

2.3 Relative Permittivity

In the previous section, we used the mode-matching method to derive the resonance condition for the split-cylinder resonator

$$\det[\mathbf{Z}] = \det\begin{bmatrix} \mathbf{Q} & -\mathbf{R} \\ \mathbf{S} & -\mathbf{P} \end{bmatrix} = 0, \tag{2.67}$$

where

$$Q_{mn} = U_n \frac{a h_{n_u}}{h_{m_s}^2 - h_{n_u}^2} J_1(h_{m_s} a) J_0(h_{n_u} a) \sin(p_{n_u} L), \tag{2.68}$$

$$R_{mm} = V_m \frac{b^2}{2} J_0^2(h_{m_s} b) \cos(p_{m_s} \frac{d}{2}), \tag{2.69}$$

$$S_{nn} = U_n p_{n_u} \frac{a^2}{2} J_0^2(h_{n_u} a) \cos(p_{n_u} L), \tag{2.70}$$

$$P_{nm} = V_m \frac{a p_{m_s} h_{n_u}}{h_{m_s}^2 - h_{n_u}^2} J_1(h_{m_s} a) J_0(h_{n_u} a) \sin(p_{m_s} \frac{d}{2}). \tag{2.71}$$

To use equation (2.67) to calculate the substrate's relative permittivity $\epsilon_s^{'}$, we must first define U_n and V_n. The inclusion of U_n and V_n help to improve the matrix conditioning of $\mathbf{Z}$ by preventing any matrix element from becoming too small or too large relative to the other matrix elements.

The matrices $\mathbf{Q}$ and $\mathbf{S}$ include the trigonometric functions $\sin(p_{n_u} L)$ and $\cos(p_{n_u} L)$. For large n, p_{n_u} is large and imaginary, resulting in large values for $\sin(p_{n_u} L)$ and $\cos(p_{n_u} L)$. Thus, to keep $\mathbf{Q}$ and $\mathbf{S}$ from becoming ill-conditioned, we define U_n as

$$U_n = \frac{p_{N_u}}{\cosh[\mathrm{Im}(p_{n_u}) L]}, \tag{2.72}$$

where p_{N_u} is the value of p_{n_u} when $n = N_u$, the total number of modes included in the cylindrical-cavity region.

In a similar way, the matrices $\mathbf{R}$ and $\mathbf{P}$ include the trigonometric functions $\cos(p_{m_s} \frac{d}{2})$ and $\sin(p_{m_s} \frac{d}{2})$. For large m, p_{n_s} is large and imaginary and $\cos(p_{m_s} \frac{d}{2})$

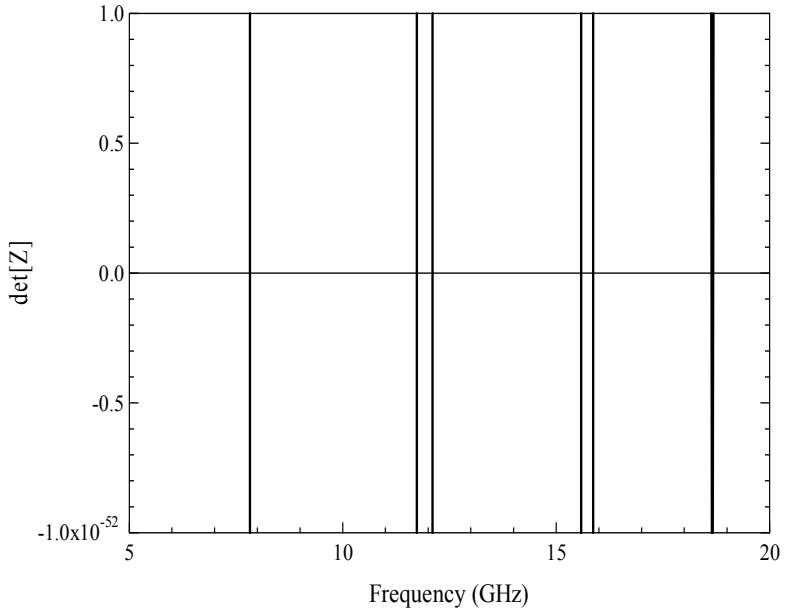

Figure 2.3: Determinant of $\mathbf{Z}$ as a function of resonant frequency. In this example, the sample's relative permittivity is 10, radius is 29.05 mm, and thickness is 1 mm. The length of the upper cylindrical-cavity section is 25.326 mm and the radius is 19.05 mm.

and $\sin(p_{m_s}\frac{d}{2})$ are large as well. To keep $\mathbf{R}$ and $\mathbf{P}$ from becoming ill-conditioned, we define V_n as

$$V_n = \frac{p_{N_s}}{\cosh[\mathrm{Im}(p_{n_s})\frac{d}{2}]}, \tag{2.73}$$

where p_{N_s} is the value of p_{n_s} when $n = N_s$, the total number modes included in the sample region.

With U_n and V_n defined, we can use the split-cylinder resonance condition in (2.67). If the sample's thickness d and radius b are known, along with the cylindrical-cavity section's radius a and length L, only two unknown variables remain in (2.67): the resonant frequency f and the sample's relative permittivity ϵ_s'. Thus, (2.67) can be used in two ways.

The first way is to calculate the resonant frequency of the split-cylinder resonator given the value of the sample's relative permittivity. This is useful for identifying the location of the TE_{0np} modes. Figure 2.3 shows a plot of the

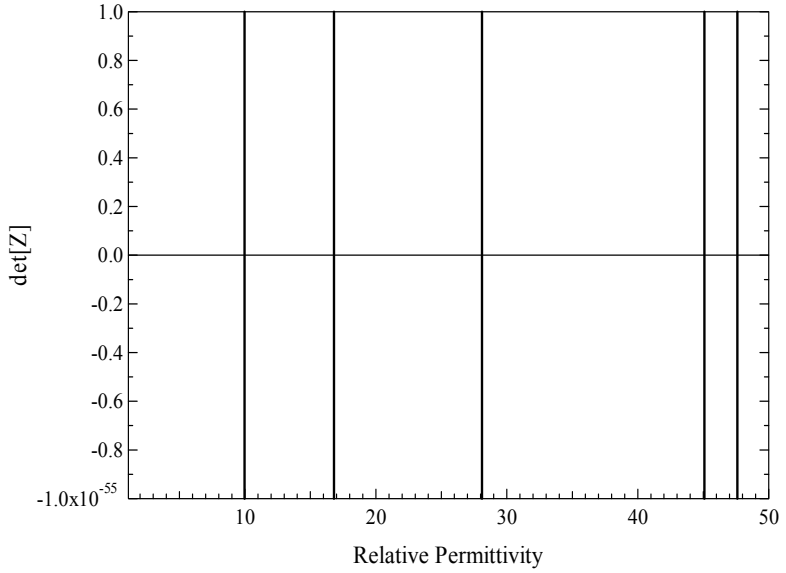

Figure 2.4: Determinant of $\mathbf{Z}$ as a function of relative permittivity $\epsilon_s^{'}$. In this example, the sample's radius is 29.05 mm and thickness is 1 mm. The length of the upper cylindrical-cavity section is 25.326 mm and the radius is 19.05 mm. The split-cylinder's TE_{011} resonant frequency is 7.83 GHz.

determinant of $\mathbf{Z}$ as a function of frequency for a sample with thickness $d = 1$ mm and relative permittivity $\epsilon_s^{'} = 10$.

Each zero crossing in Figure 2.3 corresponds to the resonant frequency of a TE_{0np} mode, where p is odd. The first zero crossing occurs at the resonant frequency of the fundamental TE_{011} mode. Because other resonant modes, besides those in the TE_{0np} family, are excited in the split-cylinder resonator, plotting the determinant of Z versus frequency is an important tool for properly identifying the frequencies of the TE_{0np} modes.

The second, and more important, use of the split-cylinder resonance condition is to the calculation of the value of the sample's relative permittivity $\epsilon_s^{'}$. In this case, the resonant frequency f of the TE_{0np} mode and the dimensions of the sample and cylindrical-cavity sections are known, and we calculate the sample's relative permittivity with (2.67). Figure 2.4 shows a plot of the determinant of Z

as a function of relative permittivity.

With the split-cylinder's resonant frequencies, each zero-crossing of the determinant of Z corresponds to the resonant frequency of a TE_{0np} mode. However, to calculate the sample's relative permittivity, only one of the zero-crossings of the determinant of Z is the true value of the sample's relative permittivity, and the remaining zero-crossings should be ignored. Figure 2.4 is a plot of the determinant of $\mathbf{Z}$ as a function of the sample's relative permittivity with several zero crossings, only one of which corresponds to the true value of sample's relative permittivity of the sample.

Since we cannot solve explicitly for the sample's relative permittivity using (2.67), we must employ an iterative method, in our case the Newton-Raphson technique. With any such iterative method, one must supply an initial guess for the relative permittivity so that the algorithm converges to the correct value of the relative permittivity. It is important to note, as seen in Figure 2.4, that the initial guess must be sufficiently close to the sample's relative permittivity to avoid converging to the wrong zero-crossing. In Chapter 5, we examine several examples to see how close the values of the initial guesses must be. In our particular example, the first-zero crossing in Figure 2.4 is the correct one that corresponds to a relative permittivity of 10.

We must truncate the total number of modes in the upper cylindrical-cavity region N_u and the sample region N_s so that the number of linear algebraic equations is finite. But the truncation of the number of modes leads to a systematic error in the calculation of the sample's relative permittivity. This phenomenon is often referred to as relative convergence and its effect must be minimized for accurate relative permittivity measurements.

To minimize the relative convergence error, we employ all the available orthogonality relations in the derivation of the resonance condition as recommended

by [11]. Although this helps to reduce the relative convergence error, the most effective way of reducing relative convergence is to properly select the optimal ratio of modes in each region.

In our introduction to this chapter, we noted that Ilinski [13] found that the relative convergence is minimized when the wavelength of the highest-order mode in each region is the same. For the split-cylinder resonator, the wavelength of the highest-order evanescent mode in the cylindrical-cavity region is

$$\lambda_u = \frac{2\pi}{\mathrm{Im}[p_{N_u}]}, \tag{2.74}$$

and the wavelength of the highest-order mode in the sample region is

$$\lambda_s = \frac{2\pi}{\mathrm{Im}[p_{N_s}]}, \tag{2.75}$$

where

$$p_{N_u}^2 = \omega^2 \mu_0 \epsilon_0 \epsilon_a^{'} - \left(\frac{j_{1,N_u}}{a}\right)^2 \tag{2.76}$$

and

$$p_{N_s}^2 = \omega^2 \mu_0 \epsilon_0 \epsilon_s^{'} - \left(\frac{j_{1,N_s}}{b}\right)^2. \tag{2.77}$$

The relative convergence is minimized if the number of modes in each region is selected so that

$$\mathrm{Im}[p_{N_u}] = \mathrm{Im}[p_{N_s}]. \tag{2.78}$$

To examine the effect of relative convergence on the calculation of relative permittivity, we show in Figure 2.5 the calculated relative permittivity of a dielectric substrate as a function of the number of modes in the cylindrical-cavity and sample regions. Also shown on this plot is the optimal ratio of modes as defined by (2.78). The calculated relative permittivity can vary several percent depending on selection of the number of modes. However, the variation in permittivity is reduced considerably if the ratio of modes is determined from (2.78).

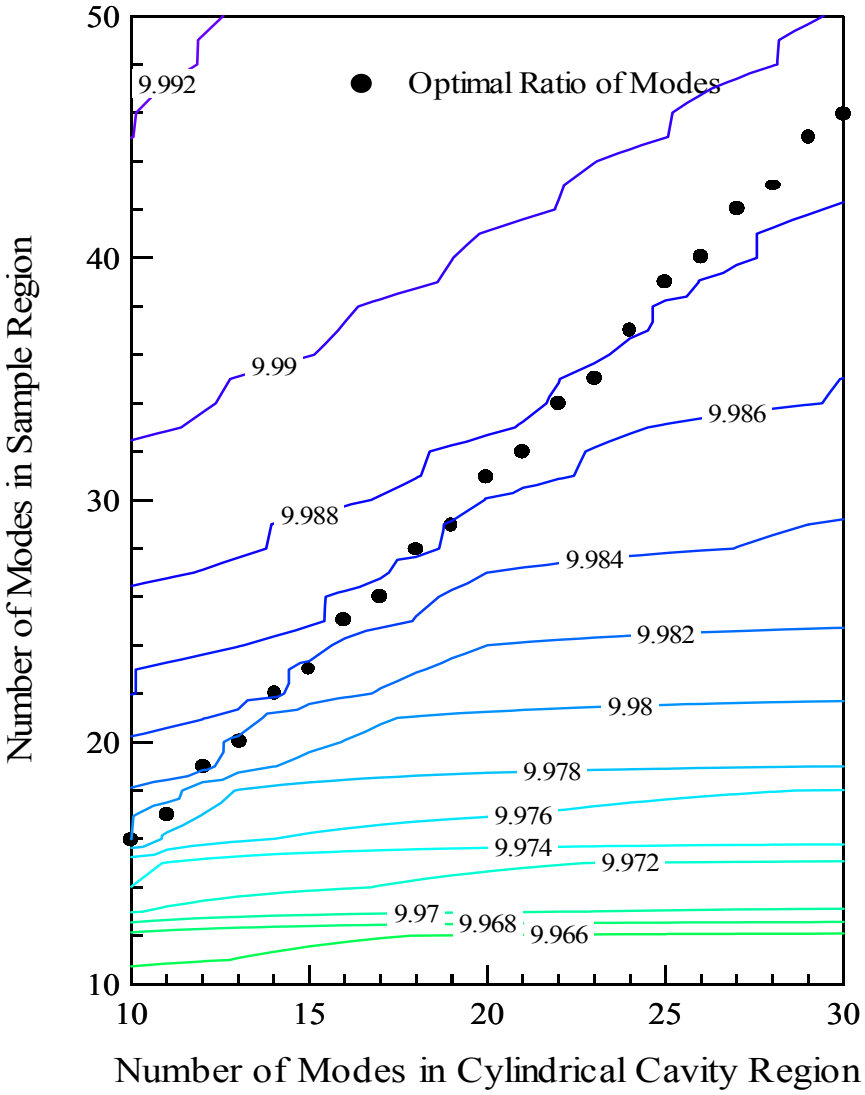

Figure 2.5: Relative permittivity $\epsilon_s^{'}$ as function of the number of modes in the cylindrical-cavity and sample regions. In this example, the sample's radius is 29.05 mm and thickness is 1 mm. The length of the upper cylindrical-cavity section is 25.326 mm and the radius is 19.05 mm. The split-cylinder's TE_{011} resonant frequency is 7.83 GHz.

The total number of modes to achieve numerical convergence may be determined with the same sample and split-cylinder resonator dimensions as specified in Figure 2.5, and using (2.78) to calculate the optimal ratio of modes. By increasing the number of modes in each region, we find the number of modes sufficient to

Number of Modes in Cylindrical-Cavity Region N_u	Number of Modes in Sample Region Region N_s	Sample Relative Permittivity $\epsilon_s^{'}$
4	8	9.9616
6	10	9.9697
8	13	9.9760
10	16	9.9800
12	19	9.9827
14	22	9.9845
16	25	9.9857
18	28	9.9867
20	31	9.8873
22	34	9.8879
24	37	9.9883
26	40	9.9886
28	43	9.9889
30	46	9.9891

Table 2.1: Relative permittivity $\epsilon_s^{'}$ as a function of modes in the cylindrical-cavity and sample regions where the ratio of modes is fixed. In this example, the sample's radius is 29.05 mm and thickness is 1 mm. The length of the upper cylindrical-cavity section is 25.326 mm and the radius is 19.05 mm. The split-cylinder's TE_{011} resonant frequency is 7.83 GHz.

reach numerical convergence. Table 2.1 lists the calculated relative permittivity as a function of the number of modes in the sample and cylindrical-cavity regions. As expected, the values of the computed relative permittivity shown in Table 2.1 vary significantly when the number of modes is small. However, as the total number of modes is increased, the relative permittivity converges, and for $N_u = 30$ and $N_s = 46$, the variation in the relative permittivity is less than 2×10^{-4}. Note that this example is for a particular split-cylinder resonator measuring a substrate with a permittivity near 10 and a thickness of 1 mm. For a different split-cylinder resonator or another dielectric substrate, the total number of modes required to achieve numerical convergence may vary.

In addition to examining the convergence of the relative permittivity as a

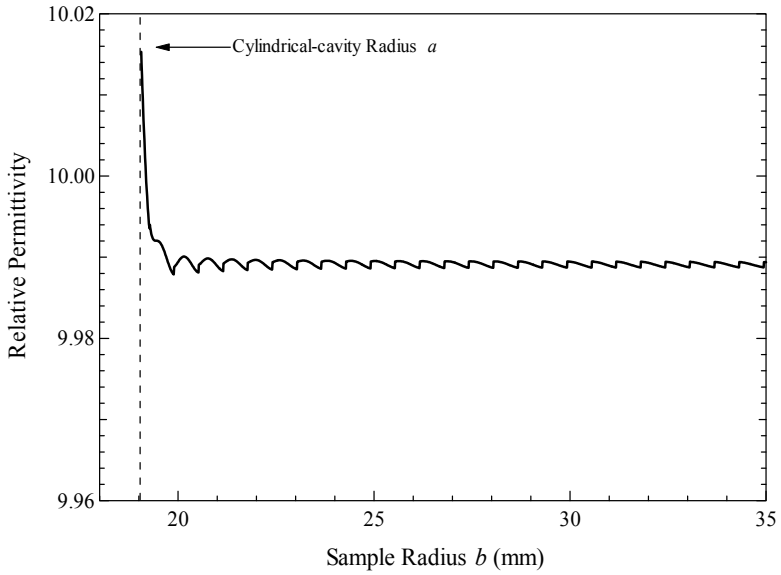

Figure 2.6: Relative permittivity as a function of sample radius b. In this example, the sample's radius is 29.05 mm and thickness is 1 mm. The length of the upper cylindrical-cavity section is 25.326 mm and the radius is 19.05 mm. The split-cylinder's TE_{011} resonant frequency is 7.83 GHz.

function of the number of modes, we also examine the effect of the sample radius b. In our derivation of the resonance condition for the split-cylinder resonator, a perfectly conducting boundary at $\rho = b$ in the sample region is assumed, although no conductive boundary exists physically. To ensure that the addition of this conductive boundary in the theoretical model would not lead to systematic errors, we calculate the relative permittivity as a function of b. Once again, this example assumes the sample's thickness is 1 mm. The length of the upper cylindrical-cavity section is 25.326 mm and the radius is 19.05 mm. The split-cylinder's TE_{011} resonant frequency is 7.83 GHz. The results, shown in Figure 2.6, indicate the calculated relative permittivity as a function of b, beginning with an initial value of b equal to the radius a of the cylindrical-cavity section. In this example, the calculated relative permittivity stabilizes for values of b several millimeters greater than the cylindrical-cavity radius a. This is due to the fact that the

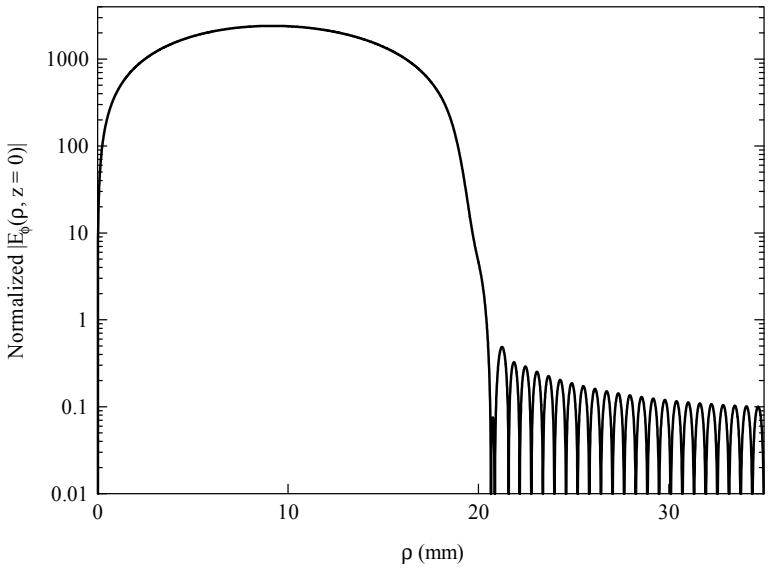

Figure 2.7: Normalized electric field in sample region as a function of ρ. In this example, the sample's radius is 29.05 mm and thickness is 1 mm. The length of the upper cylindrical-cavity section is 25.326 mm and the radius is 19.05 mm. The split-cylinder's TE_{011} resonant frequency is 7.83 GHz.

electric field in the sample region quickly attenuates when $\rho > a$.

Figure 2.7 is a plot of the electric field at $z = 0$ as a function of ρ. We see that the electric field decays rapidly when $\rho > a$, and that the electric field drops several orders of magnitude as ρ increases. Therefore, in order to minimize any effect of the conductive boundary assumed at $\rho = b$, the sample must not only completely cover the cylindrical-cavity sections, but must radially extend further until the electric field has sufficiently attenuated, only a few millimeters in this example.

2.4 Loss Tangent

In the last section, we outlined the method to calculate the sample's relative permittivity from the measured resonant frequency of the split-cylinder resonator and the various dimensions of the sample and cylindrical-cavity sections. Having

characterized these variables, we outline how to calculate the sample's loss tangent $\tan\delta_s$ from a measurement of the TE_{0np} resonant mode's quality factor Q. We define the quality factor Q as

$$Q = \frac{\omega(W_u + W_s)}{P_e + P_w + P_f + P_s}, \tag{2.79}$$

where W_u and W_s are the average energies stored in the cylindrical-cavity and sample regions respectively, and P_e, P_w, P_f, and P_s are the powers dissipated per second in the cylindrical-cavity endplate, wall, flange, and sample respectively. Note that we have ignored the power dissipated in the coupling loops as we ensured that the resonance was very weakly coupled (<-50 dB), an assumption we justify in Section 6.3.1. When we calculated the sample permittivity using (2.66), we also determined the mode coefficients A_n and B_n. With these mode coefficients we calculate the electric and magnetic fields in the upper-cylindrical cavity region

$$E_{\phi_u}(\rho,z) = \sum_{n=1}^{N_u} A_n U_n J_1(h_{n_u}\rho)\sin[p_{n_u}(L+\frac{d}{2}-z)], \tag{2.80}$$

$$H_{\rho_u}(\rho,z) = -\frac{1}{j\omega\mu_0}\sum_{n=1}^{N_u} p_{n_u} A_n U_n J_1(h_{n_u}\rho)\cos[p_{n_u}(L+\frac{d}{2}-z)], \tag{2.81}$$

$$H_z(\rho,z) = -\frac{1}{j\omega\mu_0}\sum_{n=1}^{N_u} h_{n_u} A_n U_n J_0(h_{n_u}\rho)\sin[p_{n_u}(L+\frac{d}{2}-z)], \tag{2.82}$$

and the fields in the sample region

$$E_{\phi_s}(\rho,z) = \sum_{n=1}^{N_s} B_n V_n J_1(h_{n_s}\rho)\cos(p_{n_s}z), \tag{2.83}$$

$$H_{\rho_s}(\rho,z) = -\frac{1}{j\omega\mu_0}\sum_{n=1}^{N_s} p_{n_s} B_n V_n J_1(h_{n_s}\rho)\sin(p_{n_s}z), \tag{2.84}$$

$$H_{z_s}(\rho,z) = -\frac{1}{j\omega\mu_0}\sum_{n=1}^{N_s} h_{n_s} B_n V_n J_0(h_{n_s}\rho)\cos(p_{n_s}z). \tag{2.85}$$

In the derivation of these fields, we assume that all the metal surfaces of the split-cylinder resonator are perfect conductors. This is not the case in the derivation of an expression for the loss tangent, where one assumes that the metal has

a finite conductivity σ and surface resistance R_s. However, for high-conductivity metals, the fields should not significantly differ from those in the case of perfectly-conducting metals, and we use the above expressions for the electric and magnetic fields without modifications.

We define the stored-energy terms W_s and W_u as

$$\begin{aligned} W_s &= \epsilon_0 \epsilon_s^{'} \int_{z=0}^{\frac{d}{2}} \int_{\rho=0}^{b} \int_{\phi=0}^{2\pi} |E_{\phi_s}|^2 \rho \; d\phi \, d\rho \, dz \\ &= \epsilon_0 \epsilon_s^{'} \frac{\pi b^2}{4} \sum_{n=1}^{N_s} |B_n|^2 |V_n|^2 J_0^2(h_{n_s} b) \left[d + \frac{\sin(p_{n_s} d)}{p_{n_s}} \right] \end{aligned} \tag{2.86}$$

and

$$\begin{aligned} W_u &= \epsilon_0 \epsilon_a^{'} \int_{z=\frac{d}{2}}^{L} \int_{\rho=0}^{a} \int_{\phi=0}^{2\pi} |E_{\phi_u}|^2 \rho \; d\phi \, d\rho \, dz \\ &= \begin{cases} -\epsilon_0 \epsilon_a^{'} \dfrac{\pi a^2}{4} \displaystyle\sum_{n=1}^{N_u} |A_n|^2 |U_n|^2 J_0^2(h_{n_u} a) \cdot \\ \qquad \left[d - 2L - \dfrac{\sin(p_{n_u} d)}{p_{n_u}} + \dfrac{\sin(2 p_{n_u} L)}{p_{n_u}} \right], \quad p_{n_u} \text{ is real} \\ \epsilon_0 \epsilon_a^{'} \dfrac{\pi a^2}{4} \displaystyle\sum_{n=1}^{N_u} |A_n|^2 |U_n|^2 J_0^2(h_{n_u} a) \cdot \\ \qquad \left[d - 2L - \dfrac{\sin(p_{n_u} d)}{p_{nu}} + \dfrac{\sin(2 p_{n_u} L)}{p_{n_u}} \right], \quad p_{n_u} \text{ is imaginary.} \end{cases} \end{aligned} \tag{2.87}$$

In the same way, we define the sources of power dissipation as

$$\begin{aligned} P_e &= R_s \int_{\rho=0}^{a} \int_{\phi=0}^{2\pi} |H_{\rho_u}|^2 \rho \; d\phi \, d\rho \, \Big|_{z=L} \\ &= R_s \frac{\pi a^2}{\omega^2 \mu_0^2} \sum_{n=1}^{N_u} |A_n|^2 |U_n|^2 J_0^2(h_{n_u} a) \left| \cos(p_{n_u} \frac{d}{2}) \right|^2 \end{aligned} \tag{2.88}$$

$$P_w = R_s \int_{z=\frac{d}{2}}^{L} \int_{\phi=0}^{2\pi} |H_{z_u}|^2 \rho \; d\phi \, dz \, \Big|_{\rho=a} \tag{2.89}$$

$$= \begin{cases} -R_s \dfrac{\pi a}{2\omega^2\mu_0^2} \displaystyle\sum_{n=1}^{N_u} |A_n|^2 |U_n|^2 h_{n_u}^2 J_0^2(h_{n_u} a) \cdot \\ \qquad \left[d - 2L - \dfrac{\sin(p_{n_u} d)}{p_{n_u}} + \dfrac{\sin(2p_{n_u} L)}{p_{n_u}} \right], & p_{n_u} \text{ is real} \\ R_s \dfrac{\pi a}{2\omega^2\mu_0^2} \displaystyle\sum_{n=1}^{N_u} |A_n|^2 |U_n|^2 h_{n_u}^2 J_0^2(h_{n_u} a) \cdot \\ \qquad \left[d - 2L - \dfrac{\sin(p_{n_u} d)}{p_{n_u}} + \dfrac{\sin(2p_{n_u} L)}{p_{n_u}} \right], & p_{n_a} \text{ is imaginary} \end{cases}$$

$$\begin{aligned} P_f &= R_s \int_{\rho=a}^{b} \int_{\phi=0}^{2\pi} |H_{\rho_s}|^2 \rho \; d\phi \, d\rho \, \Big|_{z=\frac{d}{2}} \qquad (2.90) \\ &= R_s \frac{\pi}{\omega^2\mu_0^2} \sum_{n=1}^{N_s} |B_n|^2 |V_n|^2 \Big\{ b^2 J_0^2(h_{n_s} b) - a^2 [J_1(h_{n_a} a) - J_1(h_{n_s} a)]^2 \Big\} \left| \sin(p_{ns} \frac{d}{2}) \right|^2 \end{aligned}$$

and

$$\begin{aligned} P_s &= \tan\delta \, \omega \epsilon_0 \epsilon_s^{'} \int_{\rho=0}^{b} \int_{z=0}^{\frac{d}{2}} \int_{\phi=0}^{2\pi} |E_{\phi_s}|^2 \rho \; d\phi \, d\rho \, dz \qquad (2.91) \\ &= \tan\delta \, \epsilon_0 \epsilon_s^{'} \frac{\pi b^2 \omega}{4} \sum_{n=1}^{N_s} |B_n|^2 |V_n|^2 J_0^2(h_{n_s} b) \left[d + \frac{\sin(p_{n_s} d)}{p_{ns}} \right] \end{aligned}$$

Solving (2.79) in terms of the sample's loss tangent $\tan\delta$, we find

$$\tan\delta = \frac{\dfrac{\omega(W_s + W_a)}{Q} - P_e - P_w - P_f}{\epsilon_0 \epsilon_s^{'} \dfrac{\pi b^2 \omega}{4} \displaystyle\sum_{n=1}^{N_s} |B_n|^2 |V_n|^2 J_0^2(h_{n_s} b) \left[d + \dfrac{\sin(p_{n_s} d)}{p_{n_s}} \right]}. \qquad (2.92)$$

With the measured resonant frequency and quality factor, the calculated sample's relative permittivity $\epsilon_s^{'}$, and the dimensions of the cylindrical-cavity and sample, the only two unknown variables in (2.92) are R_s, the surface resistivity of the cylindrical-cavity sections, and $\tan\delta$, the loss tangent of the sample. As outlined in Section 6.3.4, we obtain R_s from a measurement of the quality factor of the split-cylinder resonator, when there is no sample and the gap between the two cylindrical-cavity sections is closed ($d = 0$). Once we have calculated R_s, we use equation (2.92) to explicitly calculate the sample's loss tangent.

As was the case with the calculation of the sample's relative permittivity, we must examine the convergence of the loss tangent. First, we consider the effect

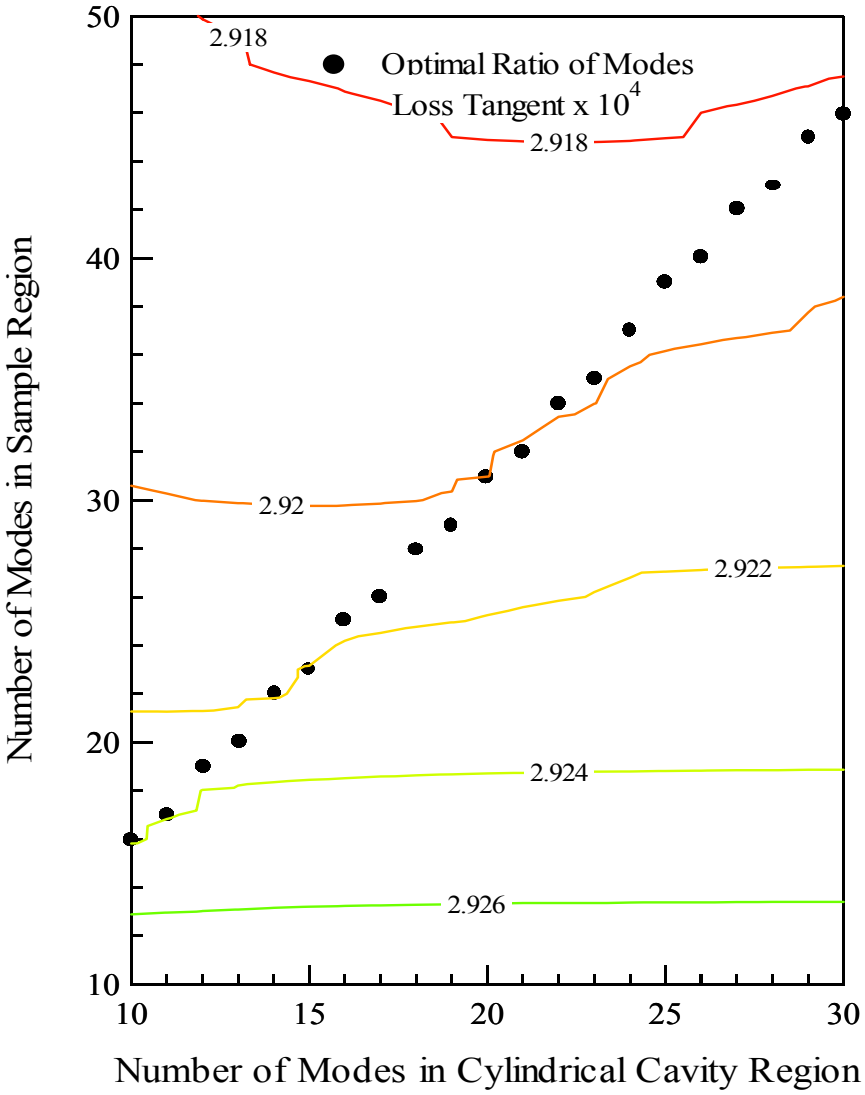

Figure 2.8: Loss tangent as a function of modes in the cylindrical-cavity and sample regions. In this example, the sample's radius is 29.05 mm and thickness is 1 mm. The length of the upper cylindrical-cavity section is 25.326 mm and the radius is 19.05 mm. The split-cylinder's TE_{011} resonant frequency is 7.83 GHz.

of relative convergence using the example in Section 2.3. The sample's thickness is 1 mm, the radius is 29.05 mm and the relative permittivity is 10. The length of the upper cylindrical-cavity section is 25.326 mm, the radius is 19.05 mm, and the surface resistance of the metal is 0.026 Ω/m^2. The split-cylinder's TE_{011} resonant

Number of Modes in Cylindrical-Cavity Region N_u	Number of Modes in Sample Region Region N_s	Sample Loss Tangent $\tan\delta \times 10^4$
4	8	2.929
6	10	2.927
8	13	2.925
10	16	2.924
12	19	2.923
14	22	2.922
16	25	2.921
18	28	2.920
20	31	2.920
22	34	2.920
24	37	2.919
26	40	2.919
28	43	2.919
30	46	2.918

Table 2.2: Loss tangent as a function of the number of modes in the cylindrical-cavity and sample regions where the ratio of modes is fixed.

frequency is 7.83 GHz and the quality factor is 5000.

We calculate the loss tangent as a function of the number of modes in the cylindrical-cavity and sample regions and plot the results in Figure 2.8. Unlike the variation in the relative permittivity, with variation of several percent, the effect on the loss tangent variation is much smaller, less than one percent. Using the criteria in equation (2.78) to select the optimal ratio of modes in each region, we can minimize this small error, due to relative convergence, on the loss tangent.

With the optimal ratio of modes found, we examine the convergence of the loss tangent as a function of the total number of modes in each region. Using the same values for the example shown in Figure 2.8, and fixing the optimal ratio of modes as determined by (2.78), we increase the number of modes in each region to find how many modes are sufficient to reach numerical convergence. Table 2.2

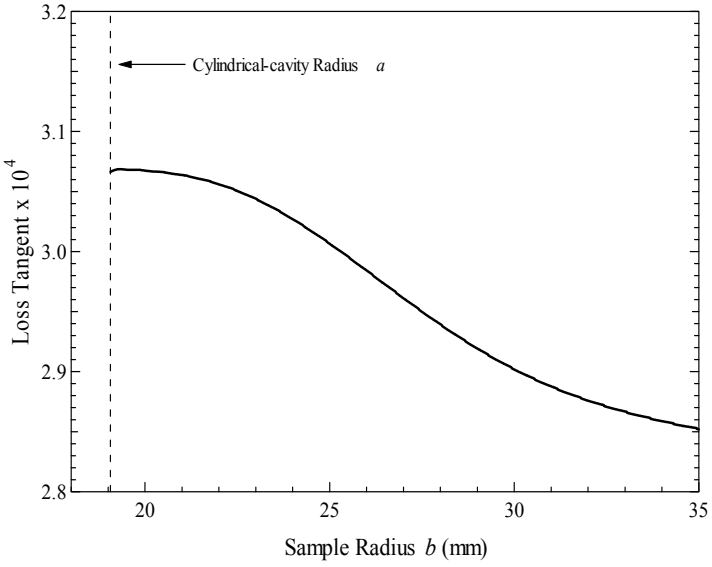

Figure 2.9: Loss tangent as a function of the radius of the sample region.

lists the calculated relative permittivity as a function of the number of modes in the sample and cylindrical-cavity regions. The value of loss tangent converges quickly as the number of modes increases, and shows changes less than 1×10^{-6} when $N_u = 30$ and $N_s = 46$.

The effect of the conductive boundary at $\rho = b$ on the calculation of the loss tangent is shown in Figure 2.9, a plot of the loss tangent as a function of b, the radius of the sample region. Unlike the relative permittivity, the loss tangent does not rapidly stabilize for values of b slightly larger than a, the radius of the cylindrical-cavity section, but decreases with increasing values of b. We believe this is due to the fact that the tangential magnetic field on the conductive flange $H_{\rho_s}(\rho, z = d/2)$ slowly decays as ρ increases. Although the magnetic field, as shown in Figure 2.10, decreases as a function of ρ, it is reduced by only an order of magnitude even when b is over a centimeter larger than a.

An important term in the calculation of the loss tangent is the power dissipated on the conductive flange P_f. Equation (2.90) shows that the conductive

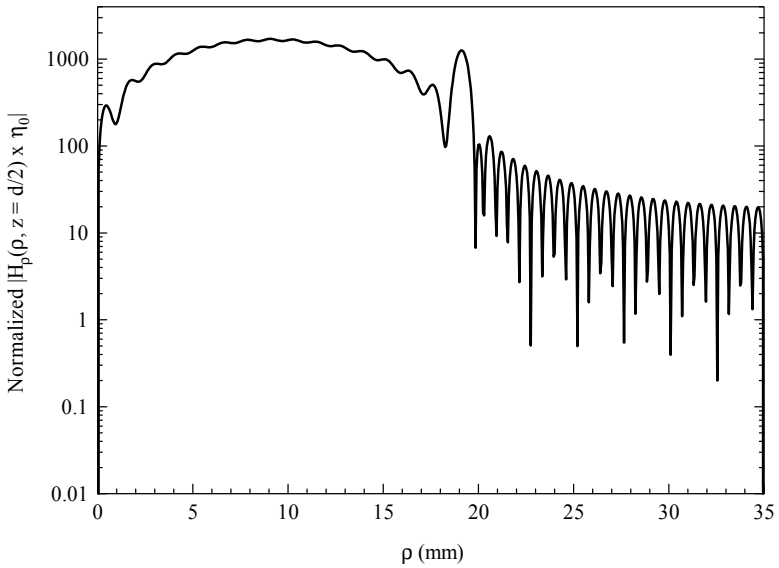

Figure 2.10: Normalized magnetic field along the conductive flange as a function of ρ.

losses on the flange are related to the value of the tangential magnetic field H_{ρ_s}. As b increases, more conductive losses due to the flange are included, and the value of the loss tangent decreases. Although this variation in loss tangent is less than 2×10^{-5} in our example, it is an error that must be included in the uncertainty analysis for the loss tangent.

Chapter 3

Least-Squares Boundary Residual Model

3.1 Introduction

In this chapter we derive a theoretical model for the split-cylinder resonator using the least-squares boundary residual (LSBR) method. Initially used to solve electromagnetic scattering problems [14], the LSBR method was later extended to the solution of eigenvalue problems [15].

Similar to the mode-matching method, the electric and magnetic fields are represented in the various split-cylinder resonator regions as a series of normal modes. However, to derive the resonance condition, the LSBR method differs considerably from the mode-matching method. In the mode-matching method, we obtained a resonance condition by multiplying the boundary condition expressions for the transverse fields by an appropriate mode and integrating over boundary surface, taking into account the orthogonal properties of the modes. In the LSBR method, we define a functional that is constructed from the various boundary conditions on the transverse fields, and a resonance condition is achieved when this functional is minimized.

3.2 Split-Cylinder Theoretical Model

3.2.1 Transverse Electric and Magnetic Fields

We assume the split-cylinder resonator geometry shown in Figure 2.2. This is identical to that in the mode-matching model, including the conductive boundary at the sample radius $\rho = b$. Therefore, we use the expressions for the transverse electric and magnetic fields derived in the previous chapter. From Section 2.2.1, the transverse fields in the upper cylindrical-cavity section of the split-cylinder resonator are

$$E_{\phi_u}(\rho, z) = \sum_{n=1}^{N_u} A_n U_n J_1(h_{n_u}\rho) \sin[p_{n_u}(L + \frac{d}{2} - z)] \tag{3.1}$$

$$= \sum_{n=1}^{N_u} A_n \phi_{n_u} \tag{3.2}$$

$$H_{\rho_u}(\rho, z) = -\frac{1}{j\omega\mu_0} \sum_{n=1}^{N_u} p_{n_u} A_n U_n J_1(h_{n_u}\rho) \cos[p_{n_u}(L + \frac{d}{2} - z)] \tag{3.3}$$

$$= \sum_{n=1}^{N_u} A_n \psi_{n_u} \tag{3.4}$$

where

$$\phi_{n_u} = U_n J_1(h_{n_u}\rho) \sin[p_{n_u}(L + \frac{d}{2} - z)], \tag{3.5}$$

$$\psi_{n_u} = -\frac{1}{j\omega\mu_0} p_{n_u} U_n J_1(h_{n_u}\rho) \cos[p_{n_u}(L + \frac{d}{2} - z)] \tag{3.6}$$

$$U_n = \frac{p_{N_u}}{\cosh[\mathrm{Im}(p_{n_u})L]}, \tag{3.7}$$

$$p_{n_u}^2 = k_u^2 - h_{n_u}^2 \tag{3.8}$$

$$h_{n_u} = \frac{j_{1,n}}{a}, \tag{3.9}$$

and

$$k_u^2 = \omega^2 \mu_0 \epsilon_0 \epsilon_a^{'}. \tag{3.10}$$

Likewise, from Section 2.2.2, the transverse fields in the sample region are

$$E_{\phi_s}(\rho,z) = \sum_{n=1}^{N_s} B_n V_n J_1(h_{n_s}\rho)\cos(p_{n_s}z) \tag{3.11}$$

$$= \sum_{n=1}^{N_s} B_n \phi_{n_s} \tag{3.12}$$

$$H_{\rho_s}(\rho,z) = -\frac{1}{j\omega\mu_0}\sum_{n=1}^{N_s} p_{n_s} B_n V_n J_1(h_{n_s}\rho)\sin(p_{n_s}z) \tag{3.13}$$

$$= \sum_{n=1}^{N_s} B_n \psi_{n_s}, \tag{3.14}$$

where

$$\phi_{n_s} = V_n J_1(h_{n_s}\rho)\cos(p_{n_s}z), \tag{3.15}$$

$$\psi_{n_s} = -\frac{1}{j\omega\mu_0} p_{n_s} V_n J_1(h_{n_s}\rho)\sin(p_{n_s}z), \tag{3.16}$$

$$V_n = \frac{p_{N_s}}{\cosh[\mathrm{Im}(p_{n_s})\frac{d}{2}]}, \tag{3.17}$$

$$p_{n_s}^2 = k_s^2 - h_{n_s}^2, \tag{3.18}$$

$$h_{n_s} = \frac{j_{1,n}}{b}, \tag{3.19}$$

and

$$k_s^2 = \omega^2\mu_0\epsilon_0\epsilon_s^{'}. \tag{3.20}$$

As in the mode-matching model, these fields satisfy Maxwell's equations and all the boundary conditions except for the boundary at $z = d/2$, the intersection of the upper cylindrical-cavity and sample regions. Note that the number of modes is truncated in each region – N_u modes in the upper cylindrical-cavity region and N_s modes in the sample region.

3.2.2 Resonance Condition

To match the boundary conditions at $z = d/2$, we define the functional

$$J(\{A_n\},\{B_n\},k_s) = \int_0^a \int_0^{2\pi} |E_{\phi_u} - E_{\phi_s}|^2 \,\rho\, d\phi\, d\rho \Big|_{z=d/2}$$

$$+ \int_0^a \int_0^{2\pi} W_1^2 |H_{\rho_u} - H_{\rho_s}|^2 \, \rho \, d\phi \, d\rho \Big|_{z=d/2}$$
$$+ \int_a^b \int_0^{2\pi} W_2^2 |0 - E_{\phi_s}|^2 \, \rho \, d\phi \, d\rho \Big|_{z=d/2} \tag{3.21}$$

where W_1 and W_2 are arbitrary weighting constants with units of impedance. The first two terms in (3.21) represent the matching of the tangential electric and magnetic fields over the aperture separating the upper-cylindrical cavity region from the sample region. The third term in (3.21) is the condition that the tangential electric field must be zero on the conductive flange of the split-cylinder resonator.

Substituting the tranverse electric and magnetic fields from both regions into (3.21), we express J in matrix form

$$J\left(\{A_n\}, \{B_n\}, k_s\right) = \overline{\mathbf{x}}\mathbf{Z}\mathbf{x} \tag{3.22}$$

where $\mathbf{x}$ is the row vector $(A_1, A_2 \cdots A_{Nu}, B_1, B_2 \cdots B_{Ns})$ and $\mathbf{Z}$ is a complex Hermitian matrix [15]. The bar indicates a complex conjugate. The matrix $\mathbf{Z}$ is the sum of three matrices that correspond to the three terms in (3.21)

$$\mathbf{Z} = \begin{bmatrix} \mathbf{Z}_{1A} & \mathbf{Z}_{1B} \\ \mathbf{Z}_{1C} & \mathbf{Z}_{1D} \end{bmatrix} + \begin{bmatrix} \mathbf{Z}_{2A} & \mathbf{Z}_{2B} \\ \mathbf{Z}_{2C} & \mathbf{Z}_{2D} \end{bmatrix} + \begin{bmatrix} \mathbf{0} & \mathbf{0} \\ \mathbf{0} & \mathbf{Z}_{3D} \end{bmatrix} \tag{3.23}$$

where

$$\mathbf{Z}_{1A} = \begin{bmatrix} \int_{\phi=0}^{2\pi} \int_{\rho=0}^{a} \phi_{1u} \overline{\phi_{1u}} \, \rho d\rho d\phi & \cdots & \int_{\phi=0}^{2\pi} \int_{\rho=0}^{a} \phi_{1u} \overline{\phi_{N_u u}} \, \rho d\rho d\phi \\ \vdots & \ddots & \vdots \\ \int_{\phi=0}^{2\pi} \int_{\rho=0}^{a} \phi_{N_u u} \overline{\phi_{1u}} \, \rho d\rho d\phi & \cdots & \int_{\phi=0}^{2\pi} \int_{\rho=0}^{a} \phi_{N_u u} \overline{\phi_{N_u u}} \, \rho d\rho d\phi \end{bmatrix}_{z=d/2} \tag{3.24}$$

$$\mathbf{Z}_{1B} = \begin{bmatrix} -\int_{\phi=0}^{2\pi} \int_{\rho=0}^{a} -\phi_{1u} \overline{\phi_{1s}} \, \rho d\rho d\phi & \cdots & -\int_{\phi=0}^{2\pi} \int_{\rho=0}^{a} \phi_{1u} \overline{\phi_{N_s u}} \, \rho d\rho d\phi \\ \vdots & \ddots & \vdots \\ -\int_{\phi=0}^{2\pi} \int_{\rho=0}^{a} -\phi_{N_u u} \overline{\phi_{1s}} \, \rho d\rho d\phi & \cdots & -\int_{\phi=0}^{2\pi} \int_{\rho=0}^{a} \phi_{N_u u} \overline{\phi_{N_s u}} \, \rho d\rho d\phi \end{bmatrix}_{z=d/2} \tag{3.25}$$

$$\mathbf{Z}_{1C} = \begin{bmatrix} -\int_{\phi=0}^{2\pi} \int_{\rho=0}^{a} -\phi_{1s} \overline{\phi_{1u}} \, \rho d\rho d\phi & \cdots & -\int_{\phi=0}^{2\pi} \int_{\rho=0}^{a} \phi_{1s} \overline{\phi_{N_u u}} \, \rho d\rho d\phi \\ \vdots & \ddots & \vdots \\ -\int_{\phi=0}^{2\pi} \int_{\rho=0}^{a} -\phi_{N_s s} \overline{\phi_{1u}} \, \rho d\rho d\phi & \cdots & -\int_{\phi=0}^{2\pi} \int_{\rho=0}^{a} \phi_{N_s s} \overline{\phi_{N_u u}} \, \rho d\rho d\phi \end{bmatrix}_{z=d/2} \tag{3.26}$$

$$\mathbf{Z}_{1D} = \left[\begin{array}{ccc} \int_{\phi=0}^{2\pi}\int_{\rho=0}^{a}\phi_{1s}\overline{\phi_{1s}}\,\rho d\rho d\phi & \cdots & \int_{\phi=0}^{2\pi}\int_{\rho=0}^{a}\phi_{1s}\overline{\phi_{N_s u}}\,\rho d\rho d\phi \\ \vdots & \ddots & \vdots \\ \int_{\phi=0}^{2\pi}\int_{\rho=0}^{a}\phi_{N_s u}\overline{\phi_{1s}}\,\rho d\rho d\phi & \cdots & \int_{\phi=0}^{2\pi}\int_{\rho=0}^{a}\phi_{N_s u}\overline{\phi_{N_s u}}\,\rho d\rho d\phi \end{array}\right]_{z=d/2} \tag{3.27}$$

$$\mathbf{Z}_{2A} = \left[\begin{array}{ccc} \int_{\phi=0}^{2\pi}\int_{\rho=0}^{a}\psi_{1u}\overline{\psi_{1u}}\,\rho d\rho d\phi & \cdots & \int_{\phi=0}^{2\pi}\int_{\rho=0}^{a}\psi_{1u}\overline{\psi_{N_u u}}\,\rho d\rho d\phi \\ \vdots & \ddots & \vdots \\ \int_{\phi=0}^{2\pi}\int_{\rho=0}^{a}\psi_{N_u u}\overline{\psi_{1u}}\,\rho d\rho d\phi & \cdots & \int_{\phi=0}^{2\pi}\int_{\rho=0}^{a}\psi_{N_u u}\overline{\psi_{N_u u}}\,\rho d\rho d\phi \end{array}\right]_{z=d/2} \tag{3.28}$$

$$\mathbf{Z}_{2B} = \left[\begin{array}{ccc} -\int_{\phi=0}^{2\pi}\int_{\rho=0}^{a}-\psi_{1u}\overline{\psi_{1s}}\,\rho d\rho d\phi & \cdots & -\int_{\phi=0}^{2\pi}\int_{\rho=0}^{a}\psi_{1u}\overline{\psi_{N_s u}}\,\rho d\rho d\phi \\ \vdots & \ddots & \vdots \\ -\int_{\phi=0}^{2\pi}\int_{\rho=0}^{a}-\psi_{N_u u}\overline{\psi_{1s}}\,\rho d\rho d\phi & \cdots & -\int_{\phi=0}^{2\pi}\int_{\rho=0}^{a}\psi_{N_u u}\overline{\psi_{N_s u}}\,\rho d\rho d\phi \end{array}\right]_{z=d/2} \tag{3.29}$$

$$\mathbf{Z}_{2C} = \left[\begin{array}{ccc} -\int_{\phi=0}^{2\pi}\int_{\rho=0}^{a}-\psi_{1s}\overline{\psi_{1u}}\,\rho d\rho d\phi & \cdots & -\int_{\phi=0}^{2\pi}\int_{\rho=0}^{a}\psi_{1s}\overline{\psi_{N_u u}}\,\rho d\rho d\phi \\ \vdots & \ddots & \vdots \\ -\int_{\phi=0}^{2\pi}\int_{\rho=0}^{a}-\psi_{N_s s}\overline{\psi_{1u}}\,\rho d\rho d\phi & \cdots & -\int_{\phi=0}^{2\pi}\int_{\rho=0}^{a}\psi_{N_s s}\overline{\psi_{N_u u}}\,\rho d\rho d\phi \end{array}\right]_{z=d/2} \tag{3.30}$$

$$\mathbf{Z}_{2D} = \left[\begin{array}{ccc} \int_{\phi=0}^{2\pi}\int_{\rho=0}^{a}\psi_{1s}\overline{\psi_{1s}}\,\rho d\rho d\phi & \cdots & \int_{\phi=0}^{2\pi}\int_{\rho=0}^{a}\psi_{1s}\overline{\psi_{N_s u}}\,\rho d\rho d\phi \\ \vdots & \ddots & \vdots \\ \int_{\phi=0}^{2\pi}\int_{\rho=0}^{a}\psi_{N_s u}\overline{\psi_{1s}}\,\rho d\rho d\phi & \cdots & \int_{\phi=0}^{2\pi}\int_{\rho=0}^{a}\psi_{N_s u}\overline{\psi_{N_s u}}\,\rho d\rho d\phi \end{array}\right]_{z=d/2} \tag{3.31}$$

$$\mathbf{Z}_{3D} = \left[\begin{array}{ccc} \int_{\phi=0}^{2\pi}\int_{\rho=a}^{b}\phi_{1s}\overline{\phi_{1s}}\,\rho d\rho d\phi & \cdots & \int_{\phi=0}^{2\pi}\int_{\rho=a}^{b}\phi_{1s}\overline{\phi_{N_s u}}\,\rho d\rho d\phi \\ \vdots & \ddots & \vdots \\ \int_{\phi=0}^{2\pi}\int_{\rho=a}^{b}\phi_{N_s u}\overline{\phi_{1s}}\,\rho d\rho d\phi & \cdots & \int_{\phi=0}^{2\pi}\int_{\rho=a}^{b}\phi_{N_s u}\overline{\phi_{N_s u}}\,\rho d\rho d\phi \end{array}\right]_{z=d/2} \tag{3.32}$$

and

$$\int_{\phi=0}^{2\pi}\int_{\rho=0}^{a}\phi_{mu}\overline{\phi_{nu}}\,\rho d\rho d\phi = \begin{cases} \pi a^2 U_m\overline{U_m}\sin(p_{m_u}L)\sin(\overline{p_{m_u}}L)J_0^2(h_{m_u}a), & (m=n) \\ 0, & (m\neq n) \end{cases} \tag{3.33}$$

$$-\int_{\phi=0}^{2\pi}\int_{\rho=0}^{a}\phi_{ms}\overline{\phi_{nu}}\,\rho d\rho d\phi = \\ -2\pi\overline{U_n}V_m\sin(\overline{p_{n_u}}L)\cos(p_{m_s}\tfrac{d}{2})\tfrac{ah_{n_u}}{h_{m_s}^2-h_{n_u}^2}J_0(h_{n_u}a)J_1(h_{m_s}a) \tag{3.34}$$

$$-\int_{\phi=0}^{2\pi}\int_{\rho=0}^{a}\phi_{mu}\overline{\phi_{ns}}\,\rho d\rho d\phi = \\ 2\pi U_m\overline{V_n}\cos(\overline{p_{n_s}}\tfrac{d}{2})\sin(p_{m_u}L)\tfrac{ah_{m_u}}{h_{m_u}^2-h_{n_s}^2}J_0(h_{m_u}a)J_1(h_{n_s}a) \tag{3.35}$$

$$\int_{\phi=0}^{2\pi}\int_{\rho=0}^{a}\phi_{ms}\overline{\phi_{ns}}\,\rho d\rho d\phi = \\ \begin{cases} \pi a^2 V_m\overline{V_m}\cos(p_{m_s}\frac{d}{2})\cos(\overline{p_{m_s}}\frac{d}{2}) \\ \qquad\cdot\Big[J_1^2(h_{m_s}a)-\frac{2}{h_{m_s}a}J_0(h_{m_s}a)J_1(h_{m_s}a)+J_0^2(h_{m_s}a)\Big] \quad (m=n) \\ 2\pi V_m\overline{V_n}\cos(p_{m_s}\frac{d}{2})\cos(\overline{p_{n_s}}\frac{d}{2})\dfrac{a}{h_{m_s}^2-h_{n_s}^2} \\ \qquad\cdot[h_{n_s}J_0(h_{n_s}a)J_1(h_{m_s}a)-h_{m_s}J_0(h_{m_s}a)J_1(h_{n_s}a)] \quad (m\neq n) \end{cases} \tag{3.36}$$

$$\int_{\phi=0}^{2\pi}\int_{\rho=a}^{b}\phi_{ms}\overline{\phi_{ns}}\,\rho d\rho d\phi = \\ \begin{cases} \pi V_m\overline{V_m}\cos(p_{m_s}\frac{d}{2})\cos(\overline{p_{m_s}}\frac{d}{2}) \\ \qquad\cdot\Big\{b^2J_0^2(h_{m_s}b)-a^2[J_1^2(h_{m_s}a)-\frac{2}{h_{m_s}a}J_0(h_{m_s}a)J_1(h_{m_s}a)+J_0^2(h_{m_s}a)]\Big\} \quad (m=n) \\ -2\pi V_m\overline{V_n}\cos(p_{m_s}\frac{d}{2})\cos(\overline{p_{n_s}}\frac{d}{2})\frac{a}{h_{m_s}^2-h_{n_s}^2} \\ \qquad\cdot[h_{n_s}J_0(h_{n_s}a)J_1(h_{m_s}a)-h_{m_s}J_0(h_{m_s}a)J_1(h_{n_s}a)] \quad (m\neq n) \end{cases} \tag{3.37}$$

$$\int_{\phi=0}^{2\pi}\int_{\rho=0}^{a}\psi_{mu}\overline{\psi_{nu}}\,\rho d\rho d\phi = \\ \begin{cases} \dfrac{\pi a^2}{\omega^2\mu_0^2}U_m\overline{U_m}p_{m_u}\overline{p_{m_u}}\cos(p_{m_u}L)\cos(\overline{p_{m_u}}L)J_0^2(h_{m_u}a), & (m=n) \\ 0, & (m\neq n) \end{cases} \tag{3.38}$$

$$-\int_{\phi=0}^{2\pi}\int_{\rho=0}^{a}\psi_{ms}\overline{\psi_{nu}}\,\rho d\rho d\phi = \frac{-2\pi}{\omega^2\mu_0^2}\overline{U_n}V_m p_{m_s}\overline{p_{n_u}}\cos(\overline{p_{n_u}}L)\sin(p_{m_s}\frac{d}{2})\frac{ah_{n_u}}{h_{m_s}^2-h_{n_u}^2}J_0(h_{n_u}a)J_1(h_{m_s}a) \tag{3.39}$$

$$-\int_{\phi=0}^{2\pi}\int_{\rho=0}^{a}\psi_{mu}\overline{\psi_{ns}}\,\rho d\rho d\phi = \frac{2\pi}{\omega^2\mu_0^2}U_m\overline{V_n}p_{m_u}\overline{p_{n_s}}\sin(\overline{p_{n_s}}\frac{d}{2})\cos(p_{m_u}L)\frac{ah_{m_u}}{h_{m_u}^2-h_{n_s}^2}J_0(h_{m_u}a)J_1(h_{n_s}a) \tag{3.40}$$

$$\int_{\phi=0}^{2\pi}\int_{\rho=0}^{a}\psi_{ms}\overline{\psi_{ns}}\,\rho d\rho d\phi = \begin{cases} \frac{\pi a^2}{\omega^2\mu_0^2}V_m\overline{V_m}p_{m_s}\overline{p_{m_s}}\sin(p_{m_s}\frac{d}{2})\sin(\overline{p_{m_s}}\frac{d}{2}) \\ \qquad \cdot\left[J_1^2(h_{m_s}a)-\frac{2}{h_{m_s}a}J_0(h_{m_s}a)J_1(h_{m_s}a)+J_0^2(h_{m_s}a)\right] \quad (m=n) \\ \frac{2\pi}{\omega^2\mu_0^2}V_m\overline{V_n}p_{m_s}\overline{p_{n_s}}\sin(p_{m_s}\frac{d}{2})\sin(\overline{p_{n_s}}\frac{d}{2})\frac{a}{h_{m_s}^2-h_{n_s}^2} \\ \qquad \cdot\left[h_{n_s}J_0(h_{n_s}a)J_1(h_{m_s}a)-h_{m_s}J_0(h_{m_s}a)J_1(h_{n_s}a)\right] \quad (m\neq n) \end{cases} \tag{3.41}$$

In order to match the boundary conditions on the transverse electric and magnetic fields on the boundary separating the upper cylindrical-cavity region from the sample region at $z = d/2$, we minimize the function J in (3.22). The functional J is minimized when the row vector $\mathbf{x}$ equals the eigenvector associated with the smallest eigenvalue of the Hermitian matrix $\mathbf{Z}$ [15]. Therefore, we compute the eigenvalue of $\mathbf{Z}$ as a function of k_s, until a minimum eigenvalue is found. From the computed eigenvectors at that minimum, we compute $\mathbf{x}$, the row vector containing the mode coefficients A_n and B_n.

Besides the values of mode coefficients, we also determine the value of k_s at the minimum. Since $k_s^2 = \omega^2\mu_0\epsilon_0\epsilon_s^{'}$ is a function of both the split-cylinder resonant frequency and the sample relative permittivity, we can use this resonance condition

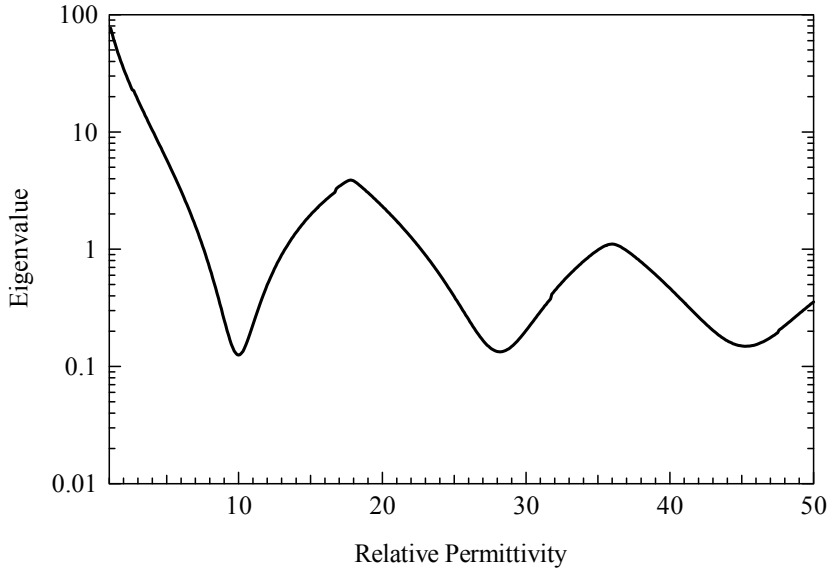

Figure 3.1: Smallest eigenvalue of $\mathbf{Z}$ as a function of the sample's relative permittivity $\epsilon_s^{'}$. In this example the sample's radius is 29.05 mm and the thickness is 1 mm. The length of the upper cylindrical-cavity region is 25.326 mm and the radius is 19.05 mm. The resonant frequency for the TE_{011} mode is 7.83 GHz.

in two ways. First, if the sample's relative permittivity is known, the value of k_s for the smallest eigenvalue is used to compute the split-cylinder's resonant frequency. Likewise, if the resonant frequency is known, we can compute the sample's relative permittivity

3.3 Relative Permittivity

After the resonant modes have been properly identified and the resonant frequency is measured, one can use the split-cylinder resonance condition to calculate the value of the sample's relative permittivity. We plot the smallest eigenvalue of $\mathbf{Z}$ as a function of $\epsilon_s^{'}$, as shown in Figure 3.1. The minima correspond to possible values for the relative permittivity of the sample. Thus, in order to determine the correct value of the sample's relative permittivity, one must provide some initial guess. With an initial guess, we can calculate the relative permittivity using an

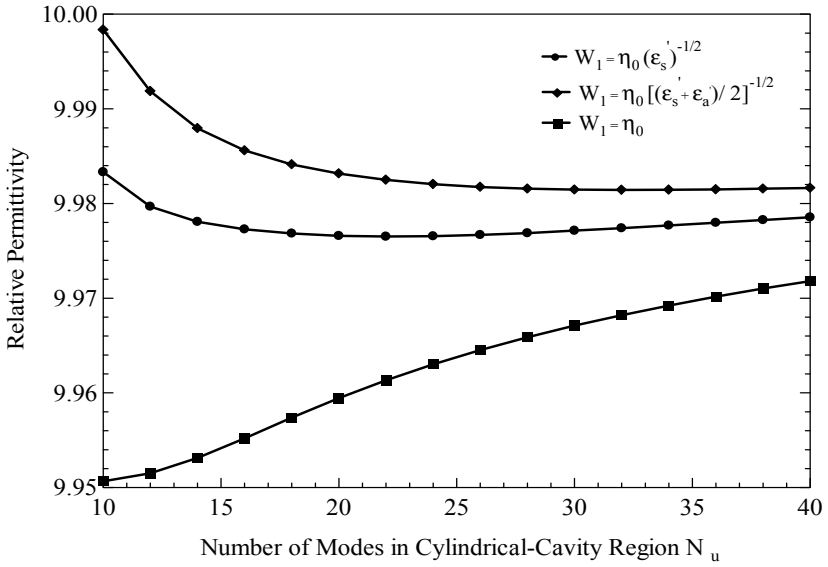

Figure 3.2: Relative permittivity of the sample as a function of the number of modes in the cylindrical-cavity region for various values of the weighting function W_1. In this example the sample's radius is 29.05 mm and the thickness is 1 mm. The length of the upper cylindrical-cavity region is 25.326 mm and the radius is 19.05 mm. The resonant frequency for the TE_{011} mode is 7.83 GHz.

iterative method, such as the Newton-Raphson method.

With the LSBR method, we specify the values of the weighting functions W_1 and W_2 in equation (3.21) so that numerical convergence is accelerated. We set W_2 equal to one so that the electric field boundary conditions in (3.21) would have the same weighting. As suggested by Jansen [16], the weighting function W_1 for the magnetic field boundary condition in (3.21) should be related to the wave impedance

$$W_1 = \frac{\eta_0}{\sqrt{\epsilon_r'}} = \sqrt{\frac{\mu_0}{\epsilon_0 \epsilon_r'}}. \tag{3.42}$$

However, since the split-cylinder resonator has two distinct regions with different material properties, we have several choices for the value of ϵ_r'. If we choose the wave impedance in the sample region then $\epsilon_r' = \epsilon_s'$. If we choose the wave impedance in the cylindrical-cavity region then $\epsilon_r' = \epsilon_a'$. Or we can choose the average of the relative permittivities of the two regions so that $\epsilon_r' = (\epsilon_s' + \epsilon_a')/2$. In

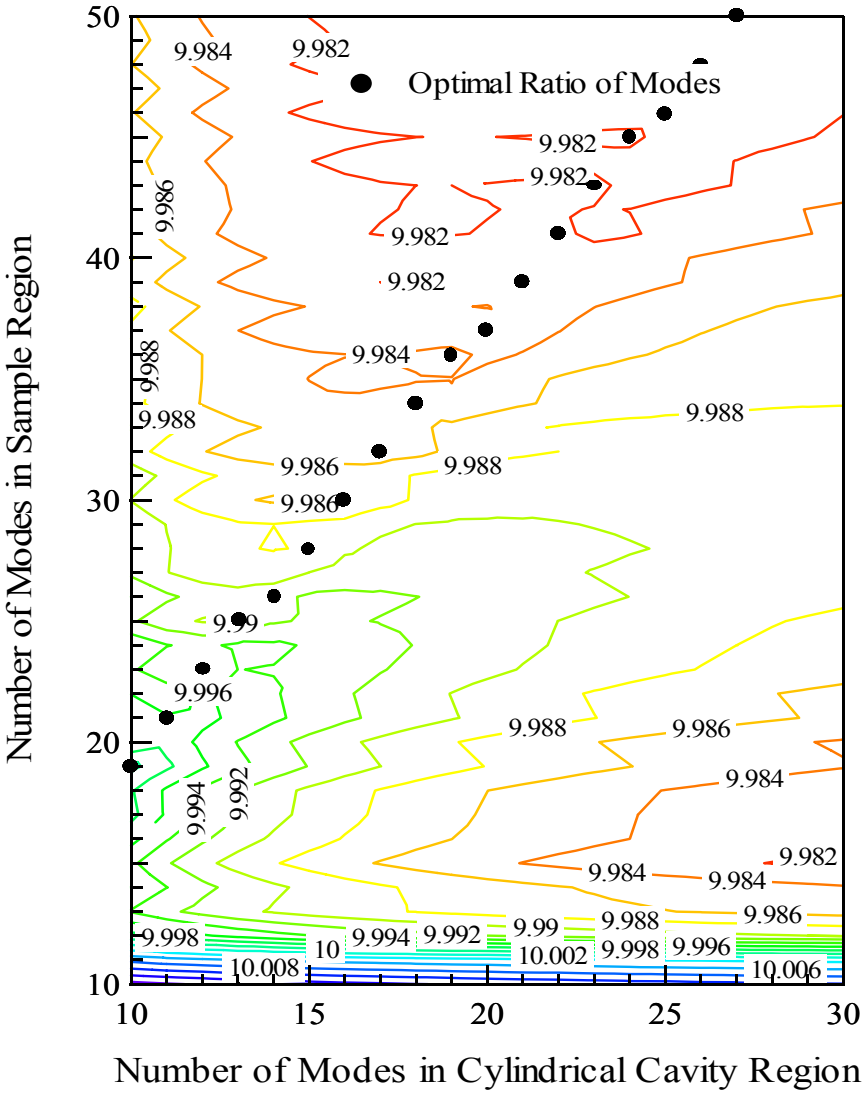

Figure 3.3: Relative permittivity as function of the number of modes in the cylindrical-cavity and sample regions.

Figure 3.2, we plot the value of the calculated relative permittivity as a function of the number of modes for the three values of W_1. As the number of modes increases, the values for the relative permittivity are in more agreement, although there remains a small discrepancy. Both convergence and stability seem to occur

when

$$W_1 = \sqrt{\frac{2\mu_0}{\epsilon_0(\epsilon_s' + \epsilon_a')}}, \tag{3.43}$$

so we selected this criterion as the weighting function for W_1.

With the mode-matching method, we truncate the number of modes in the cylindrical-cavity and sample regions. This truncation of modes leads to a systematic error, known as relative convergence error, in the calculation of the sample relative permittivity.

To examine the effect of relative convergence, we show in Figure 3.3 the calculated relative permittivity as a function of the number of modes in the cylindrical-cavity and sample regions. Section 2.3 outlines a criterion for selecting the ratio of modes that minimized the relative convergence error. We use this same criterion in the LSBR model and this value is shown in Figure 3.3. We see that the relative permittivity varies by several percent depending on the number of modes in each region. However, by carefully selecting the ratio of modes, the relative convergence is reduced, consistent with our findings with the mode-matching method.

After determining the mode ratio, we investigate how the value of relative permittivity varies as a function of the total number of modes. Thus, in Table 3.1, we list the calculated relative permittivity for an increasing number of modes in each region. For a small number of modes, the relative permittivity varies significantly, but rapidly converges as the number of modes increases. For $N_u = 30$ and $N_s = 46$, the variation in the relative permittivity is less than 5×10^{-4}.

In addition to examining the convergence as a function of the number of modes, we examine the effect of the sample radius b on the relative permittivity. As in the mode-matching method, the model based on the LSBR method assumes a conductive boundary at $\rho = b$ in the sample region, although no physical boundary

Number of Modes in Cylindrical-Cavity Region N_u	Number of Modes in Sample Region Region N_s	Sample Relative Permittivity $\epsilon_s^{'}$
4	8	10.0224
6	10	10.0195
8	13	10.0078
10	16	9.9983
12	19	9.9919
14	22	9.9879
16	25	9.9856
18	28	9.9841
20	31	9.9832
22	34	9.9825
24	37	9.9820
26	40	9.9817
28	43	9.9816
30	46	9.9815

Table 3.1: Relative permittivity as a function of modes in the cylindrical-cavity and sample regions where the ratio of modes is fixed.

exists. To ensure that the addition of this conductive boundary does not lead to a large systematic error we compute the relative permittivity as a function of b, as shown in Figure 3.4. For values of ρ several millimeters greater that the cylindrical-cavity radius a, the relative permittivity converges, although there remains a small oscillation for larger values of b. This is due to the fact that the electric field decays rapidly when $\rho > a$ in the sample region as shown in Figure 3.5.

3.4 Loss Tangent

In Section 3.3, the method for calculating the sample's relative permittivity uses the resonance condition derived with the LSBR method. The calculation of the relative permittivity requires the measured resonant frequency and the

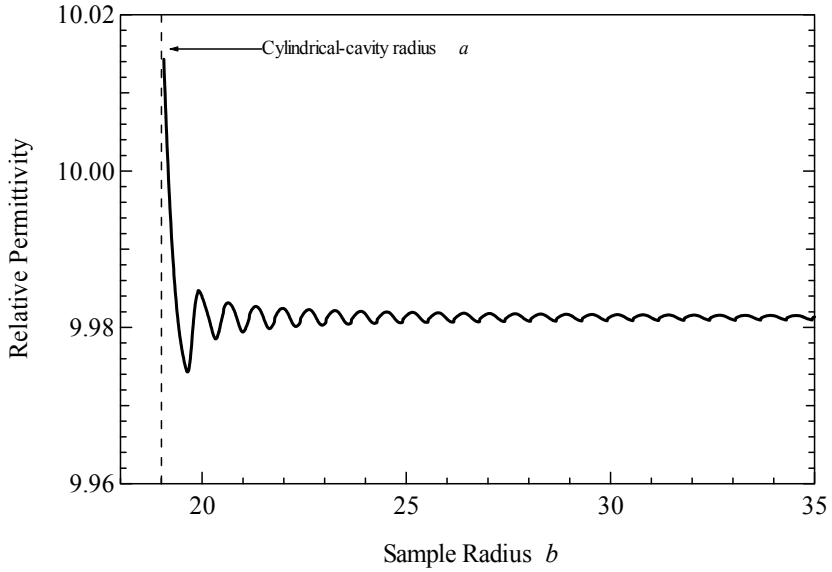

Figure 3.4: Relative permittivity as a function of sample radius b.

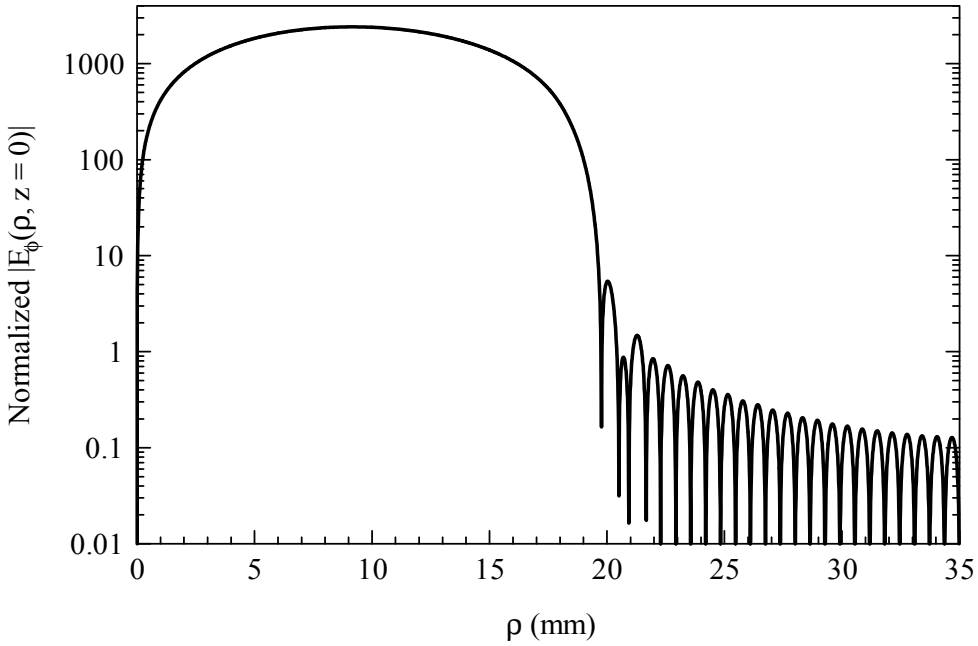

Figure 3.5: Normalized electric field in sample region as a function of ρ.

dimensions of both the split-cylinder resonator and the sample. With those values, and the addition of the resonant frequency quality factor Q, one can determine the sample loss tangent $\tan\delta$.

We define the quality factor Q as

$$Q = \frac{\omega(W_u + W_s)}{P_e + P_w + P_f + P_s}, \tag{3.44}$$

where W_u and W_s are the average energies stored in the cylindrical-cavity and sample regions respectively, and P_e, P_w, P_f, and P_s are the powers dissipated per second in the cylindrical cavity endplate, walls, flange, and sample respectively. When we calculate the sample permittivity by finding the smallest eigenvalue of $\mathbf{Z}$, we also we also determine the coefficients A_n and B_n from the eigenfunctions corresponding to the smallest eigenvalue. With these mode coefficients, we can calculate the electric and magnetic fields in the upper-cylindrical cavity region

$$E_{\phi_u}(\rho, z) = \sum_{n=1}^{N_u} A_n U_n J_1(h_{na}\rho) \sin[p_{na}(L + \frac{d}{2} - z)], \tag{3.45}$$

$$H_{\rho_u}(\rho, z) = -\frac{1}{j\omega\mu_0} \sum_{n=1}^{N_u} p_{n_u} A_n U_n J_1(h_{n_u}\rho) \cos[p_{n_u}(L + \frac{d}{2} - z)], \tag{3.46}$$

$$H_z(\rho, z) = -\frac{1}{j\omega\mu_0} \sum_{n=1}^{N_u} h_{n_u} A_n U_n J_0(h_{n_u}\rho) \sin[p_{n_u}(L + \frac{d}{2} - z)], \tag{3.47}$$

and the fields in the sample region

$$E_{\phi_s}(\rho, z) = \sum_{n=1}^{N_s} B_n V_n J_1(h_{n_s}\rho) \cos(p_{n_s} z), \tag{3.48}$$

$$H_{\rho_s}(\rho, z) = -\frac{1}{j\omega\mu_0} \sum_{n=1}^{N_s} p_{n_s} B_n V_n J_1(h_{n_s}\rho) \sin(p_{n_s} z), \tag{3.49}$$

$$H_{z_s}(\rho, z) = -\frac{1}{j\omega\mu_0} \sum_{n=1}^{N_s} h_{n_s} B_n V_n J_0(h_{n_s}\rho) \cos(p_{n_s} z). \tag{3.50}$$

We then define the stored-energy terms W_s and W_u as

$$W_s = \epsilon_0 \epsilon_s' \int_{z=0}^{\frac{d}{2}} \int_{\rho=0}^{b} \int_{\phi=0}^{2\pi} |E_{\phi_s}|^2 \rho \; d\phi \, d\rho \, dz \tag{3.51}$$

$$= \epsilon_0 \epsilon_s' \frac{\pi b^2}{4} \sum_{n=1}^{N_S} |B_n|^2 |V_n|^2 J_0^2(h_{n_s} b) \left[d + \frac{\sin(p_{n_s} d)}{p_{n_s}} \right]$$

and

$$W_u = \epsilon_0 \epsilon_a' \int_{z=\frac{d}{2}}^{L} \int_{\rho=0}^{a} \int_{\phi=0}^{2\pi} |E_{\phi_u}|^2 \rho \; d\phi \, d\rho \, dz \tag{3.52}$$

$$= \begin{cases} -\epsilon_0\epsilon_a^{'}\dfrac{\pi a^2}{4}\displaystyle\sum_{n=1}^{N_U}|A_n|^2|U_n|^2J_0^2(h_{n_u}a)\cdot \\ \qquad\qquad \left[d-2L-\dfrac{\sin(p_{n_u}d)}{p_{n_u}}+\dfrac{\sin(2p_{n_u}L)}{p_{n_u}}\right], \quad p_{n_u} \text{ is real} \\ \epsilon_0\epsilon_a^{'}\dfrac{\pi a^2}{4}\displaystyle\sum_{n=1}^{N_U}|A_n|^2|U_n|^2J_0^2(h_{n_u}a)\cdot \\ \qquad\qquad \left[d-2L-\dfrac{\sin(p_{n_u}d)}{p_{n_u}}+\dfrac{\sin(2p_{n_u}L)}{p_{n_u}}\right], \quad p_{n_u} \text{ is imaginary.} \end{cases}$$

In the same way, we can define the sources of power dissipation as

$$\begin{aligned} P_e &= R_s\int_{\rho=0}^{a}\int_{\phi=0}^{2\pi}|H_{\rho_u}|^2\rho\ d\phi\, d\rho\ \Big|_{z=L} \qquad (3.53)\\ &= R_s\frac{\pi a^2}{\omega^2\mu_0^2}\sum_{n=1}^{N_U}|A_n|^2|U_n|^2J_0^2(h_{n_u}a)\left|\cos(p_{n_u}\frac{d}{2})\right|^2 \end{aligned}$$

$$\begin{aligned} P_w &= R_s\int_{z=\frac{d}{2}}^{L}\int_{\phi=0}^{2\pi}|H_{z_u}|^2\rho\ d\phi\, dz\ \Big|_{\rho=a} \qquad (3.54)\\ &= \begin{cases} -R_s\dfrac{\pi a}{2\omega^2\mu_0^2}\displaystyle\sum_{n=1}^{N_U}|A_n|^2|U_n|^2h_{n_u}^2J_0^2(h_{n_u}a)\cdot \\ \qquad\qquad \left[d-2L-\dfrac{\sin(p_{n_u}d)}{p_{n_u}}+\dfrac{\sin(2p_{n_u}L)}{p_{n_u}}\right], \qquad p_{n_u} \text{ is real} \\ R_s\dfrac{\pi a}{2\omega^2\mu_0^2}\displaystyle\sum_{n=1}^{N_U}|A_n|^2|U_n|^2h_{n_u}^2J_0^2(h_{n_u}a)\cdot \\ \qquad\qquad \left[d-2L-\dfrac{\sin(p_{n_u}d)}{p_{n_u}}+\dfrac{\sin(2p_{n_u}L)}{p_{n_u}}\right], \qquad p_{na} \text{ is imaginary} \end{cases} \end{aligned}$$

$$\begin{aligned} P_f &= R_s\int_{\rho=a}^{b}\int_{\phi=0}^{2\pi}|H_{\rho_s}|^2\rho\ d\phi\, d\rho\ \Big|_{z=\frac{d}{2}} \qquad (3.55)\\ &= R_s\frac{\pi}{\omega^2\mu_0^2}\sum_{n=1}^{N_S}|B_n|^2|V_n|^2\Big\{b^2J_0^2(h_{n_s}b)-a^2[J_1(h_{na}a)-J_1(h_{n_s}a)]^2\Big\}\left|\sin(p_{n_s}\frac{d}{2})\right|^2 \end{aligned}$$

and

$$\begin{aligned} P_s &= \tan\delta\,\omega\epsilon_0\epsilon_s^{'}\int_{\rho=0}^{b}\int_{z=0}^{\frac{d}{2}}\int_{\phi=0}^{2\pi}|E_{\phi_s}|^2\rho\ d\phi\, d\rho\, dz \qquad (3.56)\\ &= \tan\delta\,\epsilon_0\epsilon_s^{'}\frac{\pi b^2\omega}{4}\sum_{n=1}^{N_S}|B_n|^2|V_n|^2J_0^2(h_{n_s}b)\left[d+\frac{\sin(p_{n_s}d)}{p_{n_s}}\right] \end{aligned}$$

Solving (2.79) in terms of the sample's loss tangent $\tan\delta$, we find

$$\tan\delta = \frac{\dfrac{\omega(W_s + W_a)}{Q} - P_e - P_w - P_f}{\epsilon_0 \epsilon_s^{'} \dfrac{\pi b^2 \omega}{4} \displaystyle\sum_{n=1}^{N_S} |B_n|^2 |V_n|^2 J_0^2(h_{n_s} b) \left[d + \dfrac{\sin(p_{n_s} d)}{p_{n_s}} \right]}. \tag{3.57}$$

Assuming that we have measured the resonant frequency and quality factor, calculated the sample's relative permittivity, and know the dimensions of the cylindrical-cavity and sample, the only remaining unknowns values in equation (3.57) are R_s, the surface resistivity of the cylindrical-cavity sections, and $\tan\delta$, the loss tangent of the sample. As outlined in Section 6.3.4, we obtain R_s from a measurement of the quality factor of the split-cylinder resonator when there is no sample and the gap between the two cylindrical-cavity sections is closed. Once we have the value for R_s, we can use equation (3.57) to explicitly calculate the sample's loss tangent.

As was the case with the calculation of the sample's relative permittivity, we must examine the convergence of the loss tangent. First, we consider the effect of relative convergence using the example as in Section 3.3. The sample's thickness is 1 mm, the radius is 29.05 mm and the relative permittivity is 10. The length of the upper cylindrical-cavity section is 25.326 mm, the radius is 19.05 mm, and the surface resistance of the metal is 0.026 Ω/m^2. The split-cylinder's TE_{011} resonant frequency is 7.83 GHz and the quality factor is 5000.

We calculate the loss tangent as a function of the number of modes in the cylindrical-cavity and sample regions and plot the results in Figure 3.6. Unlike the variation in the relative permittivity of several percent, the effect on the loss tangent variation is much smaller, less than one percent. Using the criterion in equation (2.78) to select the ratio of modes in each region, we can minimize this small error, due to relative convergence, on the loss tangent.

With the mode ratio, we examine the convergence of the loss tangent as a

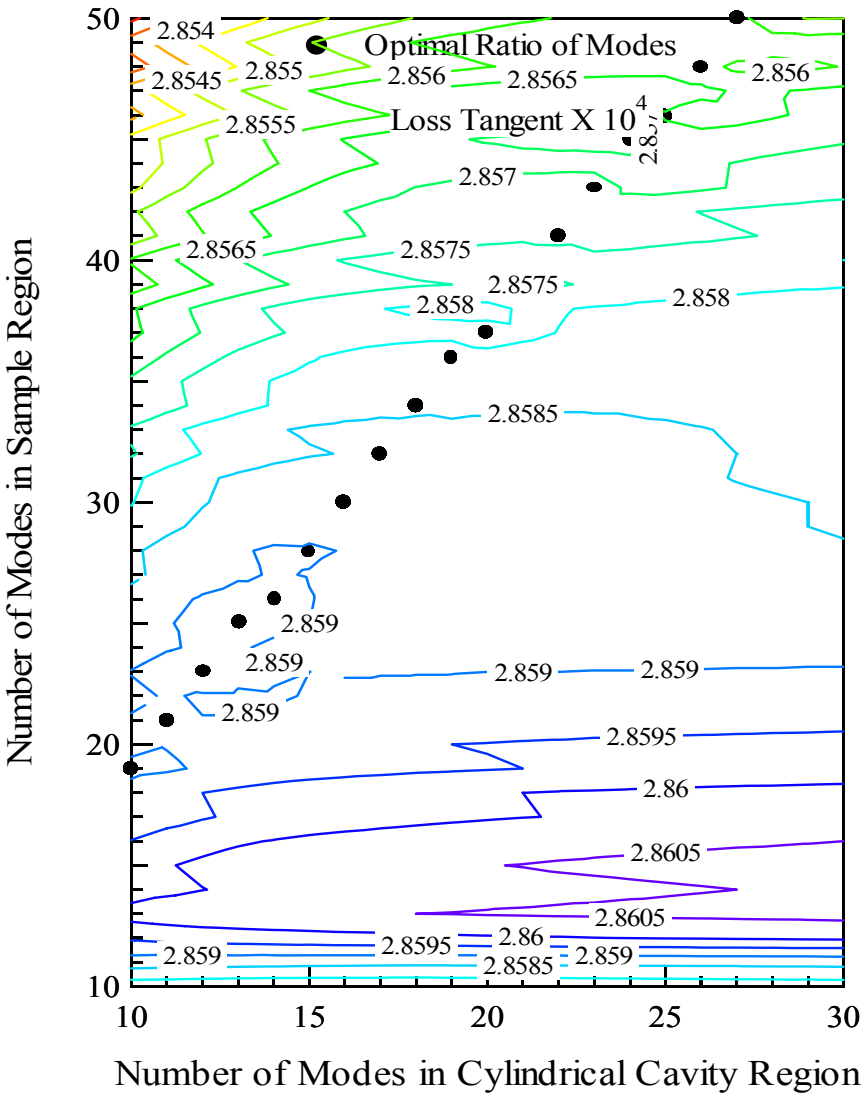

Figure 3.6: Loss tangent as a function of modes in the cylindrical-cavity and sample regions.

function of the total number of modes in each region. With the same values for the example shown in Figure 3.6, and fixing the mode ratio as determined by (2.78), we increase the number of modes in each region and examine the number of modes sufficient to reach numerical convergence. In Table 3.2, we list the calculated loss tangent as a function of the number of modes in the sample and cylindrical-cavity regions. The value of loss tangent converges quickly as we increase the number of

Number of Modes in Cylindrical-Cavity Region N_u	Number of Modes in Sample Region Region N_s	Sample Loss Tangent $\tan\delta \times 10^4$
4	8	2.921
6	10	2.921
8	13	2.923
10	16	2.923
12	19	2.924
14	22	2.924
16	25	2.923
18	28	2.923
20	31	2.923
22	34	2.923
24	37	2.922
26	40	2.922
28	43	2.922
30	46	2.911

Table 3.2: Loss tangent as a function of the number of modes in the cylindrical-cavity and sample regions where the ratio of modes is fixed.

modes, and we see changes less than 1×10^{-6} when $N_u = 30$ and $N_s = 46$.

Finally, we examine the effect of the conductive boundary at $\rho = b$ on the calculation of the loss tangent. In Figure 3.7 we plot the loss tangent as a function of b, the radius of the sample region. Unlike the relative permittivity, the loss tangent does not converge rapidly for values of b slightly larger than a, the radius of the cylindrical-cavity section. Instead, the loss tangent decreases for increasing values of b. This is due to the fact that the tangential magnetic field on the conductive flange $H_{\rho_s}(\rho, z = d/2)$ is slowly decaying for increasing ρ. Figure 3.8 shows that although the magnetic field decreases as a function of ρ, it is reduced by only one order of magnitude even when b is over a centimeter larger than a.

An important term in the calculation of the loss tangent is the power dissipated on the conductive flange. In equation (3.55) we show that the conductive

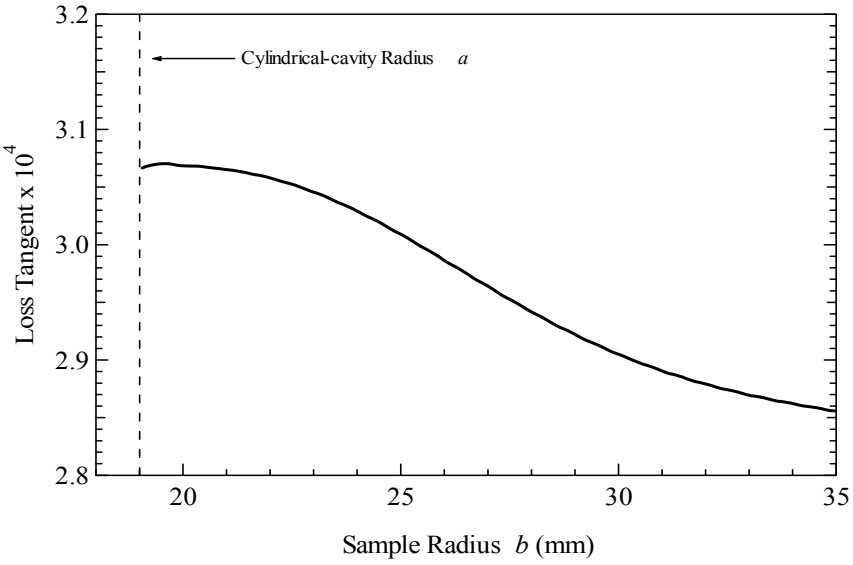

Figure 3.7: Loss tangent as a function of the radius of the sample region.

losses on the flange are related to the value of the tangential magnetic field H_{ρ_s}. As we increase the value of b, we include more conductive losses due to the flange, and the value of the loss tangent decreases. Although this variation in loss tangent is less than 2×10^{-5} in our example, we must include this systematic error in our uncertainty analysis as it might be a significant contribution to the uncertainty in the loss tangent for low-loss substrates.

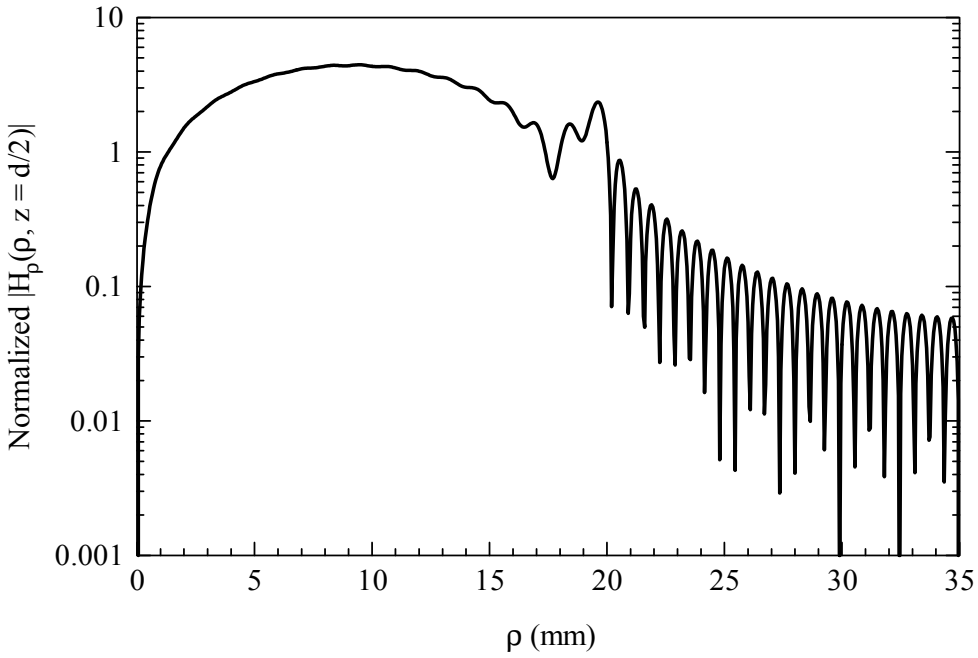

Figure 3.8: Normalized magnetic field along the conductive flange as a function of ρ.

Chapter 4

Hankel Transform Model

4.1 Introduction

In the previous two chapters we derived the resonance condition for the split-cylinder resonator using the mode-matching and the least-squares boundary residual (LSBR) methods. Both of these methods assume a perfectly conducting boundary at $\rho = b$, the diameter of the sample, in order to derive the resonance condition. This assumption leads to small systematic errors in the calculation of the sample's relative permittivity and loss tangent.

In this chapter, we summarize a method, the Hankel-transform method, for deriving the split-cylinder resonator resonance condition that does not include the conductive boundary at $\rho = b$ [17]. Instead, we assume that the sample extends to infinity in the radial direction as shown in Figure 4.1. Without a conducting boundary at the edge of the sample, the split-cylinder resonator is no longer a closed system. For this configuration, we employ Hankel transforms to derive expressions for the electric and magnetic fields in the various split-cylinder resonator regions and match these fields at the appropriate boundaries to derive a resonance condition. Knowledge of this resonance condition and the electric and magnetic fields leads to the calculation of the substrate's relative permittivity and loss tangent.

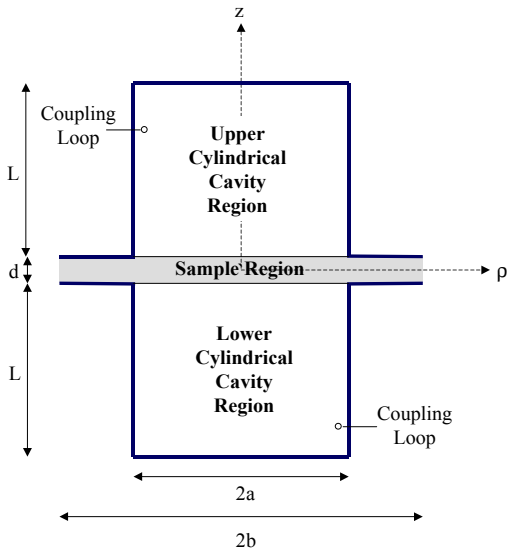

Figure 4.1: Cross-section of split-cylinder resonator with sample.

4.2 Split-Cylinder Theoretical Model

4.2.1 Fields in the Upper Cylindrical-Cavity Region

From the symmetry of the split-cylinder resonator and the assumption that we are exciting only TE_{onp} modes, the electric field in the upper cavity region has only a ϕ-component of the form

$$E_{\phi_u}(\rho, z) = \sum_{n=1}^{\infty} A_n R_{n_u}(\rho) Z_{n_u}(z), \tag{4.1}$$

where A_n is a constant, $R_{n_u}(\rho)$ is a radial eigenfunction and $Z_{n_u}(z)$ is a longitudinal function. Assuming that A_n is nonzero, we substitute (4.1) into the vector wave equation

$$\nabla^2 \vec{E} + \omega^2 \mu_0 \epsilon_0 \epsilon_a^{'} \vec{E} = 0, \tag{4.2}$$

to obtain

$$\frac{1}{R_n} \frac{1}{\rho} \frac{\partial}{\partial \rho} \left(\rho \frac{\partial R_n}{\partial \rho} \right) - \frac{1}{\rho^2} + k_u^2 = -\frac{1}{Z_{n_u}} \frac{\partial^2 Z_{n_u}}{\partial z^2} = k_n^2, \tag{4.3}$$

where $k_u^2 = \omega^2 \mu_0 \epsilon_0 \epsilon_a^{'}$, $\omega = 2\pi f$, k_n^2 is the separation constant, f is the frequency, and $\epsilon_a^{'}$ is the relative permittivity of the air within the upper cylindrical-cavity region. A time dependence of $\exp(j\omega t)$ is assumed. With the method of separation of variables to solve for $R_{n_u}(\rho)$ and $Z_{n_u}(z)$ in (4.3) we find

$$\begin{aligned} E_{\phi_u}(\rho, z) &= \sum_{n=1}^{\infty} A_n \left[C_n^{'} J_1(h_n \rho) + D_n^{'} Y_1(h_n \rho) \right] \cdot \\ &\quad \left[A_n^{'} \sin[k_n(L + \frac{d}{2} - z)] + B_n^{'} \cos[k_n(L + \frac{d}{2} - z)] \right], \end{aligned} \tag{4.4}$$

where $A_n^{'}$, $B_n^{'}$, $C_n^{'}$, and $D_n^{'}$ are constants, J_1 is the Bessel function of the first kind of order one, Y_1 is the Bessel function of the second kind of order one, and $h_n^2 = k_u^2 - k_n^2$.

From the boundary conditions on the transverse electric field

$$E_{\phi_u}\left(\rho, z = L + \frac{d}{2}\right) = 0, \quad 0 \le \rho \le a, \tag{4.5}$$

$$E_{\phi_u}(\rho = 0, z) \text{ is finite}, \quad 0 \le z \le L + \frac{d}{2}, \tag{4.6}$$

$$E_{\phi_u}(\rho = a, z) = 0, \quad \frac{d}{2} \le z \le L + \frac{d}{2}, \tag{4.7}$$

it follows that

$$B_n^{'} = 0, \tag{4.8}$$

$$D_n^{'} = 0, \tag{4.9}$$

$$h_n = \frac{j_{1,n}}{a}, \tag{4.10}$$

where $j_{1,n}$ is the nth zero of J_1. As a result, (4.4) reduces to

$$E_{\phi_u}(\rho, z) = \sum_{n=1}^{\infty} A_n R_n(\rho) \sin[k_n(L + \frac{d}{2} - z)], \tag{4.11}$$

where

$$R_{n_u}(\rho) = A_n^{'} C_n^{'} J_1(h_n \rho) = C_n J_1(h_n \rho). \tag{4.12}$$

To find an expression for C_n, we orthonormalize the radial eigenfunctions R_{n_u}. Substituting (4.12) into the orthonormalization condition

$$\int_0^a \rho R_{m_u}(\rho) R_{n_u}(\rho)\, d\rho = \delta_{mn}, \tag{4.13}$$

we find

$$C_n = \frac{\sqrt{2}}{aJ_0(h_n a)}, \tag{4.14}$$

where J_0 is the Bessel function of the first kind of order zero.

From the differential form of Faraday's law

$$\nabla \times \vec{E} = -j\omega\mu_0 \vec{H}, \tag{4.15}$$

and (4.11), we find the transverse component of the magnetic field

$$H_{\rho_u}(\rho, z) = -\frac{1}{j\omega\mu_0} \sum_{n=1}^{\infty} k_n A_n R_{n_u}(\rho) \cos[k_n(L + \frac{d}{2} - z)]. \tag{4.16}$$

To reduce the number of coordinates from two to one, we take the Hankel transforms of $E_{\phi_u}(\rho, z)$ and of $H_{\rho_u}(\rho, z)$ with respect to ρ. The Hankel transform of a function $f(\rho)$ is defined as

$$\tilde{f}(\zeta) = \int_0^{\infty} \rho' J_1(\zeta\rho') f(\rho')\, d\rho', \tag{4.17}$$

and the inverse Hankel transform is

$$f(\rho) = \int_0^{\infty} \zeta J_1(\zeta\rho) \tilde{f}(\zeta)\, d\zeta. \tag{4.18}$$

The Hankel transforms of (4.11) and (4.16) are

$$\tilde{E}_{\phi_u}(\zeta, z) = \sum_{n=1}^{\infty} A_n \tilde{R}_n(\zeta) \sin[k_n(L + \frac{d}{2} - z)] \tag{4.19}$$

and

$$\tilde{H}_{\rho_u}(\zeta, z) = -\frac{1}{j\omega\mu_0} \sum_{n=1}^{\infty} k_n A_n \tilde{R}_n(\zeta) \cos[k_n(L + \frac{d}{2} - z)], \tag{4.20}$$

where

$$\tilde{R}_n(\zeta) = \int_0^a \rho' J_1(\zeta\rho') R_n(\rho')\, d\rho'. \tag{4.21}$$

The exact integral of (4.21) is obtained by substituting (4.12) and (4.14) into (4.21):

$$\tilde{R}_n(\zeta) = \frac{\sqrt{2}}{\zeta^2 - h_n^2} h_n J_1(\zeta a). \tag{4.22}$$

4.2.2 Transverse Fields in the Sample Region

In our model, we assume that the sample is infinite in the radial direction, the magnetic and electric fields can exist anywhere along the sample, with a conductive flange above and below the sample ($z = \pm d/2$) in the region outside the cylindrical waveguide sections $\rho > a$. Therefore, any electric or magnetic fields outside the cylindrical waveguide regions must be confined to the sample.

In the sample region, as in the cavity regions, only TE_{0n} modes are considered. Therefore, the vector wave equation (4.2) is also satisfied in the sample region:

$$\left[\frac{1}{\rho}\frac{\partial}{\partial\rho}\left(\rho\frac{\partial}{\partial\rho}\right) + \frac{\partial^2}{\partial z^2} - \frac{1}{\rho^2} + \omega^2\mu_0\epsilon_0\epsilon_s'\right] E_{\phi_s}(\rho, z) = 0. \tag{4.23}$$

Taking the Hankel transform of (4.23) and integrating by parts twice we get

$$\tilde{E}_{\phi_s}(\zeta, z) = S(\zeta)\cos(k_s z) + T(\zeta)\sin(k_s z), \tag{4.24}$$

where $k_s^2 = \omega^2\mu_0\epsilon_0\epsilon_s' - \zeta^2$, ϵ_s' is the relative permittivity of the sample, and S and T are coefficients to be determined. The split-cylinder resonator symmetry requires that

$$\tilde{E}_{\phi_s}\left(\zeta, z = \frac{d}{2}\right) = \tilde{E}_{\phi_s}\left(\zeta, z = -\frac{d}{2}\right) \tag{4.25}$$

must hold for all $0 \leq \zeta \leq \infty$, and (4.24) simplifies to

$$\tilde{E}_{\phi_s}(\zeta, z) = S(\zeta)\cos(k_s z). \tag{4.26}$$

Again, using (4.15), we determine the transverse magnetic field

$$\tilde{H}_{\rho_s}(\zeta, z) = -\frac{k_s}{j\omega\mu_0} S(\zeta) \sin(k_s z). \tag{4.27}$$

4.2.3 Resonance Condition

In the previous two sections, we derived the Hankel-transformed transverse electric and magnetic fields in the upper cylindrical-cavity and sample regions. With the boundary conditions and orthogonality of the normal modes in the cylindrical-cavity region, the resonance condition for the split-cylinder resonator is determined.

The boundary condition that the electric field is continuous at $z = d/2$ requires that

$$\tilde{E}_{\phi_u}\left(\zeta, z = \frac{d}{2}\right) = \tilde{E}_{\phi_s}\left(\zeta, z = \frac{d}{2}\right) \quad 0 \leq \zeta \leq \infty. \tag{4.28}$$

Substituting the Hankel-transformed electric fields (4.26) and (4.19) into (4.28) we obtain

$$\sum_{n=1}^{\infty} A_n \tilde{R}_n(\zeta) \sin(k_n L) = S(\zeta) \cos\left(k_s \frac{d}{2}\right). \tag{4.29}$$

Solving for S we find

$$S(\zeta) = \frac{1}{\cos(k_s \frac{d}{2})} \sum_{n=1}^{\infty} A_n \tilde{R}_n(\zeta) \sin\left(k_n L\right). \tag{4.30}$$

The second boundary condition requires the continuity of the tangential magnetic field at the aperture between the upper cylindrical-cavity region and the sample region

$$\tilde{H}_{\rho_u}\left(\zeta, z = \frac{d}{2}\right) = \tilde{H}_{\rho_s}\left(\zeta, z = \frac{d}{2}\right) \quad 0 \leq \zeta \leq a. \tag{4.31}$$

Substituting the Hankel-transformed magnetic fields (4.27) and (4.20) into (4.31) we obtain

$$\sum_{n=1}^{\infty} k_n A_n \tilde{R}_n(\zeta) \cos(k_n L) = k_s S(\zeta) \sin\left(k_s \frac{d}{2}\right). \tag{4.32}$$

And the inverse Hankel transform of (4.32) with respect to ζ

$$\sum_{n=1}^{\infty} k_n A_n R_n(\rho)\cos(k_n L) = \int_0^{\infty} \zeta J_1(\zeta\rho) k_s S(\zeta)\sin(k_s\frac{d}{2})\, d\zeta. \tag{4.33}$$

To reduce the infinite summation in (4.33) to a single term, we make use of the orthonormalization of the normal modes in the cylindrical-cavity region

$$\int_0^a \rho R_{m_u}(\rho) R_{n_u}(\rho)\, d\rho = \delta_{mn}, \tag{4.34}$$

where δ_{mn} is the Kronecker delta function. Multiplying both sides of (4.33) by $\rho R_m(\rho)$ and integrating over the interval $[0, a]$ we obtain

$$k_m A_m \cos(k_m L) = \int_0^{\infty} \zeta \tilde{R}_m(\zeta) k_s S(\zeta)\sin\left(k_s\frac{d}{2}\right)\, d\zeta. \tag{4.35}$$

Substituting (4.30) into (4.35) we find the resonance condition

$$k_m A_m \cos(k_m L) = \sum_{n=1}^{\infty} A_n \sin(k_n L)\int_0^{\infty} \zeta \tilde{R}_m \tilde{R}_n(\zeta) k_s \tan\left(k_s\frac{d}{2}\right)\, d\zeta. \tag{4.36}$$

Again, we are faced with an infinite number of unknowns A_m in (4.35). To match the boundary condition exactly, all these terms must be included. However, in order to reduce this to a finite system of equations, we must truncate the number of modes N_u in the cylindrical-cavity region. We can express (4.35) in matrix form

$$\mathbf{Z}\vec{A} = 0, \tag{4.37}$$

where

$$Z_{mn} = -k_m \cos(k_m L)\delta_{mn} + \sin(k_n L)\int_0^{\infty} k_s \tan\left(k_s\frac{d}{2}\right)\, \zeta \tilde{R}_m \tilde{R}_n\, d\zeta, \tag{4.38}$$

and $\vec{A}$ is a column vector of the coefficients A_n. The linear system of equations (4.37) has a nontrivial solution only if

$$\det[\mathbf{Z}] = 0, \tag{4.39}$$

which is the resonance condition. As with the resonance conditions derived with the mode-matching and LSBR methods, we can use these equations to calculate either the resonant frequency of the split-cylinder resonator, given a known sample permittivity, or to calculate the sample's relative permittivity, given the measured split-cylinder resonant frequency.

4.3 Relative Permittivity

In the previous section, we used the Hankel transform method to derive the resonance condition for the split-cylinder resonator

$$\det[\mathbf{Z}] = 0, \tag{4.40}$$

where

$$Z_{mn} = -k_m \cos(k_m L)\delta_{mn} + \sin(k_n L) \int_0^\infty k_s \tan\left(k_s \frac{d}{2}\right) \zeta \tilde{R}_m \tilde{R}_n \, d\zeta. \tag{4.41}$$

Figure 4.2 is a plot of the determinant of $\mathbf{Z}$ as a function of the sample's relative permittivity. In this example we assume a sample thickness of 1 mm and a relative permittivity of 10. Each zero crossing in Figure 4.2 corresponds to a possible value for the sample permittivity. Thus, in order to solve for the sample's relative permittivity explicitly using (4.40), we must supply an initial guess for the relative permittivity that is reasonably close to the real value. This will prevent convergence to an incorrect zero.

Unlike the resonance conditions derived using the mode-matching and LSBR methods, there is no problem of relative convergence since we only specify the number of modes N_u in the cylindrical-cavity section. Also, we do not have to assume a perfectly conducting boundary at $\rho = b$ to derive the resonance condition. Unfortunately, this comes at the cost of having to numerically integrate (4.41) for every element of the $N_u \times N_u$ matrix $\mathbf{Z}$. Thus, we examine two aspects of numerical convergence.

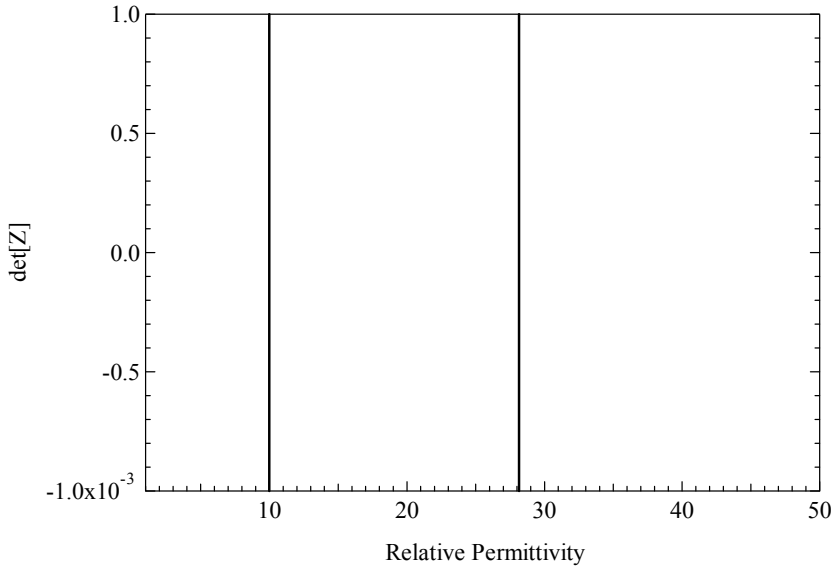

Figure 4.2: Determinant of $\mathbf{Z}$ as a function of resonant frequency. In this example, the sample's permittivity is 10, radius is 29.05 mm and thickness is 1 mm. The length of the upper cylindrical-cavity section is 25.326 mm and the radius is 19.05 mm.

First, in order to numerically integrate the matrix elements in (4.41), we truncate the upper bound of the integration limits to some finite value. To minimize the error resulting from the finite integration bound, we calculated the relative permittivity of several samples as a function of the upper integration bound and list these values in Table 4.1. We note that for all examples, the value of the relative permittivity converges at an upper integration bound of 100,000.

Besides the integration bound, we also examine the influence of the total number of modes N_u in the upper cylindrical-cavity region on the relative permittivity. Table 4.2 shows that the relative permittivity converges to a sufficient degree for various samples when the total number of modes in the upper cylindrical-cavity region reached ten.

	Sample Permittivity $\epsilon_{rs}^{'}$		
Resonant Frequency (GHz)	UB=10,000	50,000	100,000
10.02	1.0051	1.0054	1.0054
9.81	2.0077	2.0080	2.0080
9.06	4.9970	4.9973	4.9974
7.83	9.9936	9.9941	9.9941
6.21	20.0154	20.0162	20.1063
4.22	49.9283	49.9300	49.9301
3.05	100.2077	100.2110	100.2111

Table 4.1: Convergence study showing the calculated relative sample permittivity as a function of the upper bound of integration UB. In this study we fix the sample thickness at 1.0 mm and allow the resonant frequency to vary. The split-cylinder dimensions for this study are $L = 25.326$ mm and $a = 19.050$mm.

	Sample Permittivity $\epsilon_{rs}^{'}$				
Resonant Frequency (GHz)	NM=2	4	6	8	10
10.02	1.0059	1.0058	1.0057	1.0055	1.0054
9.81	2.0085	2.0084	2.0083	2.0081	2.0080
9.06	4.9979	4.9978	4.9977	4.9975	4.9973
7.83	9.9950	9.9948	9.9946	9.9943	9.9941
6.21	20.0176	20.0173	20.0170	20.0166	20.0162
4.22	49.9332	49.9325	49.9317	49.9309	49.9300
3.05	100.2171	100.2158	100.2142	100.2126	100.2110

Table 4.2: Convergence study showing the calculated relative sample permittivity as a function of the number of modes NM included in the Hankel transform model. In this study we fix the sample thickness at 1.0 mm and allow the resonant frequency to vary. The split-cylinder dimensions for this study are $L = 25.326$ mm and $a = 19.050$mm.

4.4 Loss Tangent

In the previous section, a method is given for calculating the sample's relative permittivity using a resonance condition derived from the Hankel transform method. This calculation requires the resonant frequency of the TE_{0np} mode and the dimensions of the sample and cylindrical-cavity regions. With the addition of the measured quality factor Q of the TE_{0np} resonance, the sample's loss tangent

may be calculated. The quality factor Q is defined as

$$Q = \frac{\omega(W_u + W_s)}{P_e + P_w + P_f + P_s} \tag{4.42}$$

where W_u and W_s are the average energies stored in the cylindrical-cavity and sample regions, and P_e, P_w, P_f and P_s are the powers dissipated per second in the cylindrical-cavity endplates, walls, flange, and sample respectively. When we calculated the sample's relative permittivity using (4.40), we also determined the mode coefficients A_n. Therefore, we can calculate the electric and magnetic fields in the upper cylindrical-cavity region

$$E_{\phi_u}(\rho, z) = \sum_{n=1}^{N_u} A_n \frac{\sqrt{2}}{aJ_0(h_n a)} J_1(h_n a) \sin[k_n(L + \frac{d}{2} - z)], \tag{4.43}$$

$$H_{\rho_u}(\rho, z) = -\frac{1}{j\omega\mu_0} \sum_{n=1}^{N_u} k_n A_n \frac{\sqrt{2}}{aJ_0(h_n a)} J_1(h_n a) \cos[k_n(L + \frac{d}{2} - z)], \tag{4.44}$$

$$H_{z_u}(\rho, z) = -\frac{1}{j\omega\mu_0} \sum_{n=1}^{N_u} h_n A_n \frac{\sqrt{2}}{aJ_0(h_n a)} J_0(h_n a) \sin[k_n(L + \frac{d}{2} - z)], \tag{4.45}$$

and the electric and magnetic fields in the sample region

$$E_{\phi_s}(\rho, z) = \sum_{n=1}^{N_s} A_n \sin(k_n L) \int_0^\infty \frac{\cos(k_s z)}{\cos(k_s \frac{d}{2})} \frac{\sqrt{2}}{\zeta^2 - h_n^2} h_n J_1(\zeta a) J_1(\zeta\rho) \zeta \, d\zeta, \tag{4.46}$$

$$H_{\rho_s}(\rho, z) = -\frac{1}{j\omega\mu_0} \sum_{n=1}^{N_s} A_n \sin(k_n L) \int_0^\infty k_s \frac{\sin(k_s z)}{\cos(k_s \frac{d}{2})} \frac{\sqrt{2}}{\zeta^2 - h_n^2} h_n J_1(\zeta a) J_1(\zeta\rho) \zeta \, d\zeta, \tag{4.47}$$

To obtain the fields in the sample region, the inverse Hankel-transform is required. As a result, unlike the modes in the upper cylindrical-cavity region, the fields in the sample region must be determined by numerical integration.

We define the stored-energy terms W_s and W_u as

$$\begin{aligned} W_s &= \epsilon_0 \epsilon_s' \int_{z=0}^{\frac{d}{2}} \int_{\rho=0}^{b} \int_{\phi=0}^{2\pi} |E_{\phi_s}|^2 \rho \; d\phi \, d\rho \, dz \qquad (4.48) \\ &= \frac{\pi \epsilon_0 \epsilon_s'}{4} \sum_{m=1}^{N_s} \sum_{n=1}^{N_s} A_m \overline{A_n} \sin(k_m L) \sin(\overline{k_n} L) \\ &\cdot \int_0^\infty \frac{\sqrt{2}}{\zeta^2 - h_m^2} \frac{\sqrt{2}}{\zeta^2 - h_n^2} h_m h_n J_1^2(\zeta a) \frac{1}{\cos(k_s \frac{d}{2})} \frac{1}{\cos(\overline{k_s} \frac{d}{2})} \left[d + \frac{\sin(k_s d)}{k_s} \right] \zeta \, d\zeta \end{aligned}$$

and

$$W_u = \epsilon_0\epsilon_a^{'} \int_{z=\frac{d}{2}}^{L}\int_{\rho=0}^{a}\int_{\phi=0}^{2\pi} |E_{\phi_u}|^2\rho \; d\phi \, d\rho \, dz \tag{4.49}$$

$$= \begin{cases} \frac{\pi\epsilon_0\epsilon_a^{'}}{4}\sum_{m=1}^{N_u}\sum_{m=1}^{N_u} A_m\overline{A_m}\left\{(2L-d)+\frac{1}{k_m}\left[\sin(k_m d)-\sin(2k_m L)\right]\right\} & k_m\text{is real} \\ -\frac{\pi\epsilon_0\epsilon_a^{'}}{4}\sum_{m=1}^{N_u}\sum_{m=1}^{N_u} A_m\overline{A_m}\left\{(2L-d)+\frac{1}{k_m}\left[\sin(k_m d)-\sin(2k_m L)\right]\right\} & k_m\text{is imag} \end{cases}$$

In the same way, we define the sources of power dissipation as

$$P_e = \frac{R_s}{2}\int_{\rho=0}^{a}\int_{\phi=0}^{2\pi} |H_{\rho_u}|^2\rho \; d\phi \, d\rho \; \Big|_{z=L} \tag{4.50}$$

$$= R_s\frac{\pi}{\omega^2\mu_0^2}\sum_{n=1}^{N_u} A_m\overline{A_m}k_m\overline{k_m}\cos(k_m\frac{d}{2})\cos(\overline{k_m}\frac{d}{2})$$

$$P_w = \frac{R_s}{2}\int_{\phi=0}^{2\pi}\int_{z=\frac{d}{2}}^{L} |H_{z_u}|^2\rho \; dz \, d\phi \; \Big|_{\rho=a} \tag{4.51}$$

$$= R_s\frac{2\pi}{a\omega^2\mu_0^2}\sum_{m=1}^{N_u}\sum_{n=1}^{N_u} A_m\overline{A_m}h_m h_n \int_{z=\frac{d}{2}}^{L} \sin[k_m(L+\frac{d}{2}-z)]\sin[\overline{k_n}(L+\frac{d}{2}-z)]\,dz$$

$$P_f = \frac{R_s}{2}\int_{\phi=0}^{2\pi}\int_{\rho=a}^{\infty} |H_{\rho_u}|^2\rho \;\; d\rho \, d\phi \; \Big|_{z=\frac{d}{2}} \tag{4.52}$$

$$= R_s\frac{\pi}{\omega^2\mu_0^2}\sum_{m=1}^{\infty}\sum_{n=1}^{\infty} A_m\overline{A_n}\sin(k_m L)\sin(\overline{k_n}L) \tag{4.53}$$

$$\cdot \int_{\rho=a}^{\infty}\left\{\left[\int_0^{\infty} k_s\tan(k_s\frac{d}{2})\frac{\sqrt{2}}{\zeta^2-h_m^2}h_m J_1(\zeta a)J_1(\zeta\rho)\zeta \;\; d\zeta\right]\right. \tag{4.54}$$

$$\left.\cdot \left[\int_0^{\infty}\overline{k_s}\tan(\overline{k_s}\frac{d}{2})\frac{\sqrt{2}}{\zeta^2-h_n^2}h_n J_1(\zeta a)J_1(\zeta\rho)\zeta \;\; d\zeta\right]\right\} \; d\rho \; \Big|_{z=\frac{d}{2}}$$

and

$$P_s = \tan\delta\,\omega\epsilon_0\epsilon_0^{'}\int_{\phi=0}^{2\pi}\int_{\rho=0}^{\infty}\int_{z=0}^{\frac{d}{2}} |E_{\phi_s}|^2\rho \;\; d\phi d\rho dz \tag{4.55}$$

$$= \tan\delta \frac{\pi\omega\epsilon_0\epsilon_s^{'}}{4} \sum_{m=1}^{N_u}\sum_{n=1}^{N_s} A_m\overline{A_n}\sin(k_mL)\sin(\overline{k_n}L) \tag{4.56}$$

$$\cdot \int_0^{\infty} \frac{\sqrt{2}}{\zeta^2-h_m^2}\frac{\sqrt{2}}{\zeta^2-h_n^2}h_mh_nJ_1^2(\zeta a)\frac{1}{\cos(k_s\frac{d}{2})}\frac{1}{\cos(\overline{k_s}\frac{d}{2})}\left[d+\frac{\sin(k_sd)}{k_s}\right]\zeta\ d\zeta.$$

Solving (4.42) in terms of the loss tangent $\tan\delta$, we find

$$\tan\delta = \frac{\frac{\omega(W_s+W_a)}{Q} - P_e - P_w - P_f}{T} \tag{4.57}$$

where

$$T = \frac{\pi\omega\epsilon_0\epsilon_s^{'}}{4} \sum_{m=1}^{N_u}\sum_{n=1}^{N_s} A_m\overline{A_n}\sin(k_mL)\sin(\overline{k_n}L) \tag{4.58}$$

$$\cdot \int_0^{\infty} \frac{\sqrt{2}}{\zeta^2-h_m^2}\frac{\sqrt{2}}{\zeta^2-h_n^2}h_mh_nJ_1^2(\zeta a)\frac{1}{\cos(k_s\frac{d}{2})}\frac{1}{\cos(\overline{k_s}\frac{d}{2})}\left[d+\frac{\sin(k_sd)}{k_s}\right]\zeta\ d\zeta.$$

Unfortunately, the term associated with the power dissipated on the conductive flange P_f posed a problem. The integrations necessary for the calculation of P_f are similar to those in P_s, the power dissipated in the sample. In the case of P_s, we were able to use

$$\frac{\delta(\zeta-\zeta^{'})}{\zeta} = \int_{\rho=0}^{\infty} \rho J_1(\zeta\rho)J_1(\zeta^{'}\rho)\ d\rho \tag{4.59}$$

to reduce the number of numerical integrations in (4.57) to one. However, for P_f, the integration in ρ is from a to b, not 0 to b as in the case of P_s. Therefore, we cannot use (4.59) to reduce the integrations in (4.55). Although we attempted to numerically integrate P_f, we were not successful. Therefore, we neglect this term in our calculation of the loss tangent. As a result, conductive losses on the conductive flange are added to the dielectric losses of the sample. Thus, the computed loss tangent is an upper bound on the loss tangent. This is a significant systematic error that we investigate further in Chapter 5, where we show it to be one of the main disadvantages of the Hankel-transform model.

Since we specify the number of modes only in the cylindrical-cavity region, we do not have to investigate any relative convergence error for the loss tangent.

	Loss Tangent $\tan\delta \times 10^{-4}$				
Resonant Frequency (GHz)	NM=2	4	6	8	10
10.02	41.692	41.678	41.668	41.660	41.653
9.81	17.854	17.845	17.839	17.833	17.828
9.06	5.691	5.687	5.683	5.680	5.677
7.83	3.066	3.063	3.060	3.058	3.056
6.21	2.246	2.243	2.240	2.238	2.236
4.22	1.879	1.876	1.874	1.872	1.870
3.05	1.739	1.749	1.743	1.741	1.739

Table 4.3: Convergence study showing the calculated loss tangent as a function of the number of modes NM included in the Hankel transform model. In this study we fix the sample thickness at 1.0 mm. Although the quality factor Q is fixed at 5000, the resonant frequency varies. The split-cylinder dimensions for this study are $L = 25.326$ mm and $a = 19.050$mm.

However, we examined the numerical convergence of the loss tangent as a function of the number of modes in the cylindrical-cavity section and show results in Table 4.3. Although we see good convergence with only a few number of modes, the computed value of the loss tangent in only an upper bound, since we've neglected the power dissipated on the split-cylinder flanges.

Chapter 5

Theoretical Model Comparison

5.1 Introduction

In the previous three chapters we employed the mode-matching, least-squares boundary residual (LSBR) and Hankel-transform methods to derive three theoretical models for the split-cylinder resonator. Each of these models allows one to calculate the relative permittivity and loss tangent of a dielectric substrate using a split-cylinder resonator. In this section, we compare the three different models using a variety of criteria, including the satisfaction of the boundary conditions, agreement in computed relative permittivity and loss tangent, and computational speed.

5.2 Boundary Conditions

In each of the three theoretical models, we derived a resonance condition for the split-cylinder resonator. An essential step in this derivation is the enforcement of the boundary conditions along the aperture separating the upper cylindrical-cavity region from the sample region at $z = d/2$, shown in Figure 5.1. As part of our comparison, the electric and magnetic fields at this boundary were calculated for all three theoretical models, and the performance of each method was examined in satisfying these boundary conditions.

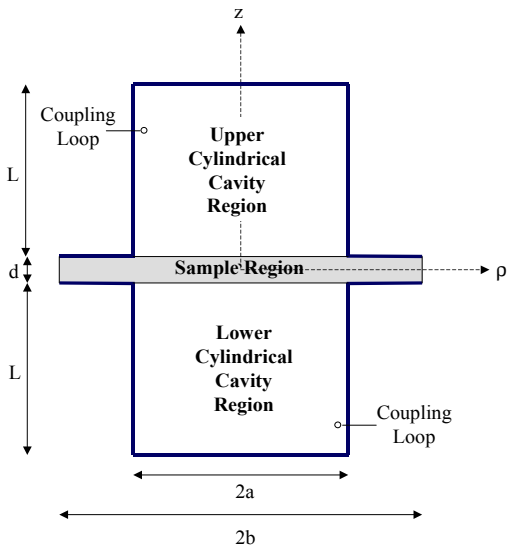

Figure 5.1: Cross-section of split-cylinder resonator with sample.

The first boundary condition required the continuity of the transverse electric field in the upper cylindrical-cavity region E_{ϕ_u} and the electric field in the sample region E_{ϕ_s} at $z = d/2$ over the range $0 \leq \rho \leq a$. In addition, the electric field in the sample region E_{ϕ_s} is zero at $z = d/2$ when $\rho > a$ since it is tangential to a flange assumed to be a perfect conductor. Figure 5.2 is a plot of the electric field on both sides of the boundary as a function of ρ for the three different models. In this example, we assume that the upper cylindrical-cavity radius a is 19.05 mm and the length L is 25.326 mm, sample thickness d is 1 mm and the relative permittivity $\epsilon_s^{'}$ is 10. In addition, the resonant frequency f of the TE_{011} mode is 7.83 GHz.

For all three models, the electric field is zero at $\rho = 0$, maximum at approximately $\rho = a/2$ and decreases as ρ approaches the radius of the upper cylindrical-cavity section at $\rho = a$. For values of ρ greater than a, the electric field in the sample region E_{ϕ_s} should vanish. However, as shown in Figure 5.2, the value in this region is non-zero, especially for cases of the mode-matching and LSBR

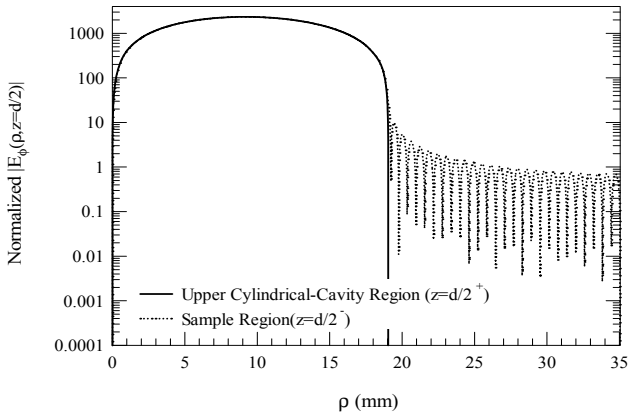

(a)

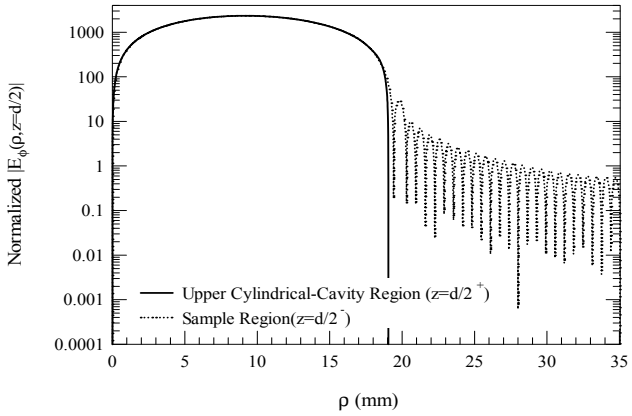

(b)

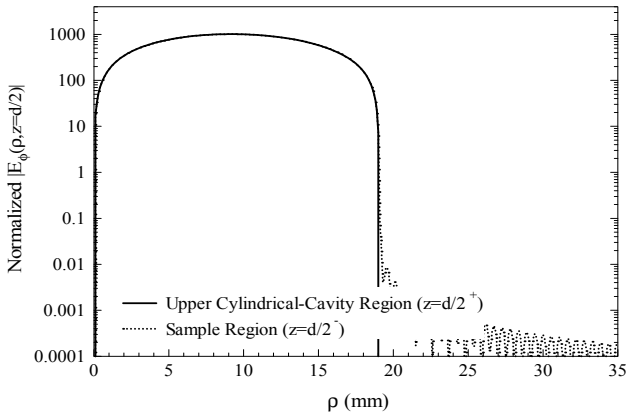

(c)

Figure 5.2: Comparison of the transverse electric fields at the boundary $z = d/2$ as a function of ρ for three theoretical models: (a) mode-matching, (b) LSBR, (c) Hankel-transform. Each cylindrical-cavity section's radius a is 19.05 mm and the length is 25.326 mm. The sample's thickness d is 1 mm and the relative permittivity is 10. The resonant frequency of the TE_{011} mode is 7.83 GHz.

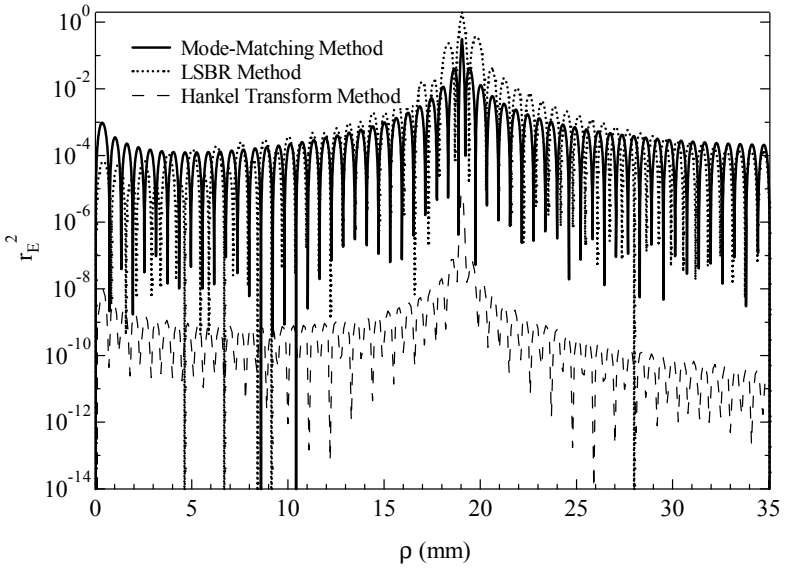

Figure 5.3: Comparison of the squared residuals r_E^2 for the electric fields at the boundary $z = d/2$ as a function of ρ for the three theoretical models. Each cylindrical-cavity section radius a is 19.05 mm and the length is 25.326 mm. The sample thickness d is 1 mm and the relative permittivity is 10. The resonant frequency of the TE_{011} mode is 7.83 GHz.

models. This is clearly shown in Figure 5.3, a plot of the squares of the residuals r_E^2 over the length of the boundary

$$r_E^2 = \begin{cases} \dfrac{|E_{\phi_u}(\rho, z = d/2^+) - E_{\phi_s}(\rho, z = d/2^-)|^2}{|E_{\phi_s}(\rho = a/2, z = d/2^-)|}, & 0 \le \rho \le a \\ \\ \dfrac{|0 - E_{\phi_s}(\rho, z = d/2^-)|^2}{|E_{\phi_s}(\rho = a/2, z = d/2^-)|}, & \rho > a. \end{cases} \tag{5.1}$$

If the boundary conditions on the transverse electric field are satisfied perfectly, the residual r_E should be zero. However, a finite value for the residuals reaches a maximum at $\rho = a$, the radius of the upper cylindrical-cavity section. This is not unexpected, as this is the location of a tranisition at the conductive corner between the cylindrical-cavity section and the conductive flange. Although this corner induces a singularity in the magnetic field, there is also some effect on the electric field. In the Hankel-transform method, unlike the mode-matching

and LSBR methods, an infinite number of TE_{0n} modes in the sample region is assumed. As a result, the Hankel-transform method is better able to represent the electric field at this corner, resulting in a smaller value for the residuals.

The second boundary condition requires the continuity of the magnetic field H_{ρ_u} in the upper cylindrical-cavity region and magnetic field H_{ρ_s} in the sample region at $z = d/2$ over the range $0 \leq \rho \leq a$. Unlike the electric field, the value of the magnetic field on the conductive flange is indeterminate for $\rho > a$, so no boundary condition of the magnetic field in the sample region can be specified. Figure 5.4 is a plot of $H_\rho \times \eta_0$ as a function of ρ at the boundary $z = d/2$, where the factor of the intrinsic wave impedance $\eta_0 = \sqrt{\mu_0/\epsilon_0}$ is included to obtain the same units as in the electric fields plotted in Figure 5.2.

Similar to the case of the electric field, the magnetic field is zero at $\rho = 0$, a maximum value at approximately $\rho = a/2$, then decreases until it reaches the conductive corner at $\rho = a$, that causes the singularity in the magnetic field. Comparison of the three models in Figure 5.4 shows that the fields match well in the center of the boundary, although there are some noticeable oscillations, not surprising since H_ρ is a derivative of the electric field E_ϕ. Closer to the edges of the boundary, significant mismatches of the magnetic field occur, especially at $\rho = a$, the location of the singularity. These differences are more apparent in Figure 5.5, a plot of the squared residuals r_H^2 of the magnetic field

$$r_H^2 = \frac{|H_{\rho_u}(\rho, z = d/2^+) - H_{\rho_s}(\rho, z = d/2^-)|^2}{|H_{\rho_s}(\rho = a/2, z = d/2^-)|}. \tag{5.2}$$

Although errors occur in the matching of the transverse electric and magnetic fields for all three theoretical models, their significance cannot be evaluated until the sample's relative permittivity and loss tangent are compared, a topic we address in the following sections.

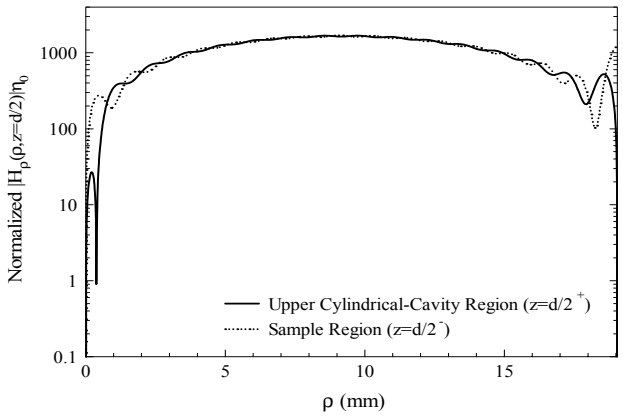

(a)

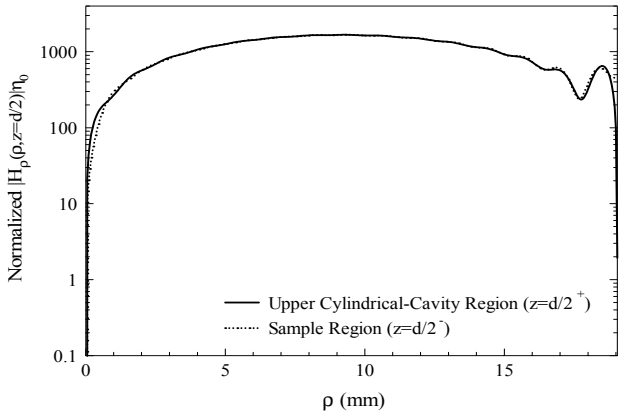

(b)

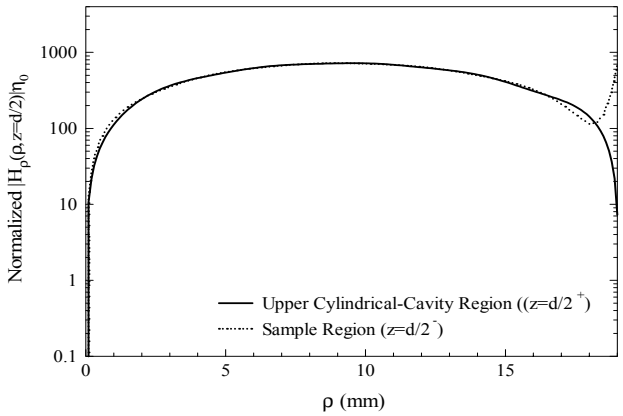

(c)

Figure 5.4: Comparison of the transverse magnetic fields at the boundary $z = d/2$ as a function of ρ for three theoretical models: (a) mode-matching, (b) LSBR, (c) Hankel-transform. Each cylindrical-cavity section radius a is 19.05 mm and the length is 25.326 mm. The sample thickness d is 1 mm and the relative permittivity is 10. The resonant frequency of the TE_{011} mode is 7.83 GHz.

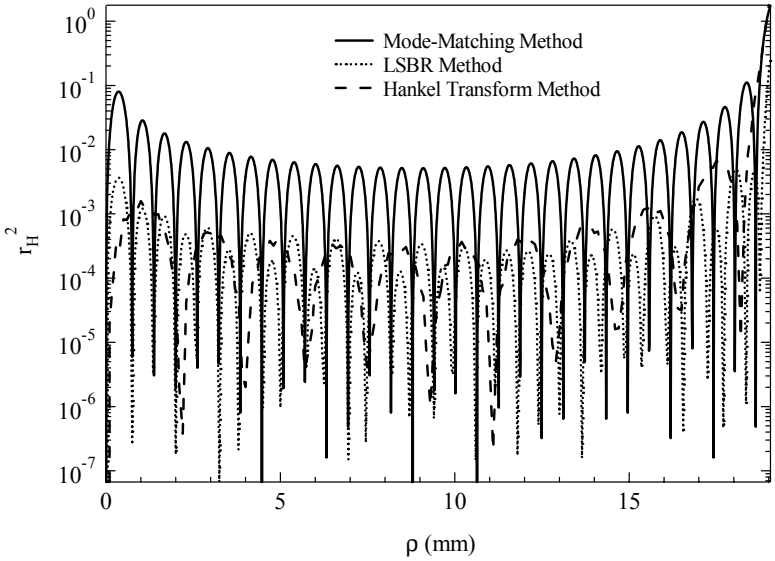

Figure 5.5: Comparison of the squared residuals r_H^2 for the magnetic fields at the boundary $z = d/2$ as a function of ρ for the three theoretical models. Each cylindrical-cavity section radius a is 19.05 mm and the length is 25.326 mm. The sample thickness d is 1 mm and the relative permittivity is 10. The resonant frequency of the TE_{011} mode is 7.83 GHz.

5.3 Relative Permittivity

In this section the three different theoretical models are used to compute the relative permittivity of several dielectric substrates of varying permittivites and thicknesses and observe the agreement between the models. For all of the comparisons given here, the dimensions are that the upper cylindrical-cavity section radius $a = 19.05$ mm and length $L = 25.326$ mm.

In our first comparison, we assume that all the dielectric substrates have a constant thickness $d = 1$ mm, but the resonant frequency of the TE_{011} mode varies from 3 to 10 GHz. Table 5.1 lists the computed relative permittivity for all three models. The results show agreement between the mode-matching and Hankel-transform models within 0.2 percent. When the LSBR method is included in the comparison, the agreement between all three models is within 1 percent.

Resonant Frequency (GHz)	Sample Permittivity $\epsilon_{rs}^{'}$ Mode-Matching	LSBR	Hankel
10.02	1.002	0.995	1.005
9.81	2.005	1.998	2.008
9.06	4.994	4.987	4.997
7.83	9.989	9.982	9.994
6.21	20.016	20.008	19.997
4.22	49.913	49.890	49.930
3.05	100.178	100.136	100.211

Table 5.1: Comparison of calculated relative permittivity $\epsilon_s^{'}$ where the sample thickness is constant (1 mm) and the TE_{011} resonant frequency varies (3-10 GHz). In this simulation, the upper cylindrical-cavity section radius is 19.05 mm and length is 25.326 mm.

The second comparison assumes that the resonant frequency of the TE_{011} mode is constant at 9.5 GHz, but that the substrate thickness d varies from 0.1 to 5 mm. Table 5.2 lists the computed relative permittivity for all three models. Again we see that the results of the mode-matching and Hankel-transform models agree within 0.2 percent and overall agreement between all three methods is within 1 percent.

Sample Thickness (mm)	Sample Permittivity $\epsilon_{rs}^{'}$ Mode-Matching	LSBR	Hankel
0.1	24.186	24.201	24.191
0.2	12.590	12.604	12.595
0.5	5.630	5.628	5.633
1.0	3.303	3.297	3.307
2.0	2.127	2.118	2.130
5.0	1.375	1.365	1.378

Table 5.2: Comparison of calculated relative permittivity $\epsilon_s^{'}$ where the TE_{011} resonant frequency is constant (9.5 GHz) and the sample thickness varies (0.1-5.0 mm). In this simulation, the upper cylindrical-cavity section radius is 19.05 mm and length is 25.326 mm.

Both of the comparisons show excellent agreement between the mode-matching and Hankel-transform methods for the relative permittivity, with some small dis-

crepancies for the LSBR method. This difference, as discussed in Section 3.3, is attributed to the fact that the relative permittivity, computed using the LSBR method, varies somewhat depending on the values of the arbitrary weighting functions W_1 and W_2 in equation (3.21).

Because the relative permittivity is solved iteratively in all three models, one must supply an initial guess that must be sufficiently close to the actual value of the relative permittivity in order to converge to the correct value. Tables 5.3 and 5.4 show the range of initial guesses that converge to the correct value of the relative permittivity for a variety of dielectric substrates. In Table 5.3, the sample thickness $d = 1$ mm is held constant while the TE_{011} resonant frequency is varied from 3 to 10 GHz. In Table 5.4, the TE_{011} resonant frequency (f =9.5 GHz) is held constant while the sample thickness is varied from 0.1 to 5.0 mm. In both simulations, we note that the Hankel-transform method has a much wider range of allowable initial guesses.

Resonant Frequency (GHz)	Computed Relative Permittivity $\epsilon_s^{'}$	Initial Guess Range for $\epsilon_{rs}^{'}$		
		Mode-Matching	LSBR	Hankel
10.02	1	(1-4)	(1-1.5)	(1-8.5)
9.81	2	(1-5)	(1-3)	(1-9.5)
9.06	5	(1-8.5)	(1-6.5)	(1-12.5)
7.83	10	(3.5-14.5)	(1-17.5)	(1-19)
6.21	20	(10.5-27)	(10.5-29.5)	(1-33)
4.22	50	(30-64.5)	(40-59.5)	(1-77)
3.05	100	(62-128)	(90.5-110)	(1-150.5)

Table 5.3: Comparison of valid initial guesses for relative permittivity $\epsilon_s^{'}$ where the sample thickness is constant (1 mm) and the TE_{011} resonant frequency varies (3-10 GHz). In this simulation, the upper cylindrical-cavity section radius is 19.05 mm and length is 25.326 mm.

Sample Thickness (mm)	Computed Relative Permittivity $\epsilon_s^{'}$	Initial Guess Range for $\epsilon_{rs}^{'}$ Mode-Matching	LSBR	Hankel
0.1	24.2	(9.5-37.5)	(14.5-34.0)	(1-91.5)
0.2	12.6	(2.5-21.5)	(3.0-22.5)	(1-46.5)
0.5	5.6	(1-10.5)	(1-7.5)	(1-19.5)
1.0	3.3	(1-6.5)	(1-4.5)	(1-10.5)
2.0	2.1	(1-4.0)	(1-3)	(1-6)
5.0	1.4	(1-2.5)	(1-1.5)	(1-3.5)

Table 5.4: Comparison of valid initial guesses relative permittivity $\epsilon_s^{'}$ where the TE_{011} resonant frequency is constant (9.5 GHz) and the sample thickness varies (0.1-5.0 mm). In this simulation, the upper cylindrical-cavity section radius is 19.05 mm and length is 25.326 mm.

5.4 Loss Tangent

In this section we compare the loss tangent of several dielectric substrates using the three different theoretical models. As in the previous relative permittivity comparison, we vary the permittivity and thicknesses of the dielectric substrates and observe the agreement between the models.

In the first comparison, we assume that the sample thickness $d = 1$ mm is constant for all the substrates, but the resonant frequency f of the TE_{011} mode varies from 3 to 10 GHz. In Table 5.5, we list the computed loss tangent using all three models. The results show less than 5×10^{-5} difference between the values. Note that as the loss tangent decreases, a slight discrepancy appears in the loss tangent computed using the Hankel-transform model. This is due to the fact, as discussed in Section 4.4, that we neglected the resistance metal losses P_f on the split-cylinder resonator's conductive flange. As a result, for low-loss materials, the loss tangent computed with the Hankel-transform method has a small systematic error resulting in a larger value of loss tangent than the values computed with the mode-matching or LSBR methods.

In the second comparison, the resonant frequency of the TE_{011} mode is held

Resonant Frequency (GHz)	Sample Loss Tangent $\tan\delta \times 10^{-4}$ Mode-Matching	LSBR	Hankel
10.02	41.79	42.14	41.65
9.81	17.85	17.91	17.83
9.06	5.61	5.62	5.68
7.83	2.92	2.92	3.06
6.21	2.02	2.03	2.24
4.22	1.56	1.56	1.87
3.05	1.35	1.35	1.74

Table 5.5: Comparison of calculated loss tangent $\tan\delta$ where the sample thickness is constant (1 mm) and the TE_{011} resonant frequency varies (3-10 GHz). In this simulation, the upper cylindrical-cavity section radius is 19.05 mm and length is 25.326 mm.

constant at 9.5 GHz, but the substrate thickness d varies from 0.1 to 5 mm. Table 5.6 lists the computed loss tangent for all three models. The agreement between all three models is within 0.2 $\times 10^{-5}$.

Sample Thickness (mm)	Sample Loss Tangent $\tan\delta \times 10^{-4}$ Mode-Matching	LSBR	Hankel
0.1	12.21	12.20	12.27
0.2	11.79	11.78	11.84
0.5	10.71	10.72	10.75
1.0	9.36	9.38	9.38
2.0	7.60	7.63	7.60
5.0	5.23	5.25	5.20

Table 5.6: Comparison of calculated loss tangent $\tan\delta$ where the TE_{011} resonant frequency is constant (9.5 GHz) and the sample thickness varies (0.1-5.0 mm). In this simulation, the upper cylindrical-cavity section radius is 19.05 mm and length is 25.326 mm.

5.5 Computation Speed

The the final comparison of the models, the overall computational speed was investigated. The computer used for these simulations was a Pentium-class PC using the Microsoft Windows 2000 operating system. First, we measured the amount of time to compute the relative permittivity in Table 5.1 and the

associated loss tangent in Tables 5.5, and show the results in Table 5.7. We note that the mode-matching model is nearly twenty times faster than the LSBR method and 100 times faster than the Hankel-transform method.

	Computational Speed (s)		
Resonant Frequency (GHz)	Mode-Matching	LSBR	Hankel
10.02	0.5	17.2	47.6
9.81	0.5	17.3	54.2
9.06	0.5	19.2	54.8
7.83	0.6	20.3	54.7
6.21	0.6	18.1	61.0
4.22	0.6	17.2	60.9
3.05	0.6	18.1	61.0

Table 5.7: Comparison of computational speed where the sample thickness is constant (1 mm) and the TE_{011} resonant frequency varies (3-10 GHz). In this simulation, the upper cylindrical-cavity section radius is 19.05 mm and length is 25.326 mm.

In our second simulation, we measured the amount of time to compute the relative permittivity in Table 5.2 and the associated loss tangent in Table 5.6, and show these results in Table 5.8. Again, we note that the mode-matching model is superior to the other two models in terms of computational speed. The LSBR method is slower because each iterative step in the calculation of the relative permittivity involves calculating the eigenvalue of a large complex matrix. The poor performance of the Hankel-transform method is attributed to the many numerical integrations that are required to calculate both the relative permittivity and loss tangent.

5.6 Model Selection

Based on our comparison of the three theoretical models, we chose to implement the mode-matching model in our measurement software. First, it accurately computes both the relative permittivity and loss tangent for a wide range

Sample Thickness (mm)	Computational Speed (s)		
	Mode-Matching	LSBR	Hankel
0.1	0.6	20.1	59.2
0.2	0.5	19.9	56.5
0.5	0.5	19.2	55.5
1.0	0.5	20.4	54.9
2.0	0.5	19.2	54.6
5.0	0.5	18.4	48.5

Table 5.8: Comparison of computational speed where the TE_{011} resonant frequency is constant (9.5 GHz) and the sample thickness varies (0.1-5.0 mm). In this simulation, the upper cylindrical-cavity section radius is 19.05 mm and length is 25.326 mm.

of dielectric substrates. In contrast, the LSBR method results are poor for the relative permittivity because of the arbitrary weighting functions W_1 and W_2, and the Hankel-transform method results are poor for the loss tangent because it neglected the resistive metal losses P_f in the split-cylinder resonator's flange. Secondly, in terms of computational speed, the mode-matching method is superior since it doesn't require time-consuming operations such as numerical integrations or computation of complex eigenvalues. Because the mode-matching method performs well both in terms of accuracy and speed we used it exclusively to calculate the relative permittivity and loss tangent in the remaining chapters of the thesis.

Chapter 6

Relative Permittivity and Loss Tangent Measurements

6.1 Introduction

In this chapter we develop the metrology necessary for relative permittivity and loss tangent measurements with a split-cylinder resonator. First, we review the mechanical specifications for both the split-cylinder resonator and the dielectric substrate. Second, we outline the process we adopted to characterize the intermediate measurement variables required for calculating the relative permittivity and loss tangent. Next, we describe the step-by-step measurement procedure we employed. Relative permittivity and loss tangent measurement results are presented for several substrates and compared with measurements made with other techniques. Included in this discussion are the development of uncertainty budgets for both the relative permittivity and loss tangent in addition to results of a repeatability study that verify the stability of the split-cylinder resonator.

6.2 Mechanical Specifications

6.2.1 Split-Cylinder Resonator Specifications

This section describes the design and construction of the split-cylinder resonator, shown in Figure 6.1. Detailed drawings of this particular split-cylinder resonator are given in Appendix A. The split-cylinder resonator is simply a circular-cylindrical cavity that is split into two halves – an upper and a lower section.

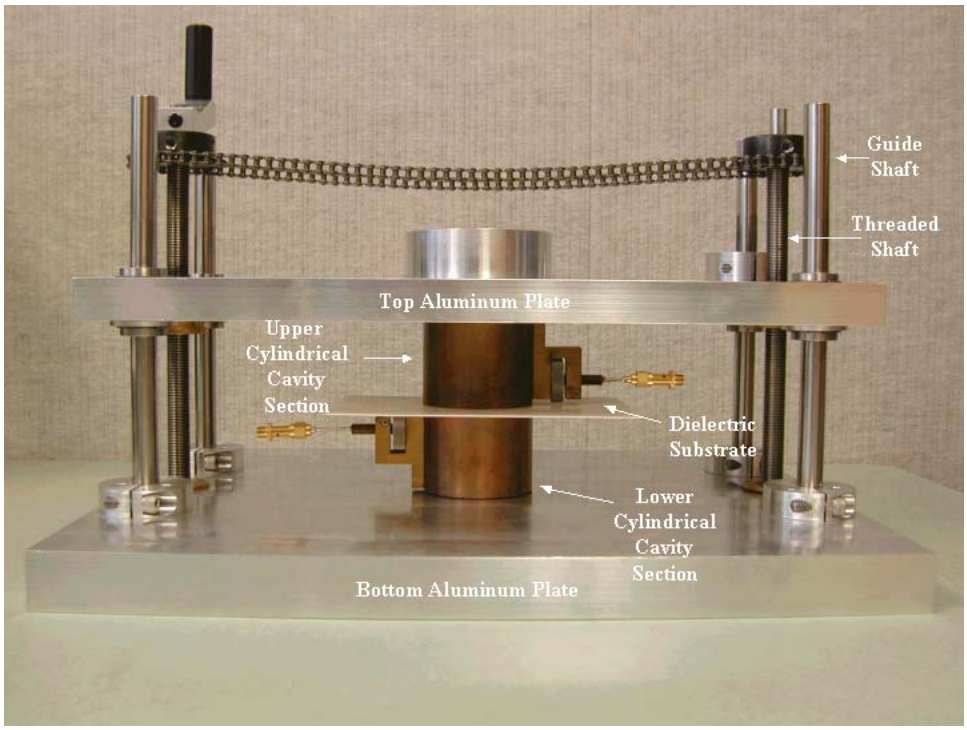

Figure 6.1: Split-cylinder resonator.

By selecting the dimensions of these sections, one can design the split-cylinder resonator to operate over a specific frequency range. For measurements in the vicinity of 10 GHz, we specified a diameter of 38.1 mm and a length of 25.4 mm for each of the cylindrical-cavity sections. With these dimensions, the resonant frequency of the TE_{011} mode was approximately 10 GHz with no sample and no gap between the two cylindrical-cavity sections.

Another design criterion was to maximize the quality factor of the split-cylinder resonator. The larger the quality factor, the greater the sensitivity one has in the measurement of the loss tangent of low-loss materials. Therefore, we fabricated the two cylindrical-cavity sections from oxygen-free copper, a good conductor with a conductivity of approximately 5.8×10^7 S/m. Figure 6.2 shows a top and side view of the lower cylindrical-cavity section. By using a high-

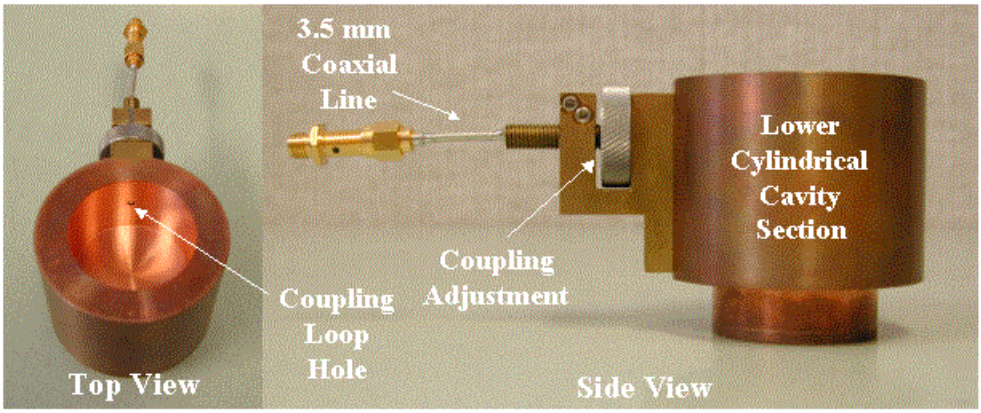

Figure 6.2: Lower cylindrical-cavity section.

conductivity metal, the resistive metal losses of the cylindrical-cavity sections are reduced and the quality factor of the split-cylinder resonator increased.

The quality factor may also be increased by the use of variable coupling loops in the cylindrical-cavity sections. These coupling loops, one in each of the cylindrical-cavity sections, excite the TE_{0np} resonances in the split-cylinder resonator. They introduce resistive losses that lower the quality factor of the split-cylinder resonator. To minimize these losses, we designed the coupling loops with adjustable penetration distance into the split-cylinder resonator for minimal coupling. With oxygen-free copper for resonator construction and minimal coupling, a quality factor of over 22,000 for the TE_{011} resonant mode at 10 GHz was obtained with no sample and no gap between the two cylindrical-cavity sections.

Next, our design required maximum alignment of the two cylindrical-cavity sections, even when the two sections are separated by the dielectric substrate thickness. Any misalignment could lead to systematic errors in both the relative permittivity and loss tangent. Therefore, as shown in Figure 6.1, we mounted the lower cylindrical-cavity section on a base plate. The upper cylindrical-cavity section was mounted on a plate suspended above the lower cylindrical-cavity section by two threaded shafts. The two threaded shafts are connected by a gear

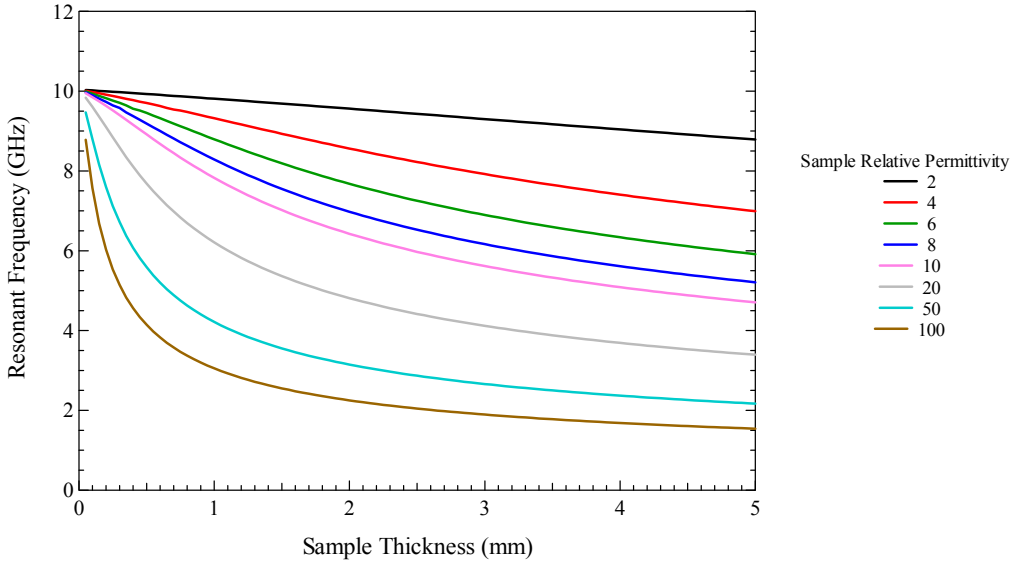

Figure 6.3: Resonant frequency of the TE_{011} resonant mode as a function of the sample's relative permittivity and thickness.

and chain assembly. By rotating the gear on one of the threaded shafts, the top aluminum plate moves vertically, thereby changing the distance d between the two cylindrical-cavity sections. To maintain the alignment of the two cylindrical-cavity sections, the top aluminum plate is guided by four stainless steel shafts, with precision ball bearings in contact with the aluminum plate and the stainless steel guide shafts.

6.2.2 Dielectric Substrate Specifications

The resonant frequency of the split-cylinder resonator varies considerably as a function of the sample's relative permittivity and thickness. Figure 6.3 is a plot of the resonant frequency of the TE_{011} resonant mode as a function of sample thickness and relative permittivity for the split-cylinder resonator described in Section 6.2.1. The resonant frequency of the TE_{0np} mode is inversely proportional to both the sample thickness and relative permittivity and varies from 2 GHz for a thick, high-permittivity material to 10 GHz for a thin, low-permittivity material.

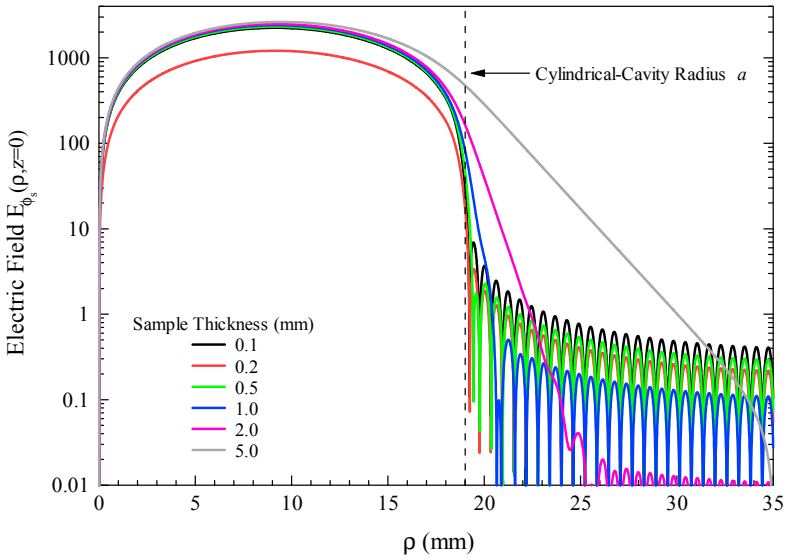

Figure 6.4: Electric field E_{ϕ_s} as a function of sample thickness. The dielectric substrate relative permittivity is 10 and the resonant frequency of the TE_{011} mode is 9.5 GHz.

The advantage of this frequency dependence is that, with an approximate value for the substrate's relative permittivity, one may select a thickness so that a measurement is made at a particular frequency.

However, one must be careful not to specify a sample thickness that is too large. First, as the sample thickness increases, more power is dissipated in the sample, resulting in lower quality factors for the TE_{0np} modes. If the quality factors become too low, the TE_{0np} mode can interfere with an adjacent resonant mode, resulting in systematic errors. In addition, as shown in Figure 6.4, the electric field E_{ϕ_s} fringes further into the sample region as the sample's thickness increases. In this example, the relative permittivity is 10 and the TE_{011} resonant frequency is 9.5 GHz. By varying the sample thickness from 0.1 mm to 5 mm, significant fringing fields appear for substrates with thicknesses on the order of 1 mm and above. These fringing fields are not desirable because their interaction with the conductive flange decreases the quality factor.

Another reason to minimize the fringing fields is that the electric field E_{ϕ_s} may not adequately decay before reaching the edge of the sample at $\rho = b$, thereby resulting in a systematic error. Therefore, after selecting a thickness, one must ensure that the sample diameter not only covers the entire cross-section of the cylindrical-cavity sections, but must extend further until the electric field has decayed significantly. For samples less than 1 mm, the sample diameter may only have to be several millimeters more than the cylindrical-cavity sections, but for samples greater than 1 mm, the sample diameter may be significantly larger.

Besides the sample thickness and diameter, the flatness of the sample must be considered. All of the theoretical models we derived for the split-cylinder resonator assume a perfectly flat sample with a uniform constant d. Unfortunately, most samples have some variability due to the manufacturing process. As we have not taken this into account in any of the models, uncertainty in the sample thickness should be minimized as much as possible. In our case, we tried to limit the thickness uncertainty to less than 0.02 mm. In some cases, it may be necessary to machine the samples to the proper specifications.

6.3 Characterization of Measurement Variables

In order to calculate the relative permittivity and loss tangent of a dielectric substrate, we must first accurately characterize several intermediate variables. These include the resonant frequency f and quality factor Q of the TE_{0np} resonant mode; the radius a, length L, and conductivity σ of the cylindrical-cavity sections; and the thickness d of the sample. In this chapter we discuss the method for characterizing each variable, including an uncertainty budget for each.

6.3.1 Resonant Frequency and Quality Factor

First, we summarize the technique for accurately measuring the resonant frequency and quality factor or the TE_{0np} resonant mode. Figure 6.5 shows a plot of a TE_{011} resonance curve for the split-cylinder resonator, measured with an automatic network analyzer. Commonly, the peak of the resonance curve is assumed to be the resonant frequency and the 3-dB method is used to calculate the quality factor. In this model, the quality factor is the peak frequency divided by the 3-dB bandwidth, where the 3-dB bandwidth is the difference between the half power points on either side of the resonant frequency [18]. Thus, with only three points on the resonance curve, one can calculate the resonant frequency and quality factor with the 3-dB method. However, as seen in Figure 6.5, the resonance curve contains some noise, especially as the coupling levels decrease. Therefore, the 3-dB method is susceptible to errors when the signal-to-noise ratio decreases.

To reduce the measurement uncertainties for the resonant frequency and quality factor, we adopted the weighted nonlinear least-squares method described in [19]. First, we model the two-port split-cylinder resonator with the equivalent circuit shown in Figure 6.6 [20, 21]. We employ two ideal transformers to model the two coupling loops that excite the split-cylinder resonator, and a series inductor L, capacitor C, and resistor R to model the split-cylinder resonator. The resistances and self-inductances of the coupling loops are assumed to be negligible [21]. An impedance-matched source is connected to port one of the cavity while an impedance-matched load is connected to port two. Note that the source and load can be interchanged without loss of generality.

We define $T(f)$ as the transmission loss through the cylindrical cavity

$$T(f) = \frac{P_{in}}{P_L}, \tag{6.1}$$

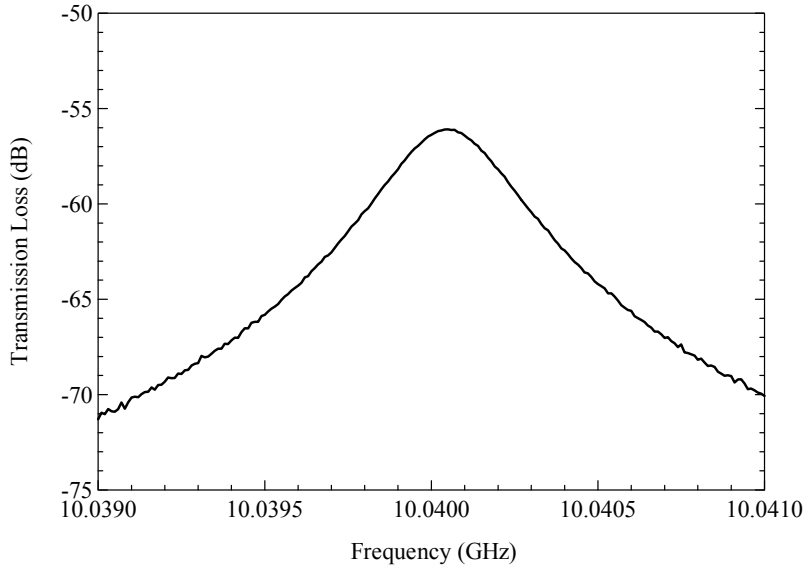

Figure 6.5: Resonance curve for a TE_{011} mode.

where f is the frequency, P_{in} is the maximum power delivered to a matched load connected at port one, and P_L is the maximum power delivered to the load at port two [21]. Solving for P_{in} and P_L we find

$$P_{in} = I_1 I_1^* Z_0 = \frac{V_s^2}{4Z_0} \tag{6.2}$$

and

$$P_L = I_2 I_2^* Z_0 = \frac{V_s^2}{Z_0} \frac{\beta_1 \beta_2}{(1+\beta_1+\beta_2)^2 + Q_0^2(\frac{f}{f_0} - \frac{f_0}{f})^2}, \tag{6.3}$$

where the coupling coefficient for port one β_1 is

$$\beta_1 = \frac{n_1^2 Z_0}{R} \tag{6.4}$$

and the coupling coefficient for port two β_2 is

$$\beta_2 = \frac{n_2^2 Z_0}{R}. \tag{6.5}$$

In (6.3), the resonant frequency f_0 is defined as

$$f_0^2 = \frac{1}{4\pi^2 LC}, \tag{6.6}$$

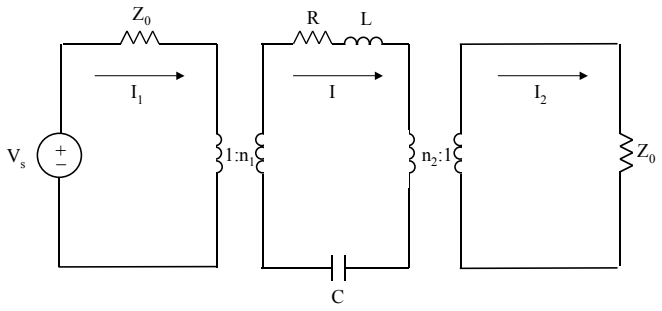

Figure 6.6: Split-cylinder resonator equivalent circuit model.

and the unloaded quality factor Q_0 is

$$Q_0 = \frac{2\pi f_0 L}{R}. \tag{6.7}$$

Substituting (6.2) and (6.3) into (6.1) we obtain

$$T(f) = \frac{4\beta_1\beta_2}{(1+\beta_1+\beta_2)^2 + Q_0^2(\frac{f}{f_0} - \frac{f_0}{f})^2}. \tag{6.8}$$

At resonance ($f = f_0$), the transmission loss reduces to

$$T(f_0) = \frac{4\beta_1\beta_2}{(1+\beta_1+\beta_2)^2}. \tag{6.9}$$

Taking the ratio of $T(f_0)/T(f)$ we get

$$\frac{T(f_0)}{T(f)} = 1 + \frac{Q_0^2(\frac{f}{f_0} - \frac{f_0}{f})^2}{(1+\beta_1+\beta_2)^2}. \tag{6.10}$$

Note that in practice, the unloaded quality factor Q_0 is larger than the measured quality factor Q due to the effects of the coupling loops

$$Q_0 = Q(1+\beta_1+\beta_2). \tag{6.11}$$

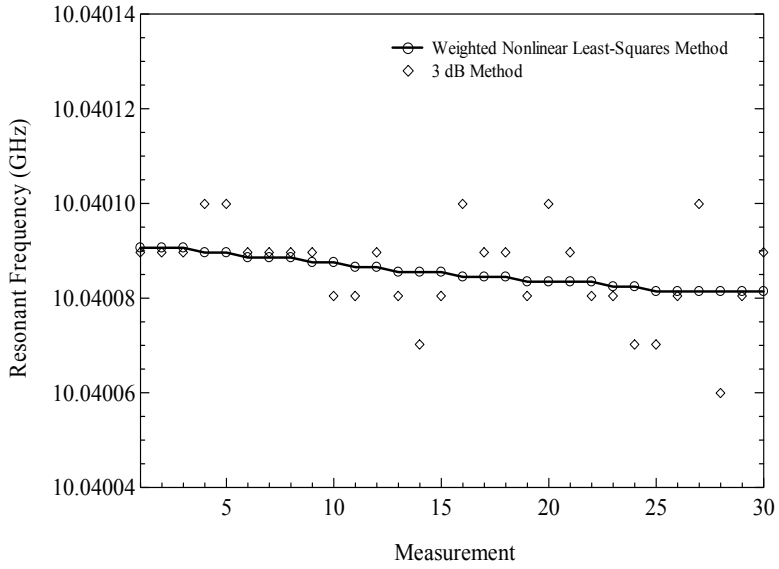

Figure 6.7: Comparison of resonant frequency measurement methods.

However, if both coupling levels are minimized ($\beta_1 \ll 1$ and $\beta_2 \ll 1$), the coupling factors β_1 and β_2 can be neglected and (6.10) rewritten as

$$T(f) = \frac{T(f_0)}{1 + Q^2(\frac{f}{f_0} - \frac{f_0}{f})^2} \approx \frac{T(f_0)}{1 + Q_0^2(\frac{f}{f_0} - \frac{f_0}{f})^2}, \tag{6.12}$$

with the assumption that the measured quality factor Q is approximately Q_0. (If the coupling coefficients are not negligible, see [22] for methods of calculating β_1 and β_2.)

For each measured k^{th} frequency point on the resonance curve

$$T_m(f_k) = |S_{21}(f_k)|^2 = \frac{T(f_0)}{1 + Q^2(\frac{f_k}{f_0} - \frac{f_0}{f_k})^2} \; + \; BG \; + \; \epsilon(f_k), \tag{6.13}$$

where $S_{21}(f_k)$ is the measured scattering parameter, BG is the background noise floor, and $\epsilon(f_k)$ is additive noise with zero expected value and variance $\sigma^2_{\epsilon(f_k)}$. There are four unknowns in the model and these form a four-parameter vector, $\vec{\theta} = (\theta_1, \theta_2, \theta_3, \theta_4) = (T(f_0), Q, f_0, BG)$. For the observed data, we model the variance of the additive noise as

$$\mathrm{VAR}[\epsilon(f_k)] = \sigma^2_{\epsilon(f_k)} = \frac{{\gamma^2}_1}{1 + Q^2(\frac{f_k}{f_0} - \frac{f_0}{f_k})^2} \; + \; {\gamma^2}_2, \tag{6.14}$$

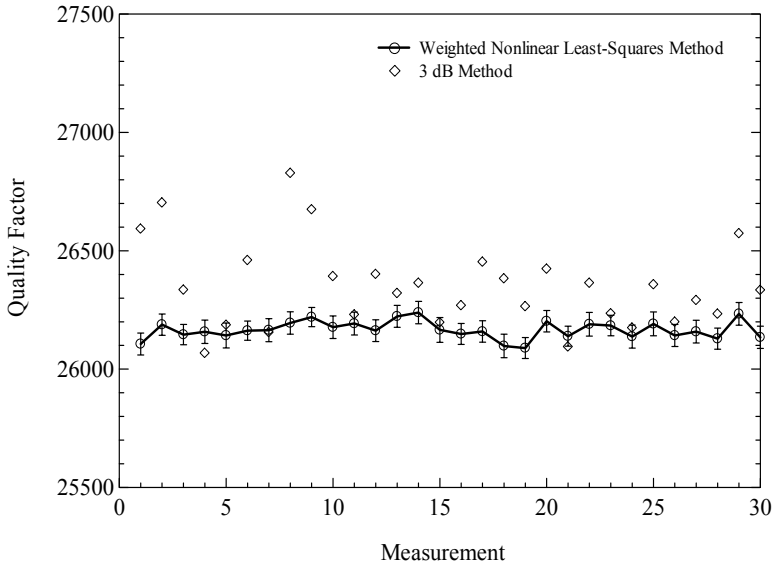

Figure 6.8: Comparison of quality factor measurement methods.

where γ_1 and γ_2 correspond to the frequency-dependent noise and the noise floor, respectively.

A weighted nonlinear least-squares fit of the measured resonance curve to equation (6.14) is performed as outlined in [19] to determine the unknown vector $\vec{\theta}$, which includes the measured resonant frequency and quality factor. Besides estimating the values of the resonant frequency and quality factor, this process also provides the associated uncertainty estimates.

To learn how this new method for calculating the resonant frequency and quality factor reduces the measurement uncertainty, we measured the resonant frequency and quality factor of a split-cylinder resonator with no sample present using both the 3-dB method and the weighted nonlinear least-squares method. In Figure 6.7, we show results for 30 consecutive measurements using both the 3-dB and weighted nonlinear least-squares method and Figure 6.8 shows a similar comparison for the measured quality factor.

Figures 6.7 and 6.8 show a noticeable decrease in the measurement scatter

Measurement Method	Resonant Frequency (GHz)	Standard Deviation (GHz)	Quality Factor	Standard Deviation
Nonlinear Least-Squares	10.004085	0.000003	26170	40
3 dB	10.004082	0.000009	26400	180

Table 6.1: Comparison of measurement method for resonant frequency and loss tangent.

when using the weighted nonlinear least-squares approach. Table 6.1 lists the mean and standard deviation for the resonant frequency and quality factor using both methods. Note that although the two method agree fairly well for both resonant frequency and quality factor, the standard deviations are several times smaller when using the weighted nonlinear least-squares method.

An important assumption in the derivation of equation (6.12) is that the losses due to the coupling loops are negligible. The coupling coefficients are so small that the loaded quality factor Q_L can be considered equal to the unloaded quality factor Q_0. This is only true if the split-cylinder resonator is very undercoupled. In the split-cylinder resonator we used, the penetration distance of the coupling loops into the cylindrical-cavity sections can be adjusted to vary the amount of coupling. Figure 6.9 indicates how the measured quality factor of the TE_{011} resonant mode changes as the coupling level varies.

For very high coupling, where the peak transmission loss is above -40 dB, the measured quality factor decreases due to the increasing resistive losses in the coupling loops. In this case, the coupling coefficients are not negligible and the loaded and unloaded quality factors are not the same. This systematic error in the quality factor is significant because it can lead to errors in the calculation of the sample's loss tangent.

On the other hand, as the coupling level decreases, the measured quality

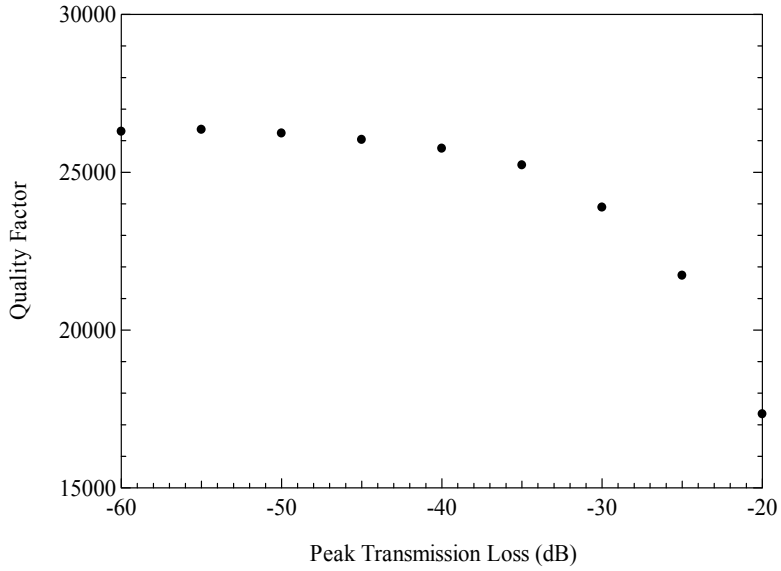

Figure 6.9: Measured quality factor as a function of transmission loss at the peak of the TE_{011} resonant mode.

factor reaches some maximum value. This indicates that the coupling losses are reduced to a level where they do not affect the quality factor measurement. However, at lower coupling levels, the signal-to-noise ratio decreases as well, so one must be careful to pick a level of coupling that minimizes the coupling losses while at the same time keeping the signal-to-noise ratio as high as possible. For the split-cylinder resonator, a coupling level of -50 dB was found to be a good compromise between these two criteria.

6.3.2 Split-Cylinder Dimensions

The radius a and length L of each of the two split-cylinder resonator sections must be characterized to ensure accurate permittivity and loss tangent measurements. First, the length of each of the split-cylinder's cylindrical-cavity sections was measured with a Sylvac digital probe at a temperature of 21.5 C. These measurements were repeated 15 times for each section. The results, including an

Measurement Variable	Value	Standard Uncertainty
Lower Cylindrical-Cavity Section Length – L_l	25.322 mm	0.006 mm (A)
Upper Cylindrical-Cavity Section Length – L_u	25.346 mm	0.004 mm (A)
Mean Length	25.334 mm	u_c(L) = 0.007 mm

Table 6.2: Uncertainty budget for L, the length of a cylindrical-cavity section. The combined standard uncertainty for the length is $u_c(L)$.

Measurement Variable	Value	Standard Uncertainty
Resonant Frequency – f_{011}	10.041 ± 0.0001 GHz	0.0002 mm (B)
Cylindrical-Cavity Section Length – L	25.334 ± 0.007 mm	0.0005 mm (A)
Speed of Light in Vacuum – c	2.99792458 m/s	–
Relative Permittivity of Air in Lab – $\epsilon_a^{'}$	1.00055	–
First Zero of J_1 – j_1	3.83171	–
Differences Between Split-Cylinder Sections		0.005 mm (B)
Split-Cylinder Radius – a	19.050 mm	u_c(a)= 0.005 mm

Table 6.3: Uncertainty budget for a, the radius of cylindrical-cavity section. The combined standard uncertainty for the radius is $u_c(a)$.

uncertainty budget, are shown in Table 6.2. Because the theoretical model for the split-cylinder resonator assumes that the two cylindrical-cavity sections are identical, the mean length for L is used for both sections.

The radius a of the split-cylinder resonator is calculated from a measurement of the TE_{011} resonant mode [23]. First, with no sample, we eliminate the gap ($d = 0$) between the two cylindrical-cavity sections, turning the split-cylinder resonator into a circular-cylindrical cavity with length $2L$ and radius a. With the two coupling loops connected to a network analyzer, we excite the TE_{011} resonance. The resonant frequency of the TE_{011} mode is

$$f_{011} = \frac{c}{2\pi\sqrt{\epsilon_a^{'}}}\sqrt{\left(\frac{j_1}{a}\right)^2 + \left(\frac{\pi}{2L}\right)^2}, \tag{6.15}$$

where $\epsilon_a^{'}$ is the relative permittivity of the air inside the cylindrical cavity and j_1

is the first zero of the Bessel function of the first kind J_1 [24]. Solving (6.15) for the radius a we get

$$a = j_1 \left[\epsilon_a^{'} \left(\frac{2\pi f_{011}}{c} \right)^2 - \left(\frac{\pi}{2L} \right)^2 \right]^{-\frac{1}{2}}. \tag{6.16}$$

Given the mean length L in Table 6.2 and measured resonant frequency, using the method outlined in Section 6.3.1, we used (6.16) to solve for the split-cylinder's radius a and show the results and uncertainty budget in Table 6.3.

6.3.3 Sample Thickness

Besides the dimensions of the split-cylinder resonator, the sample thickness d is another variable that must be characterized to ensure accurate permittivity and loss tangent measurements. With a Mitutoyo digital micrometer, we calculated the mean sample thickness from fifteen distinct points on the sample. Table 6.4 lists these for various locations on a Corning 7980 fused silica sample.

Since the number of repeated measurements is only fifteen, we cannot assume a normal distribution for sample thickness. Rather, we calculate the standard uncertainty $u(d)$ for the repeated measurements using a t-distribution

$$u(d) = t_{\alpha/2,n-1} \frac{s}{\sqrt{n}} \tag{6.17}$$

where $t_{\alpha/2,n-1}$ is the critical value of the t-distribution for a 100(1-α) percent confidence interval, n is the number of thickness measurements, and s is the standard deviation of d [25]. If we select $n = 15$ and $\alpha = 0.05$, then $t_{0.025,14} = 2.145$ and we use (6.17) to calculate a standard uncertainty for the repeated measurements that represents a 95 percent confidence interval. An uncertainty budget for the Corning 7980 fused silica example is shown in Table 6.5.

Sample Location #	Thickness (mm)
1	2.535
2	2.530
3	2.531
4	2.526
5	2.518
6	2.507
7	2.506
8	2.508
9	2.513
10	2.521
11	2.528
12	2.537
13	2.532
14	2.531
15	2.530
Mean Thickness d	2.524

Table 6.4: Sample Thickness Measurements of a Corning 7980 Fused Silica Substrate

Measurement Variable	Standard Uncertainty
Repeated Thickness Measurements	0.023 mm (A)
Digital Micrometer	0.002 mm (B)
Sample Thickness	u_c(d) = 0.023 mm

Table 6.5: Uncertainty budget for d, the sample thickness. The combined standard uncertainty for the sample thickness is $u_c(d)$.

6.3.4 Split-Cylinder Conductivity

The final measurement variable that must be characterized is the conductivity σ of the split-cylinder resonator metal walls, endplates, and flanges. This is an important step since the metal losses must be well-characterized for an accurate calculation of the sample's loss tangent. Similar to the measurement of the split-cylinder radius, we determine the conductivity of the split-cylinder resonator from a measurement of the quality factor TE_{011} resonant mode when the resonator is

Measurement Variable	Value	Standard Uncertainty
Resonant Frequency – f_{011}	10.041 ± 0.0001 GHz	4.62×10^2 S/m
Quality Factor – Q	26400 ± 200	7.03×10^5 S/m
Cylindrical-Cavity Section Length – L	25.334 ± 0.007 mm	1.53×10^3 S/m
Cylindrical-Cavity Section Radius – a	19.050 ± 0.005 mm	1.47×10^3 S/m
Permeability of Free Space – μ_0	$4\pi \times 10^{-7}$ H/m	–
Permittivity of Free Space – ϵ_0	8.854×10^{-12} F/m	–
Relative Permittivity of Air in Lab – $\epsilon_a^{'}$	1.00055	–
First Zero of J_1 – j_1	3.83171	–
Split-Cylinder Conductivity – σ	4.64×10^7 S/m	$u_c(\sigma) = 0.07 \times 10^7$ S/m

Table 6.6: Uncertainty budget for split-cylinder conductivity σ. The combined standard uncertainty for the conductivity is $u_c(\sigma)$.

empty and the gap between the two cylindrical-cavity sections is zero (d=0).

For this configuration, the split-cylinder geometry reduces to that of a circular-cylindrical cavity. The quality factor for a TE_{011} resonant mode is

$$Q = \frac{\sqrt{\frac{\mu_0}{\epsilon_0 \epsilon_a^{'}}} \left[\left(\frac{j_1}{a}\right)^2 + \left(\frac{\pi}{2L}\right)^2 \right]^{\frac{3}{2}}}{2R_s \left[\frac{1}{2L} \left(\frac{\pi}{2L}\right)^2 + \frac{1}{a} \left(\frac{j_1}{a}\right)^2 \right]}. \tag{6.18}$$

where μ_0 and ϵ_0 are the permeability and permittivity in a vacuum, $\epsilon_a^{'}$ is the relative permittivity of the air within the cavity, j_1 is the first zero of the Bessel function of the first kind J_1, a and L are the radius and length of each cylindrical-cavity section of the split-cylinder resonator, and R_s is the surface resistance of the metal conductor [24]. The conductivity of the split-cylinder resonator is assumed to be uniform over the entire fixture.

Solving (6.18) for the surface resistance R_s we get

$$R_s = \frac{\sqrt{\frac{\mu_0}{\epsilon_0 \epsilon_a^{'}}} \left[\left(\frac{j_1}{a}\right)^2 + \left(\frac{\pi}{2L}\right)^2 \right]^{\frac{3}{2}}}{2Q \left[\frac{1}{2L} \left(\frac{\pi}{2L}\right)^2 + \frac{1}{a} \left(\frac{j_1}{a}\right)^2 \right]}. \tag{6.19}$$

The conductivity σ of the metal can be written as a function of the surface resistance R_s [26]

$$\sigma = \frac{2\pi f \mu_0}{2R_s^2} \tag{6.20}$$

where f is the resonant frequency of the TE_{011} mode. Therefore, to determine the value of σ, we first calculate R_s using equation (6.19) and then calculate σ from equation (6.20). An uncertainty budget for the σ is shown in Table 6.6.

Given that the copper surfaces of the split-cylinder resonator suffer somewhat from surface roughness and impurities, our measured conductivity (4.64×10^7 S/m) is not far from the conductivity of pure copper (5.81×10^7 S/m).

6.4 Relative Permittivity and Loss Tangent Measurements

After characterizing all the necessary intermediate measurement variables, discussed in the previous section, we now focus on the calculation of the relative permittivity and loss tangent of the sample. In this section, we outline the step-by-step measurement procedure, including a discussion of the uncertainty analysis.

6.4.1 Sample Thickness

Prior to any measurements, contaminants on the surfaces of the sample should be removed as they can be a source of error, especially for the measurement of loss tangent. These contaminants include particles and lubricants that result from machining as well as oils from handling. To remove the contaminants, we clean each sample with 99% pure isopropyl alcohol and a lint-free cloth, making sure that the alcohol has completely evaporated after cleaning. In addition, we use lint-free gloves and avoid contact with the top and bottom faces of the sample.

After cleaning, we calibrate a digital micrometer and then measure the thickness of the sample over several locations. Using the procedure in Section 6.3.3,

we calculate the thickness d and standard uncertainty $u(d)$.

6.4.2 Split-Cylinder Dimensions and Conductivity

Next, as with the sample, we clean any contaminants on the surfaces of the split-cylinder resonator using 99% pure isopropyl alcohol and a lint-free cloth. After cleaning, we measure the length L of the split-cylinder's two cylindrical-cavity sections using a digital probe and calculate the measurement uncertainty $u(L)$ as outlined in Section 6.3.2.

We then reassemble the split-cylinder resonator and connect the coupling loops to the ports of an automatic network analyzer. To minimize the effect of drift in our measurements, we require that the network analyzer be on for over one hour before we make any measurements. After the allowing the system to warm up, we close the gap between the two cylindrical-cavity sections and resonate the TE_{011} mode. After adjusting the coupling loops so that the peak transmission loss is less than -50 dB, we measure the resonant frequency f and quality factor Q of the TE_{011} mode using the weighted nonlinear least-squares method described in Section 6.3.1. From the measurement of the resonant frequency, we calculate the radius a of the cylindrical-cavity sections using (6.16). With the measured quality factor, we compute the conductivity σ of the resonator metal using (6.20).

6.4.3 Resonant Frequency and Quality Factor

A dielectric substrate is then placed between the two cylindrical-cavity sections, and the split-cylinder resonator is adjusted so that the two conductive flanges contact both sides of the substrate. Depending on the relative permittivity and thickness of the substrate, there may be a significant decrease in the resonant frequency compared with the resonant frequency of the empty split-cylinder resonator, as described in Section 6.2.2. Once the resonant mode has been identified,

one calculates the resonant frequency f and quality factor Q using the method of weighted least-squares described in Section 6.3.1.

6.4.4 Relative Permittivity

At this point, all the intermediate variables have been measured, and one can calculate the relative permittivity of the dielectric substrate. In Chapter 5, we selected the theoretical model based on the mode-matching method to model the split-cylinder resonator, and this is the model we implemented in our measurement software. As described in Section 2.3, given an initial guess, we iteratively solve for the relative permittivity $\epsilon_s^{'}$ using the resonance condition

$$\det\left[\mathbf{Z}\right] = 0. \tag{6.21}$$

In Table 6.7, we show the data from a measurement of a Corning 7980 fused silica substrate. First, we note the values and uncertainties of the intermediate variables. These include the resonant frequency f of the TE_{011} mode, the radius a and length L of a single cylindrical-cavity section, and the sample thickness d. For the Corning 7980 fused silica substrate, the computed relative permittivity $\epsilon_s^{'}$ is 3.833.

Also included in Table 6.7 is a calculation of the combined standard uncertainty $u_c(\epsilon_s^{'})$ for the relative permittivity. If we assume that the relative permittivity is a function g of several intermediate variables

$$\epsilon_s^{'} = g(f_0, a, L, d) \tag{6.22}$$

then $u_c(\epsilon_s^{'})$ can be obtained from

$$u_c^2(\epsilon_s^{'}) = \left(\frac{\partial g}{\partial f_0}\right)^2 u^2(f_0) + \left(\frac{\partial g}{\partial a}\right)^2 u^2(a) + \left(\frac{\partial g}{\partial L}\right)^2 u^2(L) + \left(\frac{\partial g}{\partial d}\right)^2 u^2(d) \tag{6.23}$$

where $u(f_0)$, $u(a)$, $u(L)$ and $u(d)$ are the uncertainty of the resonant frequency, cylindrical-cavity radius, cylindrical-cavity length, and sample thickness respec-

Measurement Variable	Nominal Value	Standard Uncertainty
Resonant Frequency – f	9.504 ± 0.0001 GHz	0.0005
Split-Cylinder Length – L	25.334 ± 0.007 mm	0.0006
Split-Cylinder Radius – a	19.050 ± 0.005 mm	0.0109
Sample Thickness – d	0.809 ± 0.004 mm	0.0141
Relative Permittivity – $\epsilon_s^{'}$	3.833	$u_c(\epsilon_s^{'})$= 0.018

Table 6.7: Relative permittivity measurement and uncertainty budget for a Corning 7980 fused-silica substrate.

tively. We used the mode-matching model to numerically compute the partial derivative in (6.23). Labeled as the standard uncertainty in Table 6.7, we list the contribution of each of the various uncertainty sources and note that the sample thickness d and the cylindrical-cavity radius a are the largest sources of error for this particular measurement. Combining the standard uncertainties according to (6.23), we found the combined standard uncertainty $u_c(\epsilon_s^{'})$ to be 0.018, almost 0.5 percent uncertainty for the relative permittivity. If we assume a coverage factor $k = 2$, then $U(\epsilon_s^{'})$, the computed expanded uncertainty is 0.036, slightly more than 0.9 percent uncertainty [27].

6.4.5 Sample Loss Tangent

With the substrate's relative permittivity calculated, one can determine the loss tangent. From Section 2.4, we explicitly calculate the loss tangent $\tan\delta$ using

$$\tan\delta = \frac{\dfrac{\omega(W_s + W_a)}{Q} - P_e - P_w - P_f}{\epsilon_0\epsilon_s^{'}\dfrac{\pi b^2\omega}{4}\displaystyle\sum_{n=1}^{NS}|B_n|^2|V_n|^2 J_0^2(h_{ns}b)\left[d + \dfrac{\sin(p_{ns}d)}{p_{ns}}\right]}. \tag{6.24}$$

In Table 6.8, we show the data from a measurement of a Corning 7980 fused-silica substrate. First, we note the values and uncertainties of the intermediate variables. These include the resonant frequency f and quality factor Q of the

TE_{011} mode, the radius a, length L and conductivity σ of a cylindrical-cavity section, and the sample thickness d. For this particular case, the computed loss tangent $\tan\delta$ was 1.39×10^{-4}.

Also included in Table 6.8 is a calculation of the combined standard uncertainty $u_c(\tan\delta)$ for the loss tangent. If we assume that the loss tangent is a function g of several intermediate variables

$$\tan\delta = g(f_0, Q, a, L, \sigma, d) \tag{6.25}$$

then $u_c(\tan\delta)$ can be obtained from

$$\begin{aligned} u_c^2(\tan\delta) &= \left(\frac{\partial g}{\partial f_0}\right)^2 u^2(f_0) + \left(\frac{\partial g}{\partial Q}\right)^2 u^2(Q) + \left(\frac{\partial g}{\partial a}\right)^2 u^2(a) \\ &+ \left(\frac{\partial g}{\partial L}\right)^2 u^2(L) + \left(\frac{\partial g}{\partial \sigma}\right)^2 u^2(\sigma) + \left(\frac{\partial g}{\partial d}\right)^2 u^2(d) + u^2(b) \end{aligned} \tag{6.26}$$

where $u(f_0)$, $u(Q)$, $u(a)$, $u(L)$ $u(\sigma)$ and $u(d)$ are the uncertainty of the resonant frequency, quality factor, cylindrical-cavity radius, cylindrical-cavity length, cylindrical-cavity conductivity, and sample thickness respectively. We used the mode-matching model to numerically compute the partial derivatives in (6.26). Note that we've added the $u^2(b)$ to the list of uncertainties terms in (6.26). This is not the uncertainty in the radius of the sample, but the systematic error we discuss in Section 2.4 to account for the variability in the loss tangent due to the perfectly-conducting boundary we assumed at $\rho = b$.

After combining the various uncertainty components using (6.26), we found that the combined uncertainty for the loss tangent of the 7980 Corning fused silica sample was 2×10^{-5}. If we assume a coverage factor $k = 2$, then the expanded uncertainty is 4×10^{-5}. As seen in Table 6.8, the largest uncertainty source for the loss tangent is the systematic error attributed to the boundary at $\rho = b$, followed by the uncertainty in the quality factor and conductivity.

Measurement Variable	Nominal Value	Standard Uncertainty
Resonant Frequency – f	9.504 ± 0.0001 GHz	2.11×10^{-8}
Quality Factor – Q	17086 ± 200	2.07×10^{-6}
Split-Cylinder Length – L	25.334 ± 0.007 mm	4.00×10^{-8}
Split-Cylinder Radius – a	19.050 ± 0.005 mm	5.26×10^{-7}
Split-Cylinder Conductivity – σ	4.64 ± 0.07 S/m	1.62×10^{-6}
Sample Thickness – d	0.809 ± 0.004 mm	1.11×10^{-7}
Conductive Boundary at $\rho = b$		2×10^{-5}
Loss Tangent – $\tan\delta$	1.39×10^{-4}	$u_c(\tan\delta) = 2 \times 10^{-5}$

Table 6.8: Example uncertainty budget for the loss tangent of a Corning 7980 fused-silica substrate.

6.5 Measurement Intercomparison

In our measurement intercomparison, we applied the split-cylinder resonator method to determine the relative permittivity and loss tangent of four dielectric substrates: Corning 7980 fused silica, single-crystal quartz, Corning 1723 glass, and Coors Vistal alumina. These four dielectric substrates cover a wide range in relative permittivity (3-10) and loss tangent ($1 \times 10^{-5} - 5 \times 10^{-3}$). For these measurements, we performed single-frequency measurement using the TE_{011} resonant mode. Table 6.9 shows relative permittivity results while Table 6.10 shows loss tangent results.

In order to verify the accuracy of the split-cylinder measurements, we measured the same four materials in a circular-cylindrical cavity [24], shown in Figure 6.10. As the electrical properties of these substrates are frequency dependent, we tried to measure the substrates as close as possible to the frequency of the split-cylinder resonator measurements. For comparison, the circular-cylindrical cavity results are shown in Tables 6.9 and 6.10. There is good agreement between the two measurement methods for both the relative permittivity and loss tangent of all four materials.

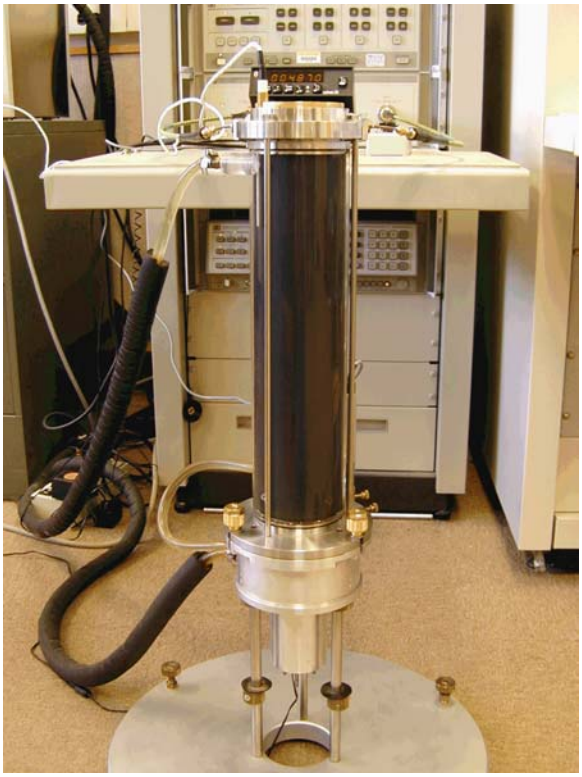

Figure 6.10: Circular-cylindrical cavity.

Sample	**Split-Cylinder Resonator**		**Cylindrical Cavity**	
	f (GHz)	$\epsilon_r^{'}$	f (GHz)	$\epsilon_r^{'}$
7980 Fused Silica	9.503	3.829 ± 0.018	9.432	3.837±0.019
Single-Crystal Quartz	9.338	4.437 ± 0.015	9.290	4.429±0.022
1723 Glass	8.763	6.147 ± 0.017	8.631	6.156±0.031
Vistal Alumina	8.135	10.016 ± 0.023	8.135	9.994±0.050

Table 6.9: Comparison of relative permittivity measurements using a split-cylinder resonator and a circular-cylindrical cavity.

Sample	**Split-Cylinder Resonator**		**Cylindrical Cavity**	
	f (GHz)	$\tan\delta \times 10^{-3}$	f (GHz)	$\tan\delta \times 10^{-3}$
7980 Fused Silica	9.503	0.14 ± 0.02	9.432	0.12 ± 0.05
Single-Crystal Quartz	9.338	0.02 ± 0.03	9.290	0.01 ± 0.05
1723 Glass	8.763	4.64 ± 0.13	8.631	4.62 ± 0.07
Vistal Alumina	8.135	0.01 ± 0.02	8.135	0.05 ± 0.05

Table 6.10: Comparison of loss tangent measurements using a split-cylinder resonator and a circular-cylindrical cavity.

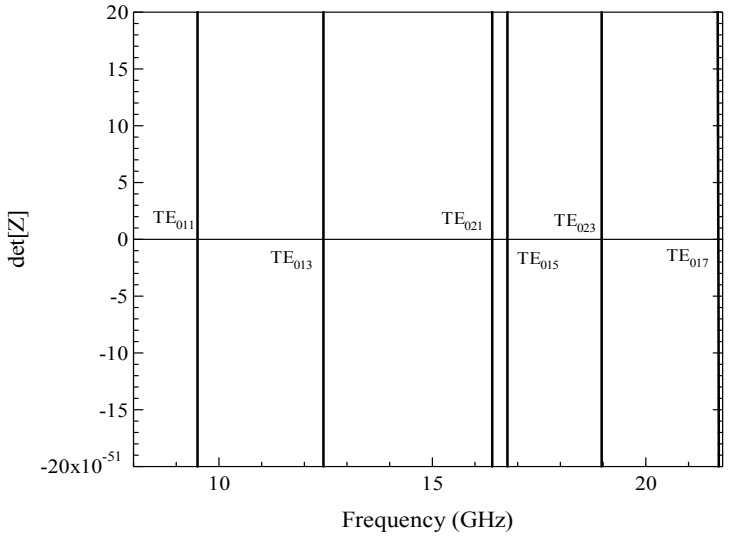

Figure 6.11: Zero-crossings of det[**Z**] showing the frequencies of the first six TE_{0np} resonant modes.

6.6 Broadband Measurements using TE_{0np} Resonant Modes

Up to this point we have only used the TE_{011} resonant mode to make single-frequency relative permittivity and loss tangent measurements using the split-cylinder resonator. However, the mode-matching model derived for the split-cylinder resonator includes not only the TE_{011} mode but also the higher-order TE_{0np} modes. Therefore, we employ these higher-order modes so that the relative permittivity and loss tangent can be measured over a wider frequency range.

We used two split-cylinder resonators to measure the complex permittivity of two fused-silica substrates over a frequency range of 10 to 50 GHz. The first of these resonators, whose TE_{011} resonant frequency is 10 GHz with no sample, has dimensions $2a$=38.1 mm and L=25.3 mm. The resonator was constructed from oxygen-free copper and had a small hole in the waveguide wall for the coupling loop. The second split-cylinder resonator, whose TE_{011} resonant frequency is 35 GHz with no sample, has dimensions $2a$=13.18 mm and L=3.51 mm. The resonator was constructed from silver-plated brass and also had small holes in

each section to accommodate the coupling loops.

Two fused-silica samples, machined from the same lot, were measured with the two split-cylinder resonators. The sample for the larger split-cylinder resonator was 55 mm square and 0.81 mm thick. The sample for the smaller resonator was 25 mm square and 0.28 mm thick. Each sample was placed between the two cylindrical-cavity sections of the split-cylinder resonator, and the resonance curve for the TE_{011} mode was examined on an automatic network analyzer. From the resonance curve, we obtained the resonance frequency f and the quality factor Q. From these two quantities and the geometrical dimensions of the split-cylinder resonator and sample, the sample relative permittivity using (2.67) and the sample loss tangent were calculated using (2.92).

We noted earlier that equation (2.67) could be used to calculate the resonant frequency of the split-cylinder resonator, given the substrate's relative permittivity and thickness and the dimensions of the split-cylinder resonator. With the value of the relative permittivity calculated from the TE_{011} resonance, a plot of $\det[\mathbf{Z}]$ as a function of frequency is shown in Figure 6.11. The first zero crossing corresponds with the TE_{011} mode while the other zero crossings correspond to the higher-order TE_{0np} modes. For increased measurement sensitivity, only the TE_{0np} modes where p is an odd integer are included, as these modes have a maximum electric field at the center of the sample. It is important to note where these frequencies occur before attempting to measure them with a network analyzer because as the frequency increases, modes other than those in the TE_{0np} family are excited. The information contained in Figure 6.11 reduces the chance of measuring an incorrect mode.

After correctly identifying these higher-order modes, we measured the resonant frequency and quality factor of each with a network analyzer. In some cases, the TE_{0np} resonance may be close in frequency to other resonant modes, thereby

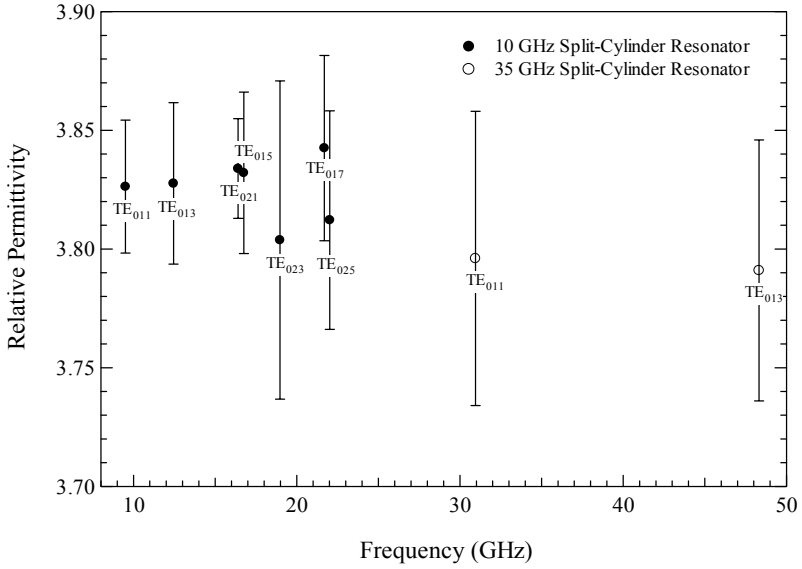

Figure 6.12: Relative permittivity of 7980 Corning fused silica substrate using higher-order TE_{0np} modes.

distorting the resonance curve. One must use these modes with caution as this distortion may cause errors in the calculation of the resonant frequency and quality factor. Once the resonant frequency and quality factor are determined, we again calculate the relative permittivity and loss tangent of the substrate using (2.67) and (2.92). Figure 6.12 shows the measured relative permittivity of fused silica using two split-cylinder resonators. As expected, the permittivity is relatively flat over the frequency range. Figure 6.13 shows the measured loss tangent of fused silica measured with the two split-cylinder resonators. We note an increase in the loss tangent as a function of frequency, and over the frequency range of 10 to 50 GHz, the increase is linear with frequency.

Finally, to verify the accuracy of the broadband, fused silica measurements, we machined additional samples for testing in a circular-cylindrical cavity, a dielectric-post resonator, and several split-post resonators. In Figures 6.14 and 6.15 the split-cylinder resonator measurements of relative permittivity and loss tangent are compared to measurements made with these other methods. We

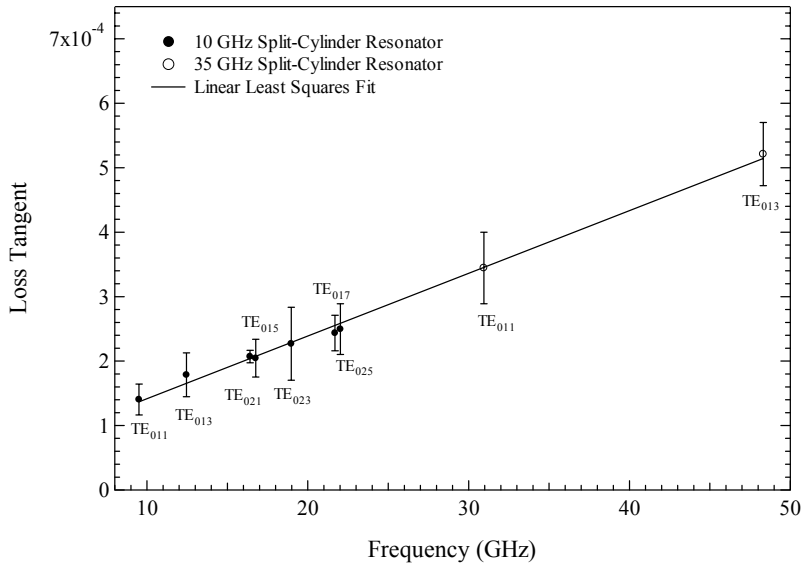

Figure 6.13: Loss tangent of 7980 Corning fused silica substrate using higher-order TE_{0np} modes.

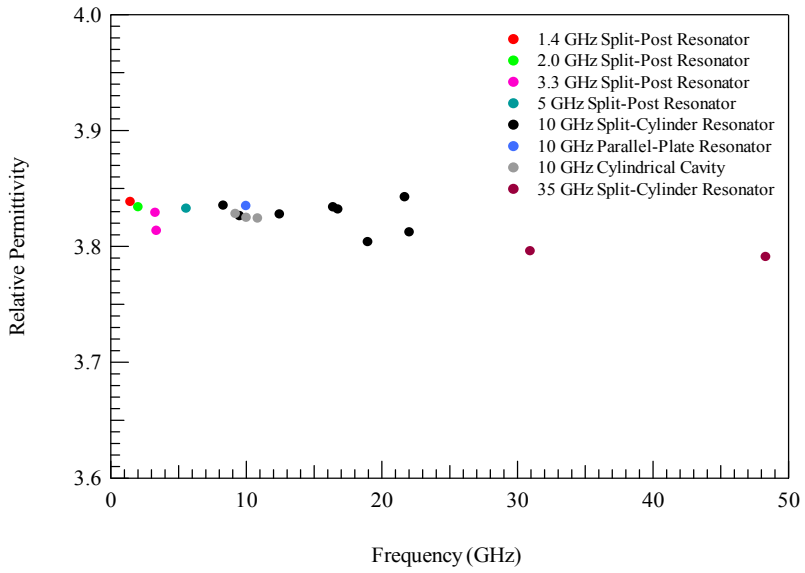

Figure 6.14: Comparison of measurement methods for broadband relative permittivity measurements of 7980 Corning fused silica substrate.

found close agreement between all the methods for both relative permittivity and loss tangent over the frequency range from 1 to 50 GHz.

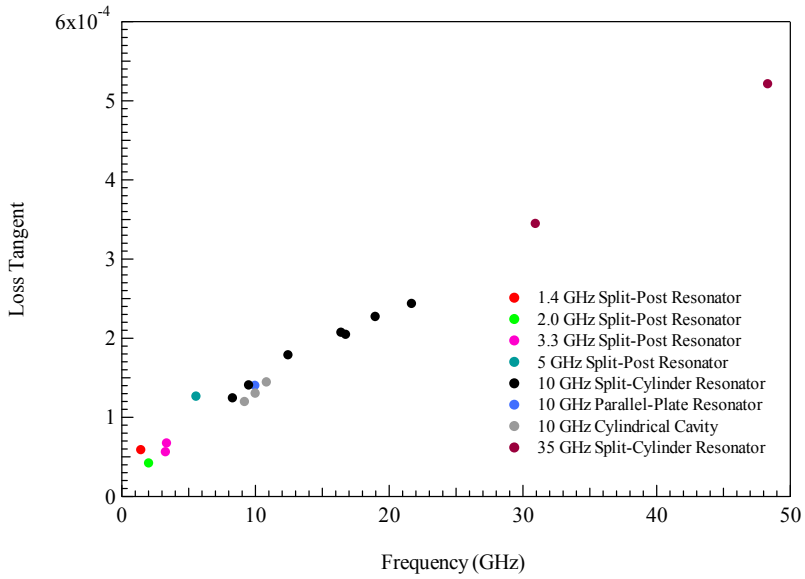

Figure 6.15: Comparison of measurement methods for broadband loss tangent measurements of 7980 Corning fused silica substrate.

6.7 Thin-Material Measurements

The ability to characterize thin ($<$ 1.0 mm) dielectric materials is an important consideration when selecting a measurement method as thin materials are becoming more widespread. Unfortunately, many measurement methods do not have the sensitivity to make accurate measurements of either permittivity or loss tangent because the sample is often placed in a relatively low electric field. For example, in a cylindrical cavity resonator, the sample is placed directly on the bottom conductive endplate. The electric field is very low in this region and the resonant frequency and quality factor of the cavity are only slightly perturbed. However, in the split-cylinder resonator method, the sample is placed in a maximum electric field so that the measurement sensitivity is increased.

In order to demonstrate the ability of the split-cylinder resonator to measure the permittivity and loss tangent of thin materials, we performed a series of measurements on six polyimide films, each with a nominal thickness of 0.05 mm.

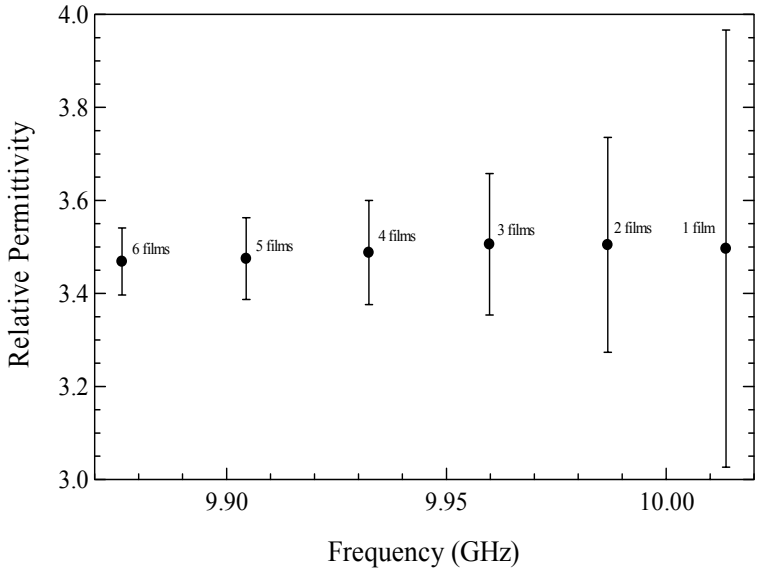

Figure 6.16: Relative permittivity of polyimide films as a function of frequency.

First, we measured a single polyimide film using the split-cylinder resonator, and we show the relative permittivity results in Figure 6.16 and the loss tangent results in Figure 6.17. The uncertainty in both the relative permittivity and loss tangent are high for the single-film measurement, because relative sample thickness uncertainty is relatively high.

To verify the single-film measurement, additional films were stacked on the original film individually in sequence, and the relative permittivity and loss tangent were measured after the addition of each film. Figures 6.16 and 6.17 show the measurement results for the stacked films. As expected, the resonant frequency and the measurement uncertainty for both relative permittivity and loss tangent decreased as additional films were added. For all six measurements, the results agreed within the measurement uncertainty.

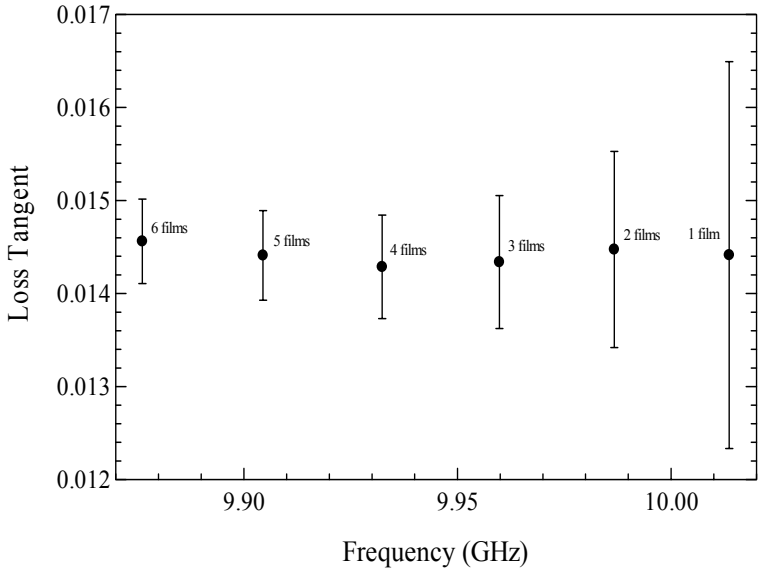

Figure 6.17: Loss tangent of polyimide films as a function of frequency.

6.8 Repeatability Study

In order to evaluate the long-term stability of the split-cylinder resonator measurements, we designed a repeatability study for measurements of the relative permittivity and loss tangent of several dielectric substrates. Since not all of the sources of variability can be identified in our uncertainty analysis, the repeatability study helps to validate our uncertainty analysis and verify the stability of the measurement system.

We chose four dielectric substrates that would cover a wide range in relative permittivity (3-10) and loss tangent ($1 \times 10^{-5} - 5 \times 10^{-3}$). The four substrates selected were 7980 Corning fused silica, single-crystal quartz, 1723 Corning Glass, and Coors Vistal alumina. The study consisted of a series of measurement sessions, each on a separate day, where the four substrates were measured with the split-cylinder resonator described in Section 6.2.1. The measurement order for the four substrates during any single measurement session was random, and the repeatability study consisted of eight measurement sessions made over a period of

Sample	$\epsilon_s^{'}$	Standard Deviation
7980 Corning Glass	3.826	0.003
Single-Crystal Quartz	4.435	0.005
1723 Corning Glass	6.151	0.005
Coors Vistal Alumina	10.025	0.013

Table 6.11: Repeatability study results for the relative permittivity $\epsilon_s^{'}$ of four dielectric substrates.

Sample	$\tan\delta \times 10^{-3}$	Standard Deviation
7980 Corning Glass	0.139	0.001
Single-Crystal Quartz	0.024	0.001
1723 Corning Glass	4.656	0.008
Coors Vistal Alumina	0.011	0.001

Table 6.12: Repeatability study results for the loss tangent $\tan\delta$ of four dielectric substrates.

two months. Measured values of relative permittivity and loss tangent for the four dielectric substrates are shown in Figures 6.18-6.21. Results of the study in Tables 6.11 and 6.12 show the average measured relative permittivity and loss tangent of the four substrates as well as the measured standard deviations. For all four materials, there is little variation in the results over time and the standard deviations are relatively small and well within the measurement uncertainties. Thus, the major uncertainty sources in our uncertainty analysis have been accounted for.

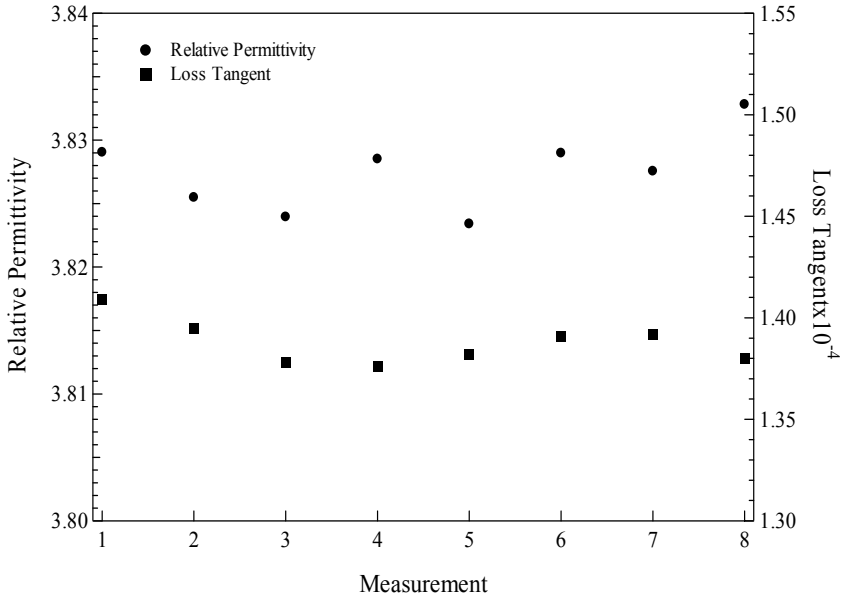

Figure 6.18: Repeatability study for 7980 Corning fused silica. The measured resonant frequency is approximately 9.504 GHz.

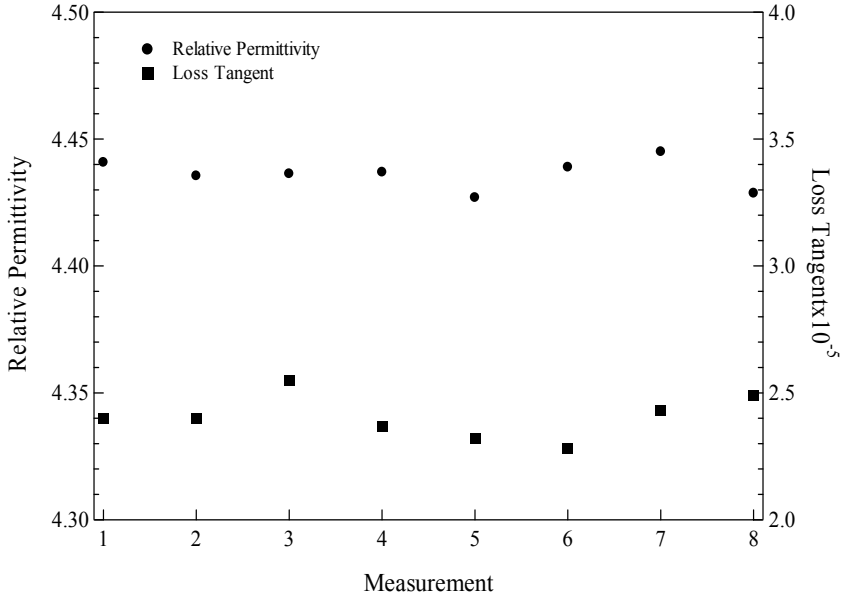

Figure 6.19: Repeatability study for single-crystal quartz. The measured resonant frequency is approximately 9.338 GHz.

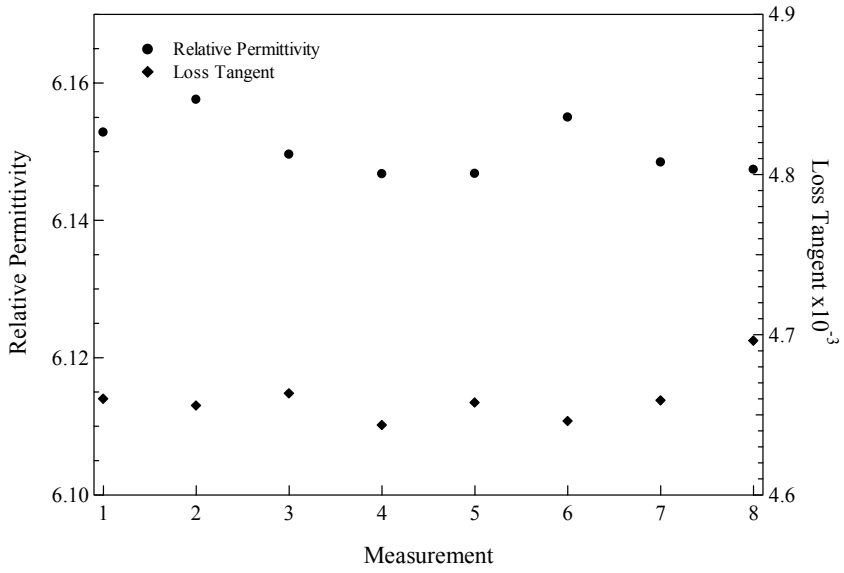

Figure 6.20: Repeatability study for 1723 Corning glass. The measured resonant frequency is approximately 8.763 GHz.

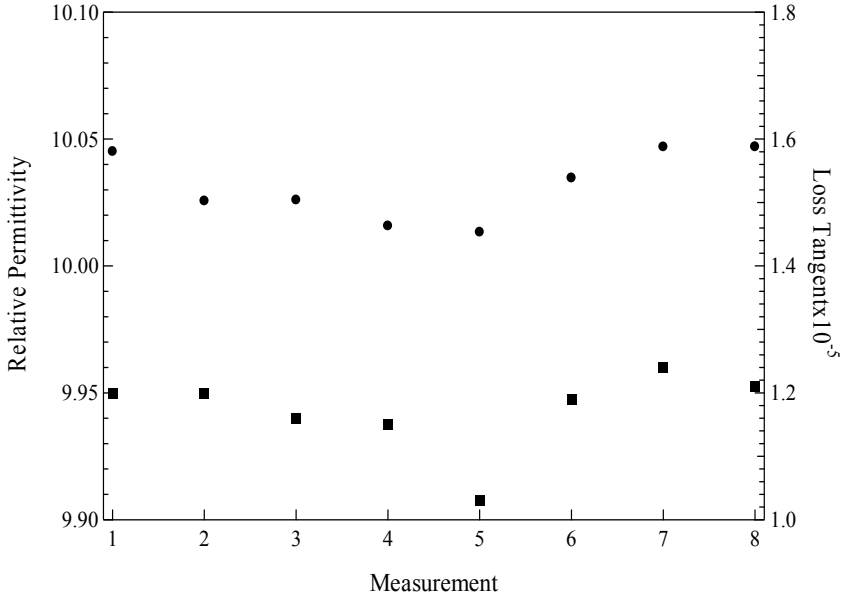

Figure 6.21: Repeatability study for Coors Vistal alumina. The measured resonant frequency is approximately 8.135 GHz.

Chapter 7

Conclusion and Future Work

In this thesis we developed three theoretical models for the split-cylinder resonator. These models, derived using the mode-matching, least-squares boundary residual, and Hankel-transform method, allow one to make nondestructive relative permittivity and loss tangent measurements of dielectric substrates from a measurement of the resonant frequency and quality factor of a TE_{0np} mode.

Unlike previous models that used only the TE_{011} mode to perform single-frequency measurements, our models include higher-order TE_{0np} modes that broaden the frequency range of the split-cylinder resonator. To improve the accuracy of the relative permittivity measurement, we accurately represented the fringing fields in the sample region, rather than by perturbation methods used in previous models. Also, the separation of the conductive losses of the split-cylinder resonator from the dielectric losses of the substrate significantly improved the sensitivity of the loss tangent measurement.

In a detailed comparison of the models, the mode-matching model was found to be superior to the LSBR and Hankel-transform methods on the basis of accuracy in the calculation of relative permittivity and loss tangent as well as computational speed. As a result, we incorporated the mode-matching model into our measurement software and used it to characterize several dielectric substrates that varied in both relative permittivity ($\epsilon_s^{'} = 3 - 10$) and loss tangent

($\tan\delta = 1 \times 10^{-5} - 5 \times 10^{-3}$). Comparison of these measurements with a split-cylinder resonator and a circular-cylindrical cavity at a single frequency, indicated close agreement in both the relative permittivity and loss tangent. With the higher-order TE_{0np} resonant modes, measurements over a broader frequency range showed close agreement with those made in a circular-cylindrical cavity, dielectric-post resonator, and several split-post resonators over a frequency range of 1-50 GHz.

Because of symmetry, the electric field in the split-cylinder resonator is maximum at the center of the sample, resulting in a higher sensitivity for both relative permittivity and loss tangent measurements. As a result, the relative permittivity and loss tangent were obtained for polyimide films that were only 0.05 mm thick.

In addition to these measurement results, an uncertainty analysis was developed for both the relative permittivity and loss tangent. This revealed uncertainties within 0.5 percent for the relative permittivity. The major sources of uncertainty were the split-cylinder radius a and the sample thickness d. For the loss tangent, uncertainties of not less than 2×10^{-5} were found. Although there were contributions due to uncertainties in the quality factor Q and conductivity of the split-cylinder metal σ, the main source of uncertainty was a systematic error introduced by assumption of the conductive boundary at $\rho = b$ in order to implement the mode-matching method. Through a repeatability study we found that our uncertainty analysis had taken into account the major random error sources and that the measurement system was stable over time.

We discovered, however, several issues related to the split-cylinder that might make the method unattractive to some users. First, although the conductive losses of split-cylinder walls, endplates and flanges were separated from the dielectric losses in the substrate, the level of the conductive losses reduces the

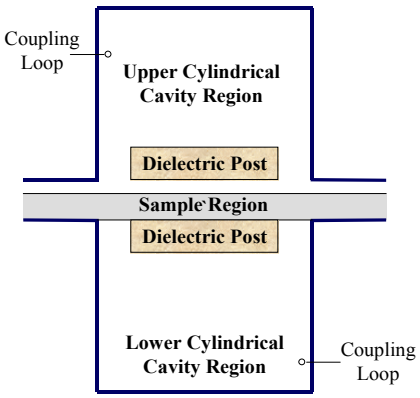

Figure 7.1: Split-post resonator.

sensitivity of the loss tangent measurement. In any attempt to measure substrates with loss tangent less than 1×10^{-4}, significant uncertainty is introduced.

Second, we found that the resonant frequency of the split-cylinder resonator was highly dependent on the sample's thickness and relative permittivity. In the case of our split-cylinder resonator, we observed that the resonant frequency could vary from 2 to 10 GHz depending on the properties of the dielectric substrate. In some cases this might not be desirable, as one might want to measure the properties of a wide range of substrates at approximately the same frequency.

To mitigate these concerns, we plan to investigate the *split-post resonator*, another measurement technique for nondestructive relative permittivity and loss tangent measurements [28]. The geometry of the split-post resonator, shown in Figure 7.1, is similar to the split-cylinder resonator except for two items. First, there are two dielectric posts in each of the cylindrical-cavity sections. Second, the gap between the two halves of the split-post resonator is fixed so that the dielectric substrate does not contact the upper half of the split-post resonator.

For certain aspect ratios of the dielectric posts, most of the electric and magnetic fields are confined to the posts and the region between the post where the sample resides. As a result, only a small amount of the fields interacts with the conductive metal walls, endplates, and flanges, most of the power is dissipated in the posts and sample. If the dielectric posts are fabricated from low-loss materials, then most of the energy will be dissipated in the sample, increasing the sensitivity of the loss tangent measurement.

The dielectric posts serve a dual purpose in that the relative permittivity, thickness and diameter of the posts largely control the resonant frequency of the split-post resonator. The difference in resonant frequency with and without sample is relatively small compared to that observed in the split-cylinder resonator. Therefore, a split-post resonator can measure a wide range of dielectric substrates at approximately the sample frequency.

The advantages of the split-cylinder resonator come at a cost however. In the case of the split-cylinder resonator, the fields in each of the three regions can be represented by simple waveguide modes, and because of it's symmetry, only two of the three regions needed consideration. The split-post resonator has six distinct regions that must be included in the model, and the two regions with the dielectric posts must be modeled as sections of loaded waveguide.

As a result, in applying the mode-matching method to derive a theoretical model for the split-cylinder resonator, the expressions to calculate the relative permittivity and loss tangent are much more complex. In addition, computational speed may also become an issue. However, we will pursue the modeling of the split-post resonator, as we believe the advantages far outweigh the drawbacks.

Bibliography

[1] J. Baker-Jarvis, R. Geyer, J. Grosvenor, M. Janezic, C. Jones, B. Riddle, C. Weil, and J. Krupka, "Dielectric characterization of low-loss materials in the range 1 GHz to 20 GHz: A comparison of techniques," *IEEE Trans. Dielect. Elect. Insulation*, vol. 5, no. 4, pp. 571–577, 1998.

[2] G. Kent, "An evanescent-mode tester for ceramic dielectric substrates," *IEEE Trans. Microwave Theory Tech.*, vol. 36, no. 10, pp. 1451–1454, October 1988.

[3] G. Kent, "Nondestructive permittivity measurement of substrates," *IEEE Trans. Instrum. Meas.*, vol. 45, no. 1, pp. 102–106, February 1996.

[4] G. Kent and S. Bell, "The gap correction for the resonant-mode dielectrometer," *IEEE Trans. Instrum. Meas.*, vol. 45, no. 1, pp. 98–101, February 1996.

[5] W.C. Hahn, "A new method for the calculation of cavity resonators," *J. Appl. Phys.*, vol. 12, pp. 62–68, January 1941.

[6] J.R. Whinnery and H.W. Jamieson, "Equivalent circuits for discontinuities in transmission lines," *Proc. IRE*, vol. 32, pp. 98–116, February 1944.

[7] A. Wexler, "Solution of waveguide discontinuities by modal analysis," *IEEE Trans. Instrum. Meas.*, vol. 15, no. 9, pp. 508–517, September 1967.

[8] P.J.B. Clarricoats and K.R. Slinn, "Numerical solution of waveguide-discontinuity problems," *Proc. IEE*, vol. 114, pp. 878–886, July 1967.

[9] R.E. Collin, *Field Theory of Guided Waves*, McGraw-Hill Book Company, Inc., 1960.

[10] G.V. Eleftheriades, A.S. Omar, and L.P.B. Katehi, "Some important properties of waveguide junction generalized scattering matrices in the context of the mode matching method," *IEEE Trans. Microwave Theory Tech.*, vol. 42, pp. 1896–1903, October 1994.

[11] C. Vassallo, *Théorie des Guides D'Ondes Électromagnétiques*, Eyrolles, 1985.

[12] P.H. Masterman and P.J.B. Clarricoats, "Computer field-matching solution of waveguide transverse discontinuities," *Proc. IEE*, vol. 118, no. 1, pp. 51–63, January 1971.

[13] A.S. Ilinskii and E.Y. Fomenko, "Investigation of infinite-dimensional systems of linear algebraic equations of the second kind in waveguide diffraction problems," *Comput. Maths. Math. Phys.*, vol. 31, no. 3, pp. 1–11, 1991.

[14] J.B. Davies, "A least-squares boundary residual method for the numerical solution of scattering problems," *IEEE Trans. Microwave Theory Tech.*, vol. 21, no. 2, pp. 99–104, February 1973.

[15] H.J.A. LaRiviere and J.B. Davies, "The solution of electromagnetic eigenvalue problems by least square boundary residuals," *IEEE Trans. Microwave Theory Tech.*, pp. 436–441, May 1975.

[16] R. Jansen, "On the performance of the least squares method for waveguide junctions and discontinuities," *IEEE Trans. Microwave Theory Tech.*, pp. 434–436, May 1975.

[17] M.D. Janezic and J. Baker-Jarvis, "Full-wave analysis of a split-cylinder resonator for nondestructive permittivity measurements," *IEEE Trans. Microwave Theory Tech.*, vol. 47, no. 10, pp. 2014–2020, October 1999.

[18] P. Petersan and S. Anlage, "Measurement of resonant frequency and quality factor of microwave resonators: Comparison of methods," *Journal of Applied Physics*, vol. 84, no. 6, pp. 3392–3402, September 1998.

[19] K.J. Coakley, J.D. Splett, M.D. Janezic, and R.F. Kaiser, "Estimation of q-factors and resonant frequency," *IEEE Trans. Microwave Theory Tech.*, vol. 51, no. 3, pp. 862–868, March 2003.

[20] C.G. Montgomery, R.H. Dicke, and E.M. Purcell, *Principles of Microwave Circuits*, McGraw-Hill Book Company, 1948.

[21] E.L.Ginzton, *Microwave Measurements*, McGraw-Hill Book Company, 1957.

[22] D. Kajfez, *Q Factor*, Vector Fields, 1994.

[23] J.C. Gallop and W. Radcliffe, "Shape and dimensional measurement using microwaves," *J. Phys. E: Sci. Instrum.*, vol. 19, pp. 413–417, 1986.

[24] E. Vanzura, R. Geyer, and M. Janezic, *The NIST 60-Millimeter Diameter Cylindrical Cavity Resonator: Performance for Permittivity Measurements*, Natl. Inst. Stand. Technol. Tech. Note 1354, 1993.

[25] J.L. Devore, *Probability and Statistics for Engineering and the Sciences*, Brooks/Cole Publishing Company, 1991.

[26] D. Pozar, *Microwave Engineering*, Addison-Wesley Publishing Company, 1990.

[27] B.N. Taylor and C.E. Kuyatt, *Guidelines for Evaluating and Expressing the Uncertainty of NIST Measurement Results*, Natl. Inst. Stand. Technol. Tech. Note 1297, 1994.

[28] J. Krupka and S. Maj, "Local complex permittivity measurement of MIC substrates," *CPEM*, pp. 154–155, 1986.

Appendix A

Split-Cylinder Resonator Mechanical Drawings

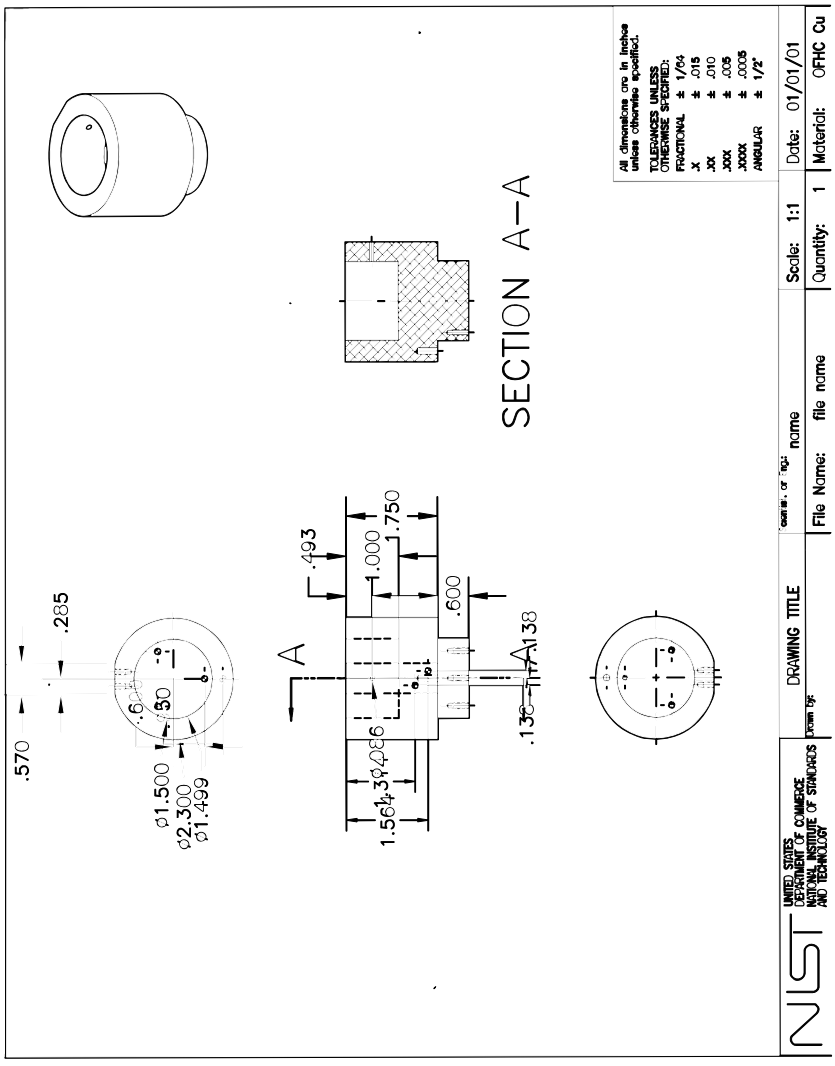

Figure A.1:

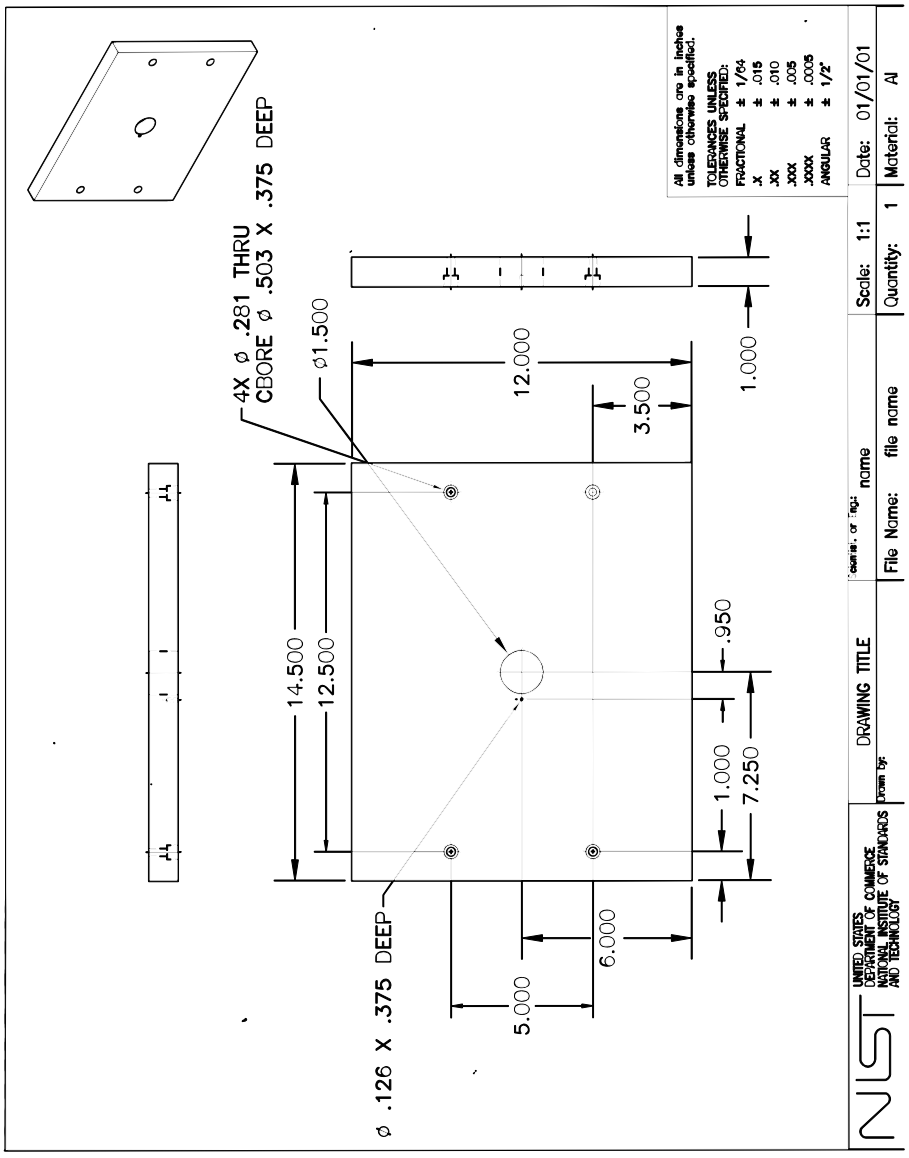
4X ø .281 THRU
CBORE ø .503 X .375 DEEP
ø1.500
ø .126 X .375 DEEP
14.500
12.500
12.000
3.500
1.000
.950
1.000
7.250
6.000
5.000
All dimensions are in inches
unless otherwise specified.
TOLERANCES UNLESS
OTHERWISE SPECIFIED:
FRACTIONAL ± 1/64
.X ± .015
.XX ± .010
.XXX ± .005
.XXXX ± .0005
ANGULAR ± 1/2°
Scale: 1:1
Date: 01/01/01
Quantity: 1
Material: Al
File Name: file name
Material or Tag: name
DRAWING TITLE
Drawn by:
UNITED STATES
DEPARTMENT OF COMMERCE
NATIONAL INSTITUTE OF STANDARDS
AND TECHNOLOGY

Figure A.2:

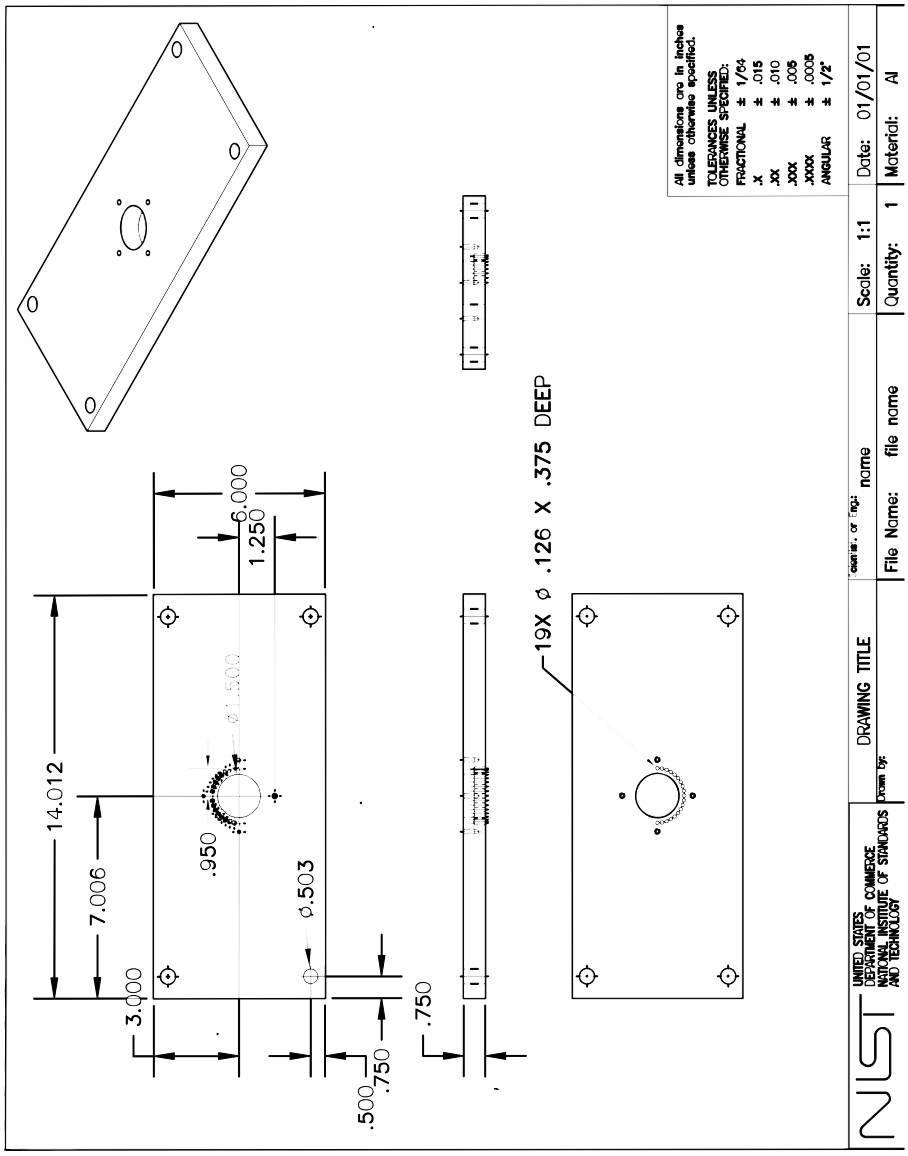
All dimensions are in inches
unless otherwise specified.
TOLERANCES UNLESS
OTHERWISE SPECIFIED:
FRACTIONAL ± 1/64
.X ± .015
.XX ± .010
.XXX ± .005
.XXXX ± .0005
ANGULAR ± 1/2°
UNITED STATES
DEPARTMENT OF COMMERCE
NATIONAL INSTITUTE OF STANDARDS
AND TECHNOLOGY
DRAWING TITLE
Drawn by:
Scale: 1:1
Date: 01/01/01
File Name: file name
Quantity: 1
Material: Al
14.012
7.006
3.000
6.000
1.250
.950
Ø1.500
Ø.503
.500
.750
.750
19X Ø .126 X .375 DEEP

Figure A.3:

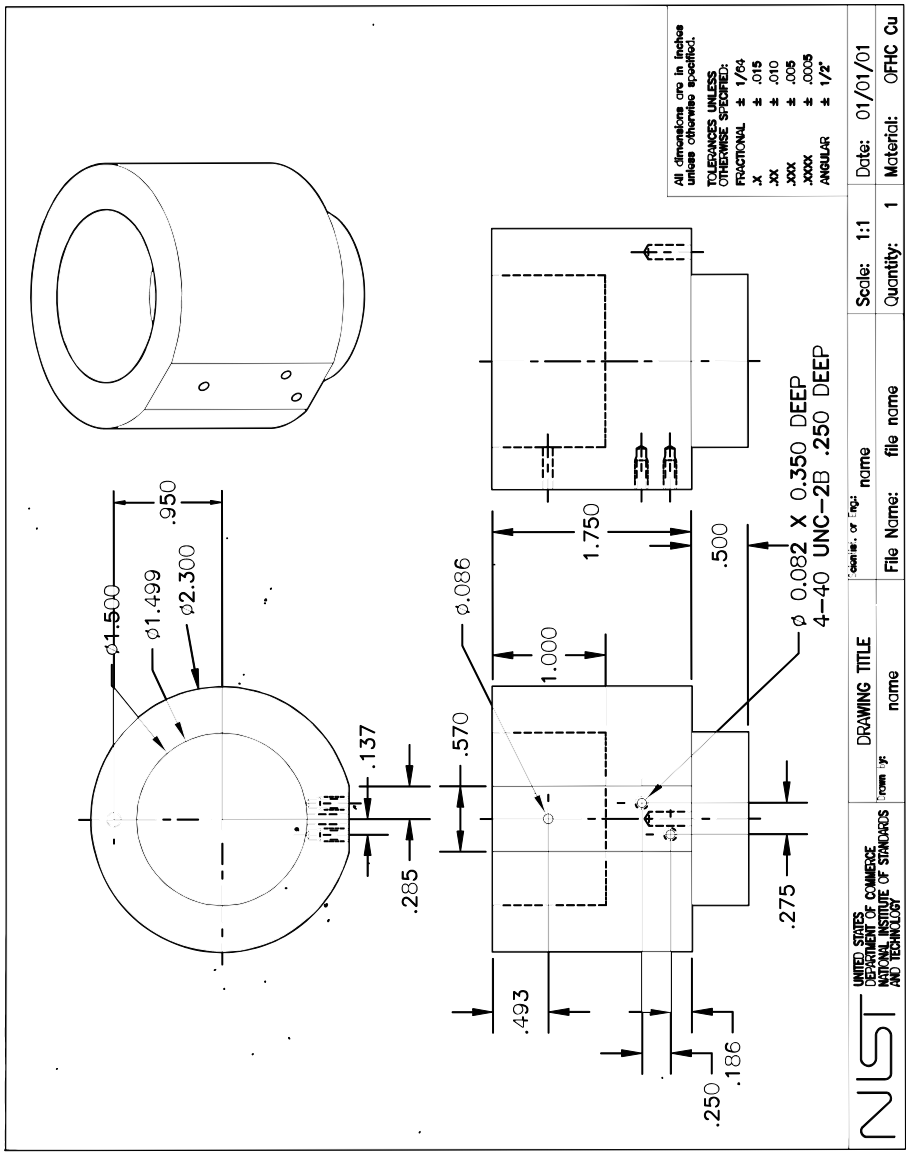
All dimensions are in inches unless otherwise specified.
TOLERANCES UNLESS OTHERWISE SPECIFIED:
FRACTIONAL ± 1/64
.X ± .015
.XX ± .010
.XXX ± .005
.XXXX ± .0005
ANGULAR ± 1/2°
UNITED STATES DEPARTMENT OF COMMERCE NATIONAL INSTITUTE OF STANDARDS AND TECHNOLOGY
NIST
DRAWING TITLE
Drawn by: name
Examined or Engd: name
File Name: file name
Scale: 1:1
Quantity: 1
Date: 01/01/01
Material: OFHC Cu
ø1.500
ø1.499
ø2.300
.950
.137
.285
.570
ø.086
1.000
1.750
.500
ø 0.082 X 0.350 DEEP
4-40 UNC-2B .250 DEEP
.493
.186
.250
.275

Figure A.4:

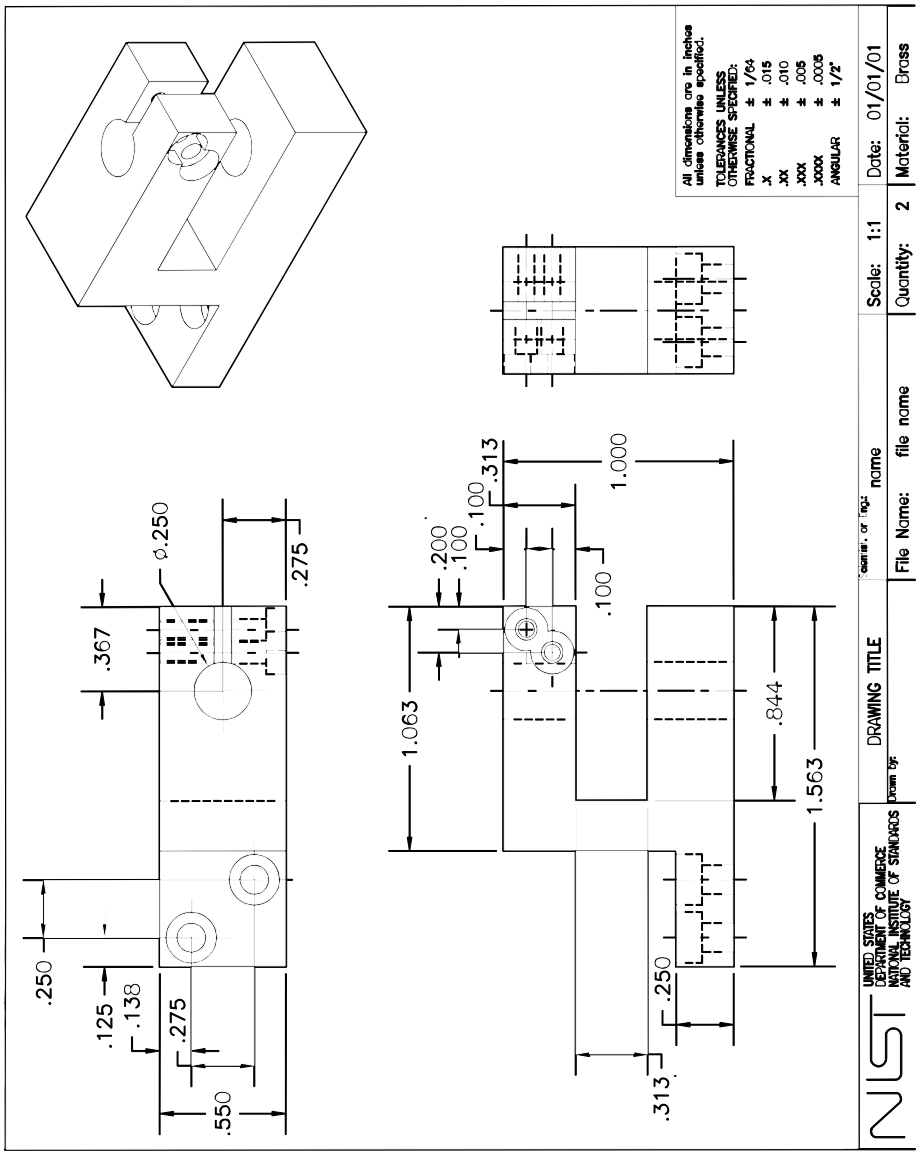
All dimensions are in inches unless otherwise specified.
TOLERANCES UNLESS OTHERWISE SPECIFIED:
FRACTIONAL ± 1/64
.X ± .015
.XX ± .010
.XXX ± .005
.XXXX ± .0005
ANGULAR ± 1/2°
DRAWING TITLE
UNITED STATES DEPARTMENT OF COMMERCE NATIONAL INSTITUTE OF STANDARDS AND TECHNOLOGY
Scale: 1:1
Date: 01/01/01
Quantity: 2
Material: Brass
File Name: file name
.250
.125
.138
.275
.550
.367
ø.250
.275
.200
.100
.313
1.000
.100
1.063
.844
1.563
.313
.250

Figure A.5:

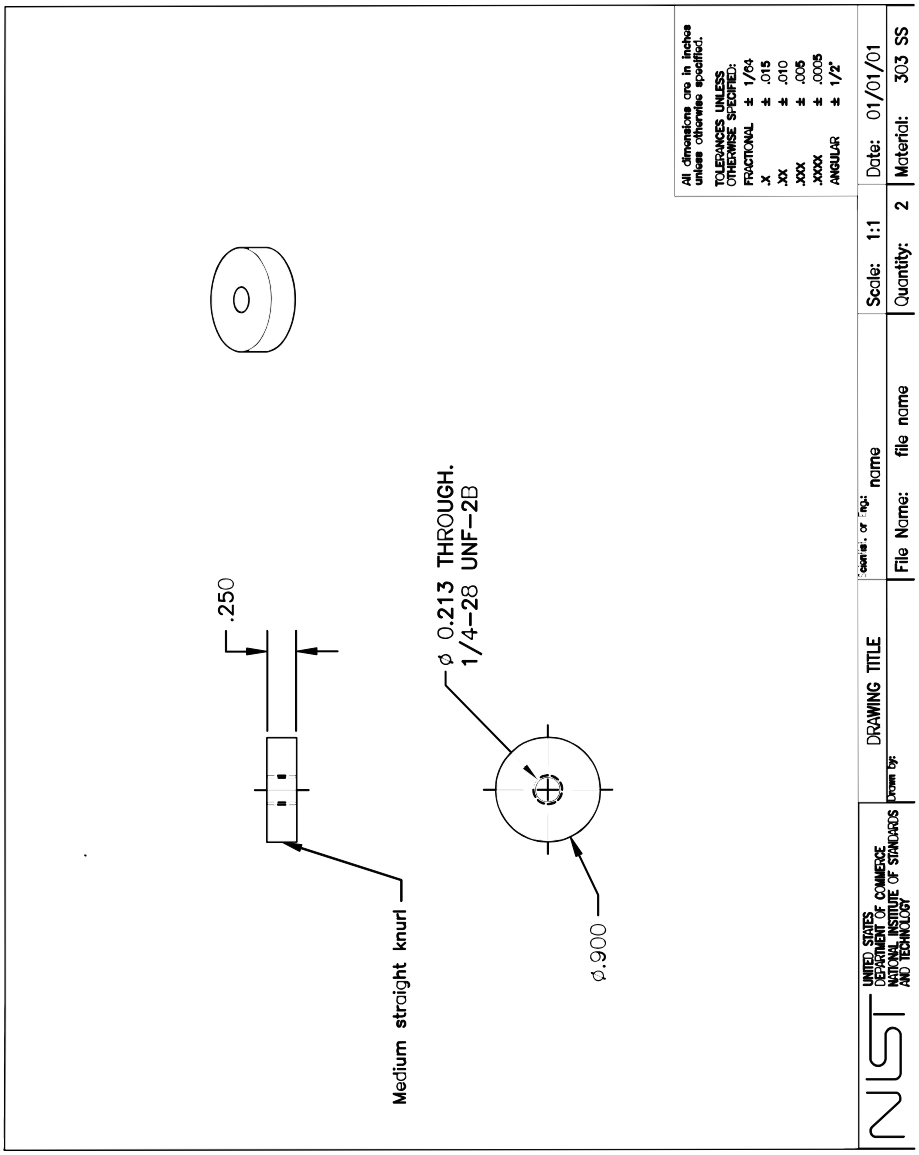
.250
Medium straight knurl
ø 0.213 THROUGH.
1/4–28 UNF–2B
ø.900
All dimensions are in inches unless otherwise specified.
TOLERANCES UNLESS OTHERWISE SPECIFIED:
FRACTIONAL ± 1/64
.X ± .015
.XX ± .010
.XXX ± .005
.XXXX ± .0005
ANGULAR ± 1/2°
UNITED STATES DEPARTMENT OF COMMERCE NATIONAL INSTITUTE OF STANDARDS AND TECHNOLOGY
DRAWING TITLE
Drawn by:
name
File Name: file name
Scale: 1:1
Quantity: 2
Date: 01/01/01
Material: 303 SS

Figure A.6:

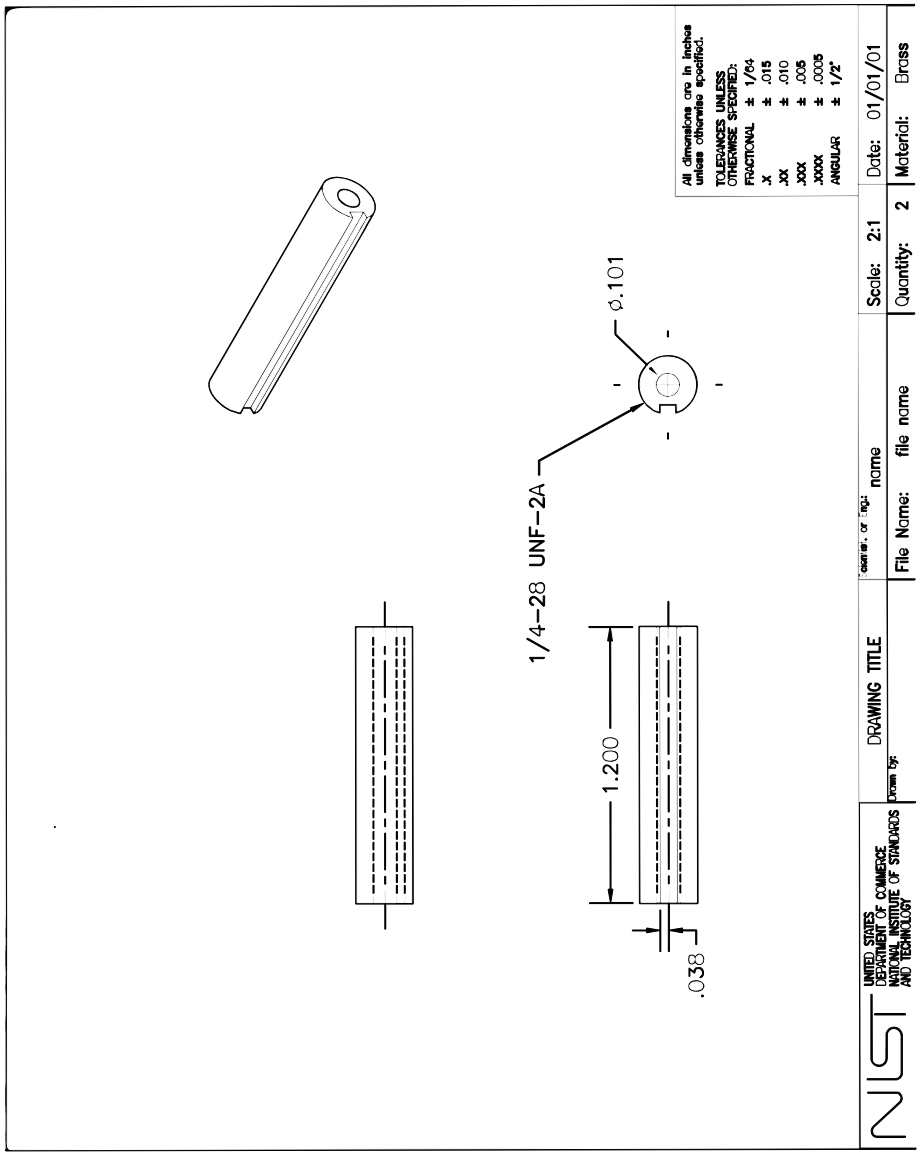
All dimensions are in inches unless otherwise specified.
TOLERANCES UNLESS OTHERWISE SPECIFIED:
FRACTIONAL ± 1/64
.X ± .015
.XX ± .010
.XXX ± .005
.XXXX ± .0005
ANGULAR ± 1/2°
Ø.101
1/4-28 UNF-2A
1.200
.038
UNITED STATES DEPARTMENT OF COMMERCE NATIONAL INSTITUTE OF STANDARDS AND TECHNOLOGY
DRAWING TITLE
Drawn by:
name
Scale: 2:1
Date: 01/01/01
File Name: file name
Quantity: 2
Material: Brass

Figure A.7:

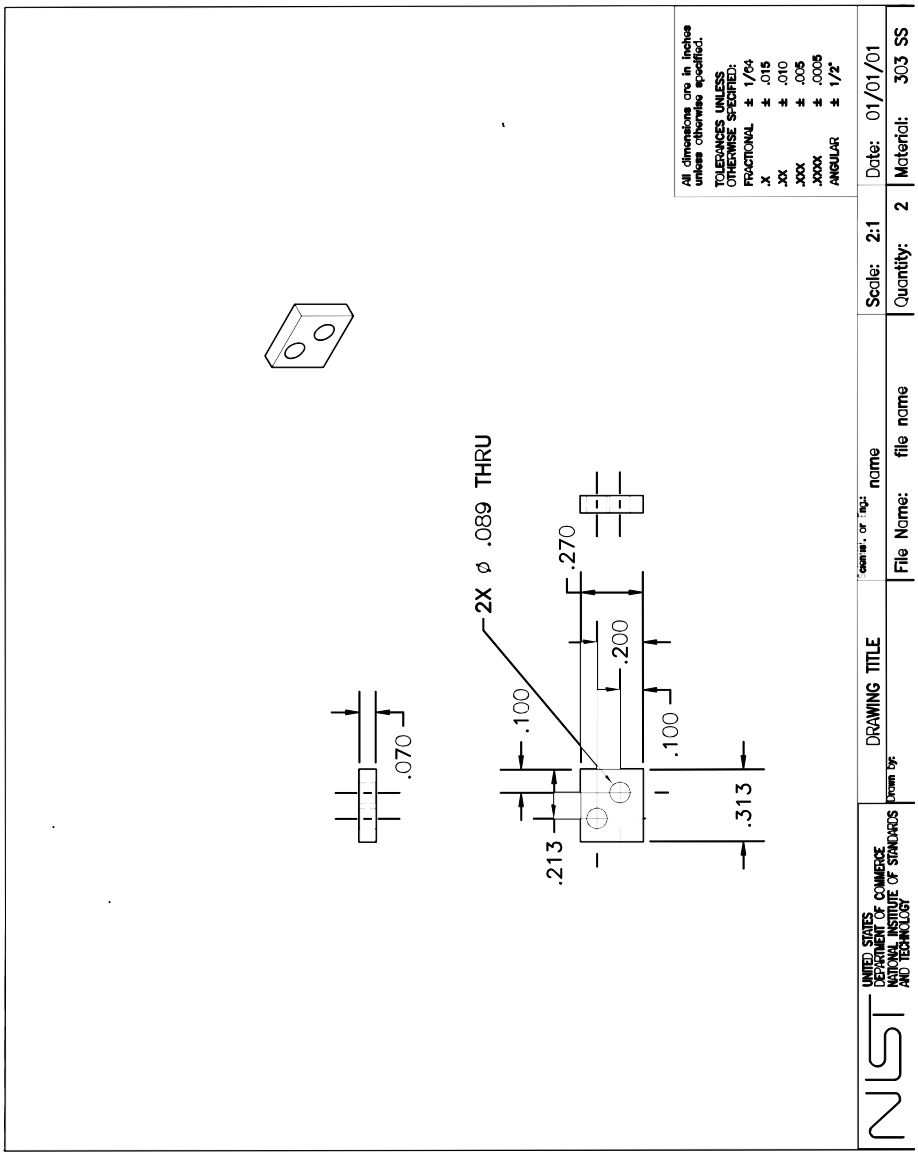
All dimensions are in inches unless otherwise specified.
TOLERANCES UNLESS OTHERWISE SPECIFIED:
FRACTIONAL ± 1/64
.X ± .015
.XX ± .010
.XXX ± .005
.XXXX ± .0005
ANGULAR ± 1/2°
UNITED STATES DEPARTMENT OF COMMERCE NATIONAL INSTITUTE OF STANDARDS AND TECHNOLOGY
DRAWING TITLE
Drawn by:
Geometric Tol.: name
File Name: file name
Scale: 2:1
Quantity: 2
Date: 01/01/01
Material: 303 SS
2X ø .089 THRU
.070
.100
.213
.270
.200
.100
.313

Figure A.8: